Positioning and control of single-photon emitters in SiC-based nanostructures for quantum applications

Benedicte Allum Pedersen

Thesis submitted for the degree of Master of Science in Material Science and Nanotechnology

60 credits

Department of Chemistry

Faculty of mathematics and natural sciences

University of Oslo

Spring 2022

Positioning and control of single-photon emitters in SiC-based nanostructures for quantum applications
http://www.duo.uio.no/
Trykk: Reprosentralen, Universitetet i Oslo

Abstract

Point defects in silicon carbide (SiC) are a promising platform for single-photon sources and qubits for use in quantum technology, such as quantum computing, communication, and sensing. The silicon vacancy (V_{Si}) in the 4H-SiC polytype is a quantum compatible point defect that is rapidly gaining attention in research. The use of waveguides and photonic structures is a possible way to control the intensity and directionality of point defect emission. In this thesis, the V_{Si} has been identified with cathodoluminescence in a SiC sample with nanostructures of different sizes. The sample showed emission in the V1 and V1' zero-phonon lines associated with the negatively charged silicon vacancy (V_{Si}^-). The nanostructures showed stronger emission intensities from V_{Si}^- compared to the sample, it was also shown that the emission intensities from V_{Si}^- increased as the size of the structures decreased. Angle-resolved cathodoluminescence was used for measurements of the directionality of the emission from V_{Si}^-. The radiation profiles of the structures showed changes from the Lambertian radiation profile obtained from the substrate. These measurements also showed the highest enhancement of the V_{Si}^- intensity and the highest change in directionality compared to the substrate was found in the smallest structure.

The Finite-Difference Time-Domain (FDTD) method was used for further understanding of the optical characterization. The simulation method was developed by simulation of an ensemble of defects in SiC nanostructures. After verification of the method with results from the optical characterizations, the simulation method was employed for the understanding of the experimental measurements. An asymmetric nanopillar was simulated and showed emission directions corresponding to what was observed in the experimental structures. Finally, FDTD was used for simulations of structures in a size domain and shaped not yet possible in the lab. The simulations showed increased intensities for a pillar half the size of the simulated wavelength. Simulations of other geometrical structures such as a rectangular waveguide, a pyramid, and a hemisphere were conducted to demonstrate further use of the simulation method.

Sammendrag

Punktdefekter i silisiumkarbid (SiC) er en lovende plattform for såkalte "single-photon" kilder og qubits for bruk i kvanteteknologi, som for eksempel kvantedatamaskiner, kvantekommunikasjon og kvant basert sensorteknologi. Silisium vakansen (V_{Si}) i 4H-SiC polytypen er en kvantekompatibel punktdefekt som raskt har fått økt oppmerksomhet innen forskning. For å kontrollere intensiteten og retningen til emisjonen fra punktdefekter ser man til bølgeledere og fotoniske strukturer som en mulig løsning. I denne oppgaven, har katodeluminescens blitt brukt for å identifisere V_{Si} i en SiC prøve med sylindriske nanostrukturer av ulik størrelse. Målinger med katodeluminescens viste skarpe emisjon i de såkalte "zero-phonon" linjene V1 og V1' assosiert med den negativt ladede silisium vakansen (V_{Si}^-). Emisjons intensiteten fra V_{Si}^- i nanostrukturene og de ustrukturerte områdene ble sammenlignet og det ble observert forsterket intesnitet fra nanostrukturene relativ til den flate overflate. Økningen i intensitet fra V_{Si}^- viste seg også å øke når størrelsen på nanostrukturene minket. Vinkel-oppløst katodeluminescens ble brukt for målinger av emisjons retningene til V_{Si}^-. Polare emisjons profiler fra målinger av nanostrukturene viste avvik fra den Lambertiske emisjon profilen til den flate overflaten. Disse målingene viste også den høyeste forsterkningen av emisjons intensiteten fra V_{Si}^-. Den største endringen i emisjons retningen ble funnet i de minste strukturene, sammenlignet med den flate overflaten.

Den numeriske simuleringsmetoden "Finite-Difference Time-Domain" (FDTD) ble anvendt for videre forståelse av den optiske karakteriseringen. Simulerings metoden ble utviklet med hensyn på modellering av et defekt ensemble i SiC nanostrukturer. Metoden har blitt verifisert ved sammenligning av numeriske og eksperimentelle resultater, og ble deretter brukt for dypere forståelse av de observasjonene gjort med katodeluminescens og vinkel-oppløst katodeluminescens. Simuleringer av en asymmetrisk nanostruktur viste emisjons retninger samsvarende med eksperimentelle resultater. Til slutt, ble den utviklede FDTD modellen brukt for å simulere strukturer med nanoskala dimensjoner som enda ikke er praktisk tilgjengelige på MiNaLaben. Andre geometriske strukturer, som en rektangulær bølgeleder, en pyramide og en hemisfære, ble simulert for å demonstrere videre bruk av den utviklede simuleringsmetoden.

Acknowledgements

First, I want to thank my main supervisor Prof. Lasse Vines for excellent guidance and for pointing me in the right direction. I want to thank my other supervisors Snorre Braathen Kjeldby and Vilde Mari Reinertsen, to Snorre for having endless patience at the CL lab, and to Vilde for answering all my questions about FDTD. I also want to thank Marianne Etzelmüller Bathen for participating in discussions regarding my thesis and for good guidance on CL. And thanks to all of you for proofreading my thesis. Thanks to Gard Selnesaunet for fabricating the nanostructures used in this thesis.

I would like to thank my mom for always supporting me and boosting my confidence by being my biggest fan. Thanks to Eirik and Johanne for all the fun we always have together and for being the best teammates when life took us to unexpected paths. I also want to thank the rest of my extended family for always showing a genuine interest in how my studies were going.

Thanks to all my classmates during the last five years at UiO, I am very grateful for all friendships I have gained. Thanks to my best friends Anna and Mariel for all the study breaks and late nights both in and outside of the university, I will certainly miss seeing you every day.

Contents

Chapter 1

Introduction

Computers and electronic devices are a natural part of our everyday life. The basic building block of a computer and many other electronic devices is the transistor. The very first transistor was made of germanium and developed by a team at Bell Telephone Laboratories in 1948 [1]. After this development, transistors received great attention in research. In the mid-1950s, the first silicon transistor was in production. This marked the start of the transistor as a fundamental building block for integrated circuits (ICs) and thereby modern computer technology [1]. The development of the transistor technology in ICs followed a rapid development, known as *Moore's law*, described by Gordon Moore in 1965 [2]. He stated that the number of components placed on a silicon chip had approximately doubled every year. As continued transistor size reduction is no longer achievable this growth has started to stagnate. The stagnation has resulted in an investigation into new technologies. One of the approaches to overcome the limitations of present computer technology is quantum computing. Quantum computers offer to speed up some well-known operations, in addition, they provide capabilities much beyond what is currently available. A quantum computer, for example, is well suited to tackling exceedingly complicated problems with several variables. It is not expected that quantum computers will be replacing current computer technology any time soon. However, for problems such as prediction of the weather or the finance market, and complex quantum chemistry problems, a quantum computer will potentially be well-suited [3].

At the beginning of the 1900s physicists had the perception of energy being a continuous wave-like phenomenon, and that energy was independent of the characteristics of physical matter. In 1900 the German physicist, Max Planck, published his study of radiation from a black body and presented the theory about energy being made up of particle-like components, restricted to discrete sets of energy, known as *quantization*. This marked the birth of quantum theory, and Plank later was rewarded the Nobel Prize in physics for his work [4]. In 1905 Einstein applied Planck's quantum theory to light and explained the phenomenon, known as the *photoelectric effect* [5]. The *first quantum revolution* relates to these theoretical ideas established during the 20th century. The presence of a band gap and the utilization of this in components is a prime example with respect to the present topic for this first revolution. We are currently in the midst

of the *second quantum revolution*, in which quantum theory created in the 1900s is applied to develop new technologies [6]. The use of these ideas to produce practical applications and devices is referred to as *quantum technology* (QT) and includes for example quantum computation, quantum communication, and quantum sensing.

1.1 Quantum Technology

The development of QT is based on five fundamental principles. The first principle is Heisenberg's *uncertainty principle*, which states that for every certain measurement of a quantum state, there is at least one other state in the system that is measured uncertain. This means, for instance, that we cannot precisely determine the position and momentum of a particle simultaneously. Instead, we have to compute the *probability* of the particle being in a specific state. The *superposition* principle describes that if the outcome of an event consists of two or more indistinguishable situations, the system is in a state of both outcomes simultaneously until a measurement is performed and the system is forced into one of the outcomes. When two quantum systems are coupled together, their states cannot be described independently of each other. If the first system experiences a measurement, the state of the second system will change as a result. This phenomenon is called *entanglement*. The *coherence* of a quantum state is the ability to maintain superposition over time. The loss of information about the second system's initial state or the collapse of the quantum state into a classical state is called *decoherence*. The time before decoherence or the time before quantum features of the system are leaked to the environment is termed the *coherence time*.

Quantum computing, quantum communication, and quantum sensing are important technologies based on these quantum principles. All three of these technologies utilize the quantum bits or *qubits*, which are the basic building blocks of QT. The most well-known of the quantum technologies is probably quantum computers; as previously mentioned, the development of conventional computers has started to stagnate, and quantum computers could participate in further technological advances in the computer field. While a regular, *classical* computer consists of bits that could hold either 0 (OFF) or 1 (ON), a qubit can be in either the state of 0 or 1, like a classical computer, but also be in a superposition of 0 and 1 at the same time [3]. The idea of entanglement is used to connect networks of qubits. By combining superposition and entanglement, a quantum computer has the theoretical capability to outperform classical computers. In 2019, Google demonstrated this with a quantum computer consisting of 53 superconducting qubits based on Josephson's junctions [7]. This demonstration gave motivation for further research into quantum computer systems. In analogy with classical computers where transistors are connected to make up a gate, which results in the basic operations of a computer *and*, *or*, and *not*, a quantum computer relies on quantum gates operating on one or two qubits [3].

The physical systems which are hosting the qubits for quantum computers must fulfill certain criteria. The qubit candidate must have long coherence times. Decoherence and short coherence times are one of the main challenges at the moment. The system should have the possibility

to be controlled, and it should be a two leveled quantum system with discrete energy levels. The system should be isolated from its surrounding environment and exhibit reliable read-out mechanisms, for example through photon emission [8][3]. It is also desirable that the qubit system has a material host which can be large-scale fabricated and integrated into devices.

Besides quantum computing, the other two main topics of QT (sensing and communication) are rapidly gaining attention. Today public key distribution (PKD) is a standard way to transfer information over a distance. The PKD utilizes mathematical problems that are easy to solve in one direction but difficult to compute in the other direction [9]. As mentioned, quantum computers may be able to solve complex mathematical problems like this, and the need for a communication method that is secure also from quantum computers is present. Quantum communication is a way to exchange information over long distances and keep it a secret from an uninvited third party. Polarized single photons are interesting for use in quantum communication and can travel long distances. The photons follow Heisenberg's uncertainty principle; if someone intercepts the data you're sending or receiving, the quantum state of the photon will be destroyed, and the eavesdropper will not be able to identify or understand the message. Quantum communication utilizes the superposition of two quantum states, meaning that if the information is detected or measured, it will result in the second state being destroyed.

Quantum sensors take advantage of a quantum system's high sensitivity to external perturbations. The central concept of a sensor is a probe that interacts with an appropriate system and the properties of interest will change the state of the probe. Measurements of the probe reveal the parameters that characterize the system. In quantum-enhanced sensors, the probe is generally prepared in a particular non-classical state. Quantum sensing employs a quantum mechanical system, entanglement, and coherence for the detection of, for example, weak electric and magnetic fields, as well as single molecules, with nanoscale spatial resolution [10]. A physical system suitable as a quantum sensor should have discrete energy levels, the ability to control initialization and state read-out, the ability to manipulate the sensor in a coherent manner using time-dependent fields, and finally, the system must interact with the physical quantity that is measured via a coupling parameter [11].

1.2 Material platforms for quantum technology

The physical implementation of a qubit for quantum computers must, as previously described, have long coherence times, minimum of two discrete energy levels, and isolation from its environment. Several promising qubit candidates which fulfill these criteria already exist. Some candidates include; **single photons**, exploiting the fact that the polarization state of the photon can be rotated to create single-qubit gates [12], **superconducting Josephson junction** realize qubits in electrical circuits and is the most common platform for quantum computing today, which is used by Google among others, **quantum dots**, realized by fabrication of nanostructures in semiconductors to make artificial atoms and create discrete energy levels, and **point defects in semiconductors**, which show features such as long spin coherence times, discrete energy levels and mature fabrication methods.

A semiconductor is a material with an intermediate forbidden energy gap between the conduction band and the valence band. Point defects, a non-native species, or an intrinsic fault in the lattice of semiconductors introduce energy states within the energy gap. *Deep-level* defects, meaning defects with energy levels situated near the middle of the energy gap, have a highly localized nature and may ensure the isolation and coherence needed for QT applications [3]. A deep-level defect suitable as a qubit should exhibit a system with at least two energy levels.

The nitrogen-vacancy (NV) center in diamond is the most well-known point defect acting as a qubit and started the research on point defects as qubits. Diamond has a large band gap and low spin-orbit coupling [13]. The negatively charged NV center has shown long coherence times and single-photon emission at room temperature [14]. However, diamond is costly in production and suffers difficulties in device integration, therefore other materials are investigated as possible qubit hosts. Semiconductors have the possibility of large-scale manufacturing with mature technology, and solid-state semiconductors may easily be integrated into devices. SiC marks itself as a promising candidate for QT as it has a wide band gap, low spin-orbit coupling, and long coherence times. SiC is structurally very similar to diamond and several promising quantum defects have been discovered in the industrially friendly 4H-SiC polytype. One of the most studied emitters in SiC includes the silicon-vacancy (V_{Si}) which possesses properties similar to those of the NV center [15][3]. V_{Si} in 4H-SiC will be the defect of interest for this thesis. Unfortunately, V_{Si} has relatively low emission intensities and no existing entanglement protocols, which are barriers that must be overcome before the V_{Si} can be utilized in quantum technologies. The use of nanopillars and other waveguides or cavity structures is a possible method to amplify the signal as well as isolate single defects and control them. Photonic structures are considered an essential approach to be used in components for QT.

1.3 Layout of the thesis

Numerical calculations of electromagnetic fields are a useful approach for understanding the emission from defects in nanostructures. The time-dependent Maxwell's equations form the basis of electromagnetism. Except in a few rare cases, finding analytic solutions to these equations is impossible. The Finite-Difference Time-Domain (FDTD) method, first introduced by Yee in 1966 [16], utilizes that the derivatives in Maxwell's equations can be written out as finite differences and can then be solved numerically for the time domain by iteration. The FDTD method can thus solve Maxwell's equations in both time and space. With numerical methods such as FDTD, the optical behavior of micro- and nanopillars can be studied before testing out physical structures in the lab. The FDTD method is used in this work to explore the electromagnetic fields from an ensemble of defects and from single emitters in nanostructures.

In this work, the impact of nanopillars on emission from V_{Si} will be investigated. With verification from experimental results obtained with cathodoluminescence and angle-resolved cathodoluminescence, the goal will be the development of a simulation method for single emitters in nanopillars in SiC using FDTD. Chapter 2 introduces the central theory and background for an understanding of features seen in quantum point defects, and 4H-SiC is presented as a

material platform for QT. This chapter also discusses photonic structures and gives an introduction to Maxwell's equations and modeling of electrodynamics with FDTD. In Chapter 3, the experimental methods will be introduced and the method development of the simulations will be explained. Finally, Chapter 4 will present and discuss experimental results. Thereafter follows a verification of the simulation method by comparison to experimental results, and lastly, we will present simulation results for nanostructures that were not yet practically realizable in the MiNa-lab. The work is concluded in Chapter 5, and further work for the investigation of V_{Si} emission in nanostructures is suggested.

Chapter 2

Theory

To understand why semiconductors can act as host materials for quantum technology, a solid understanding of semiconductor physics is required. This chapter will begin with an overview of semiconductors and defects in semiconductors before looking into how SiC nanostructuring can be used to enhance emission intensity and the directionality of the emission defect centers. Lastly, numerical calculations of electrodynamics with the Finite-Difference Time-Domain method are introduced. This chapter is based on the textbooks of Kittel [17] and Streetman [18].

2.1 Semiconductor physics

Semiconductors are electrically conductive materials that fall between metals and insulators. They have a fundamental band gap of energy where charge carriers are forbidden. This affects many of the material properties and permits semiconductors to be used in essential technologies, such as transistors and solar cells. This section will cover the theory behind the electronic properties of a semiconductor.

2.1.1 Crystalline materials

Solid materials are formed by closely packed atoms, held together by interatomic bonds. The nature of these bonds determines the properties of different solid materials. There are three types of bonding: covalent, ionic, and metallic. If the atoms occur randomly through the material without any long-range order, we say that the material is *amorphous*. If the atoms are ordered periodically over a long range, the material has a *crystalline* structure. *Polycrystalline* materials are composed of crystalline regions of different sizes and orientations. If the same periodicity is repeated over the whole solid, the solid is called a single crystal. The periodicity of a crystal is defined by the *lattice*, which is a symmetric array of points in space. The crystal lattice can be defined by three translation vectors $\mathbf{a_1}$, $\mathbf{a_2}$, and $\mathbf{a_3}$. Any point in the lattice can then be described by

$$\mathbf{R} = x\mathbf{a_1} + y\mathbf{a_2} + z\mathbf{a_3}, \tag{2.1}$$

where x, y, and z are integers and $\mathbf{R}$ is the translation vector of the lattice. The translation vectors are known as primitive lattice vectors, and they span the primitive lattice cell, which again spans the entire crystal through repetition. The understanding of crystal structure in crystalline materials supports the understanding of the rest of this chapter, concerning semiconductor physics and point defects.

2.1.2 Bandstructure of semiconductors

Electrons on a single atom have discrete energy levels, corresponding to the energy of the atoms' orbitals. As a consequence of Pauli's exclusion principle, stating that only one electron can occupy each orbital, the energy levels can not overlap when several atoms are brought together in a crystal. Instead, the energy of the orbital is shifted and the energy separation between them becomes infinitesimally small as the number of atoms in a bulk material increases. The energy levels are considered to form continuous "bands". The allowed energy levels, or bands, are separated by an energy gap where electrons are not allowed. As a result, electrons are not always confined to a single atom but occupy the energy bands.

The highest energy band occupied by electrons at 0 K is called the *valence band*, while the lowest unoccupied energy band at 0 K is called the *conduction band*. We typically refer to the lowest energy of the conduction band, E_C, and the highest energy of the valence band, E_V. The electronic properties of a material are to a large extent determined by these energies and by the energy difference E_g between E_C and E_V, which is called the band gap. Figure 2.1 illustrates how an insulator, a semiconductor, and a metal differ with respect to the energy bands and the size of E_g. Both the semiconductor and the insulator have a filled valence band and an empty conduction band at 0 K, they differ from each other by the size of the band gaps. At 0 K when the valence band is completely filled by electrons and the conduction band is completely empty the material is not able to conduct electricity. The size of the band gap of a semiconductor allows thermal and optical excitation across the band gap, which is needed to achieve electronic conduction. The band gap of an insulator is large, resulting in low probabilities for excitations across the band gap, and thus insulators do not conduct current. Metals have partially filled bands or bands that overlap, resulting in conductive materials with no need for electron excitation across the band gap.

Thermal excitation occurs in a semiconductor when the temperature is increased and electrons in the valence band gain enough energy to get *excited* into the conduction band. This process leaves an empty electronic state in the valence band, called a *hole*. We call the hole in the valence band and the electron in the conduction band an electron-hole-pair (EHP). A positive hole in the valence band and a negative electron in the conduction band are both considered *charge carriers* and can move in their respective energy bands. When EHPs are generated through the energy from photons, it is called an optical excitation.

For ideal materials with a periodic structure, the wavefunction of a single electron traveling through a periodic crystal has the form of a plane wave, with a propagation constant, $\mathbf{k}$, termed

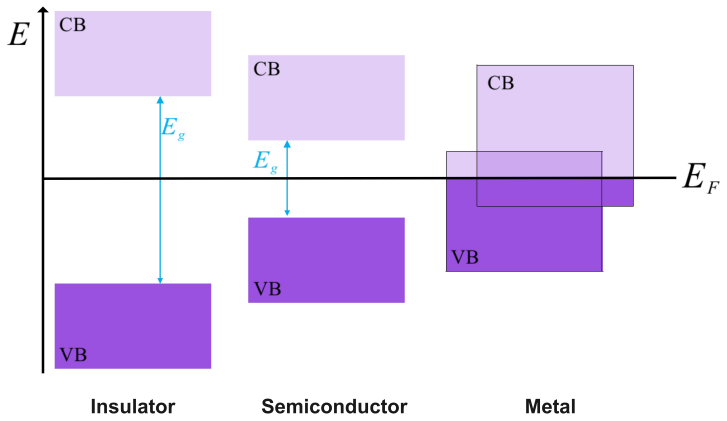

Figure 2.1: Schematic illustration of energy bands relative to the Fermi level for an insulator, a semiconductor and a metal. The dark areas represent filled states at 0 K. Metals differ from semiconductors by having partly filled, and overlapping energy bands.

the wave vector. The space-dependent wavefunction for a traveling electron can be written as

$$\Psi(\mathbf{r}) = u_k(\mathbf{r})e^{i\mathbf{kr}}. \tag{2.2}$$

Here $u_{\mathbf{k}}(\mathbf{r})$ is a Bloch periodic function that follows the periodic potential, $U(\mathbf{r}) = U(\mathbf{r} + \mathbf{R})$, of the lattice.

We separate semiconductors into *indirect* and *direct* band gap semiconductors. The band gap is considered to be direct when the valence band maximum and conduction band minimum are both associated with the same wave vector $\mathbf{k}$. When the valence band maximum and conduction band minimum are at different values of $\mathbf{k}$, this is known as an indirect band gap. Figure 2.2 illustrates the energy of the valence and conduction band in a direct band gap to the left and an indirect band gap to the right. An electron transition from $\mathrm{E_C}$ to $\mathrm{E_V}$ in a direct semiconductor can thus happen without any change in the momentum. The result of such an electron transition is a photon with energy close to $\mathrm{E_g}$. However, a transition of an electron in the indirect band gap involves a change in $\mathbf{k}$, which corresponds to a change in the electron's momentum and energy. This change often happens with the assistance of states in the band gap, $\mathrm{E_t}$ in Figure 2.2. These states are often a result of defects in the crystal. For example, SiC is an indirect band gap semiconductor which is important to keep in mind when looking at the emission spectra of SiC. The transition of an electron from $\mathrm{E_C}$ to $\mathrm{E_V}$ via a defect state happens with interaction with phonons which change the momentum of the electron. The energy of the emitted photons is thus not equal to the energy of the band gap.

The probability of a state being occupied by an electron can be calculated with the Fermi-Dirac distribution,

$$f(E) = \frac{1}{\exp\frac{(E-E_F)}{K_B T} + 1}. \tag{2.3}$$

$f(E)$ is the probability that a state with energy E is occupied by an electron at a temperature T and k_B is the Boltzmann constant. $\mathrm{E_F}$ is the Fermi level, which is an important quantity when

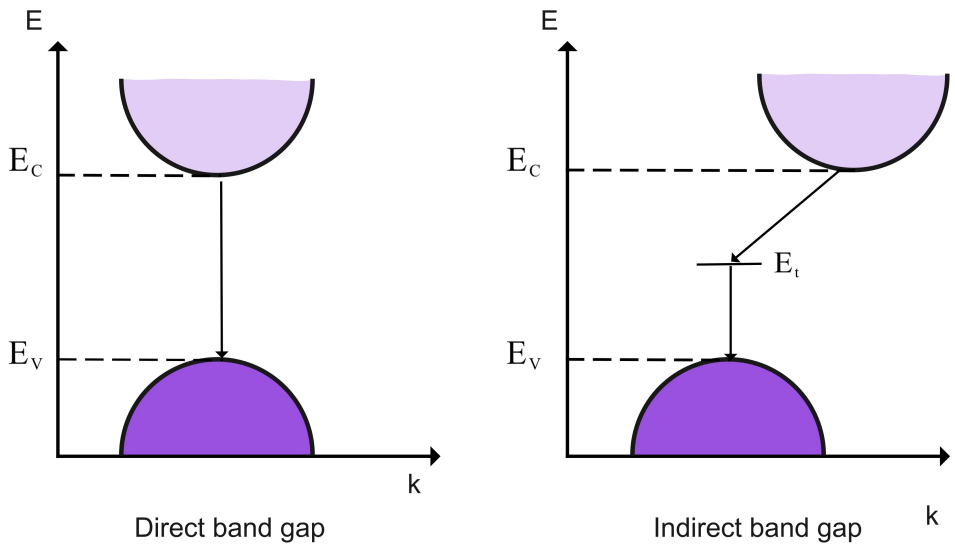

Figure 2.2: Transition of electrons in a direct and an indirect band gap. The transition in the indirect band gap goes through a defect state (E_t). Adapted from Streetman [18].

analyzing the behavior of semiconductors. The probability of E_F being occupied by an electron is equal to $\frac{1}{2}$. At 0 K, all energy states with $E < E_F$ are occupied by electrons, while the energy states with $E > E_F$ are unoccupied. If the temperature is increased the probability of occupation of states above E_F is increased. Figure 2.3 shows how the Fermi-Dirac distribution changes for the temperatures T_1 and T_2, where $T_2 > T_1 > 0$ K.

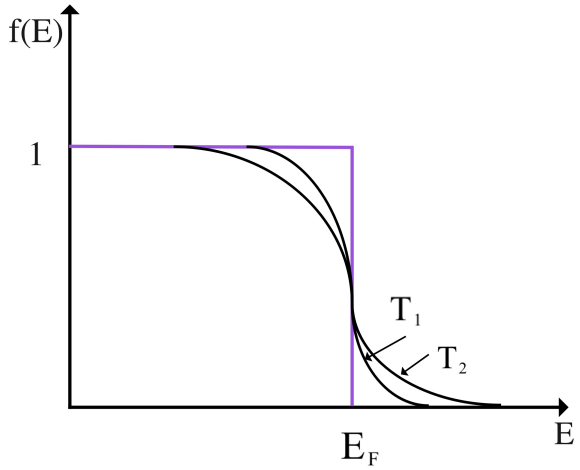

Figure 2.3: The Fermi-Dirac distribution at different temperatures, $T_2 > T_1 > 0$ K. The probability of states with energy above E_F being populated by electrons increases as the temperature increases. Figure adapted from Streetman [18]

The Fermi level in the semiconductor in Figure 2.1 is positioned in the middle of the band gap. We call this an *intrinsic* semiconductor and no electronic current is present at 0 K. With an increase in temperature, as explained above, the electronic conduction will increase. To increase the probability of EHP creation and increase the carrier concentration and again the electronic conduction, states can be intentionally introduced in the band gap by the introduction of a

foreign atom, this is called *doping*, and we then call it an *extrinsic* semiconductor. Doping also leads to an increase or decrease of E_F. An increase of E_F indicates that states near E_C are occupied by electrons and that the material is n-doped, meaning doped with an impurity atom with one valence electron more than the host atom. A decrease of E_F indicates that the material is p-doped with an impurity atom with one less valance electron than the host atom. p-type doping will give an increased concentration of holes in the valence band, while n-type doping will give an increased concentration of electrons in the conduction band.

2.2 Defects in semiconductors

The laws of thermodynamics explain that a perfect crystal without any symmetry-breaking flaw does not exist in real life [17]. These flaws are imperfections in the crystal lattice of a semiconductor and are called defects. Defects may contribute to the electrical and optical properties of a semiconductor. As mentioned in the introduction, point defects in semiconductors are promising candidates for qubits. Defects can be introduced by doping or by an unintentional introduction of foreign elements, which are called *extrinsic* defects. Elements present in the host material may also cause the formation of defects. These defects are called *intrinsic* defects.

Defects in crystalline materials can be grouped by their size. Relevant to this project are the 0-dimensional defects, termed point defects. Other defect types include 3-dimensional volume defects like precipitates, 2-dimensional planar defects like grain boundaries, and 1-dimensional defects with, for example, a line of point defects or dislocations. Point defects for use in quantum technology, such as quantum computers and networks, should exhibit the necessary properties such as (i) possibility to act as qubits based on either photon polarization or electron spin, (ii) gate operations applied to isolated spin systems and, (iii) single-photon emission for quantum state read-out and secure information transfer over large distances and within quantum computer systems [19].

2.2.1 Point defects

Point defects are divided into *vacancies, interstitial* and *substitutional* defects. Figure 2.4 schematically illustrates the three defect types in a crystal lattice. An empty lattice site that is supposed to host an atom is called a vacancy. Interstitial defects occur when there is an atom situated at voids in the lattice, in-between lattice sites. When an atom non-native to the perfect crystal occupies a crystal site, we have a substitutional defect. These three varieties can be combined and form point defect clusters, for example, a vacancy and a substitutional defect or a divacancy consisting of two neighboring vacancies.

A defect will influence the crystal structure surrounding it and may also attract charge carriers. The location of the defect level inside the bandgap affects the optical and electronic properties of a semiconductor. *Shallow* defects are found closer to either band gap edges ($\sim$ 0.2 eV). Holes or electrons associated with these defects are easily thermally excited and can contribute as charge carriers in either the conduction or valence band. Since the holes and electrons strongly interact with the band edges, the wavefunctions of shallow defect states are

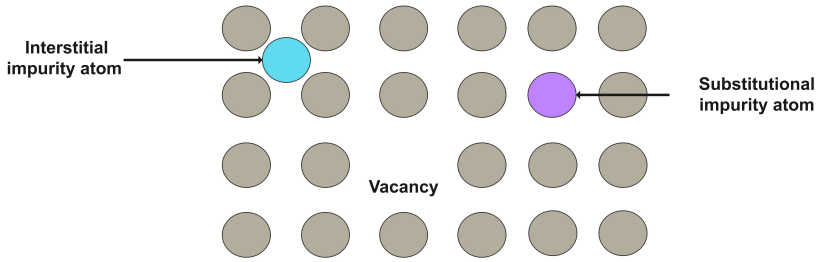

Figure 2.4: An interstitial, a vacancy and a substitutional point defect in a crystal lattice. The grey circles represent crystal atoms on lattice sites.

delocalized. *Deep level* defects are located closer to the middle of the band gap. They are deep in the sense that the energy required to remove an electron or hole from the defect state to the conduction or valence band is much larger than the characteristic thermal energy kT. Deep level defects have a *localized* wavefunction and often function as *traps* for charge carriers or as recombination centers for EHPs. A trap within the band gap can result in a lower free charge carrier concentration in the conduction band, and deep level defects contribute little to conduction in the material. Deep level defects, on the other hand, provide the isolation and coherence required for quantum technology due to their localized wavefunctions and are the subject of this thesis. It is desirable to obtain control of both the concentration and location of the defects in materials used for practical applications.

2.2.2 Defects states and recombination

As previously stated, deep level defects can capture electrons or holes. The energy level of the defect differs depending on which type of charge carrier it captures. Figure 2.5 illustrates a defect in the middle of the band gap which can capture electrons and holes. *Charge-state transition* levels are the energy levels related to these deep level defects and signify the transitions between charge states. Each defect can have more than one charge state, for example (+/0) and (0/-). The location of the Fermi level will define the steady-state occupancy of the charge state, i.e., if it is occupied by an electron or a hole. To explain the carrier capture of this deep level defect we assume that the defect level is situated close to the middle of the band gap and that the probability of capture of electrons and holes are similar. c_n and c_p are used for electrons and hole capture respectively, while e_n and e_p indicate the respective emission rate for electrons and holes. We can determine whether the defect acts as a recombination center or as a trap by considering the ratio between electron and hole capture. A recombination center will have $c_n \sim c_p$, while an electron trap will have $c_n >> c_p$ [3]. If light is emitted by recombination of excited electrons it is called *luminescence*. When studying defect emission related to QT, we are interested in transitions within one single charge state level of the defect, i.e., the defect should be in the same charge state during the excitation and recombination process. The luminescence from these processes does not involve movement of charge carriers in the crystal lattice, and the energy required to excite the electron from the ground state to the excited state is thus less than the energy of the band gap.

The so-called configuration coordinate model describes the recombination of localized charge

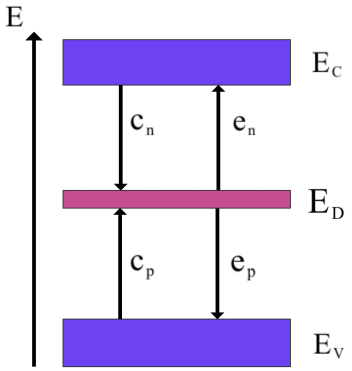

Figure 2.5: To the left is an illustration of carrier capture of a deep level defect. c_n, c_p and e_n, e_p respectively represent capture and emission rates for electrons and holes. To the right is an illustration of two different charge state transition levels for the defect. The location of E_F will define the stability of each charge state

carriers. It helps us understand the shape of the optical spectra and how phonons participate in luminescence processes. The model is illustrated in Figure 2.6 and represents the defect's potential energy relative to Q which represents the atom displacement from the equilibrium position of the defect center. The rearrangement of atoms during the excitation and relaxation induces small changes in the positions of the atoms. When the atoms are relaxed back to their equilibrium positions a photon is emitted together with several phonons [20]. The configuration coordinate Q is generally a combination of vibrational modes of the crystal structure around the defect. However, for technical simplification of the configuration coordinate model, Q is reduced from a three-dimensional unit to one dimension [21]. The optical transition of a charge carrier to an excited state is much faster than the phonon frequencies in the lattice from the motion of atoms. The transition from the ground state to the excited state is in the model, therefore, represented as a vertical transition without change in the atom's position. The transition process can be described in four steps, labeled in Figure 2.6. At first (1) an electron absorbs the energy of a photon and is excited into the excited state (a vertical transition, i.e., without changing the atomic configuration) represented by the upper parabola. The system then relaxes to the lowest point of the excited state (2) by phonon interactions. Eventually, the system relaxes back to the ground state by emitting a photon with the energy corresponding to the vertical line (3). Finally, the system is by interactions with phonons relaxed back to the zero-vibrational level of the ground state, located at the bottom of the parabola, and the lattice arrangement is back to its original. The cycle is then repeated.

Due to interactions with phonons, some transition energy is lost, leading to a reduction of the radiation energy. When the electron transitions directly from the lowest excited state to the bottom of the ground state the resulting emission intensity is called a zero-phonon line (ZPL). The energy associated with the ZPL, E_{ZPL}, gives rise to a sharp peak in a luminescence spectrum. Energy transitions involving phonon interactions will result in lines at different energies than the ZPL or broader bands called phonon side-bands (PSB) in the same spectrum. The ZPL could be hidden by the PSBs in the spectrum if the phonon-electron coupling is strong [3][20]. Defects that are characterized by such a distinguishable ZPL and simultaneously emit one photon at

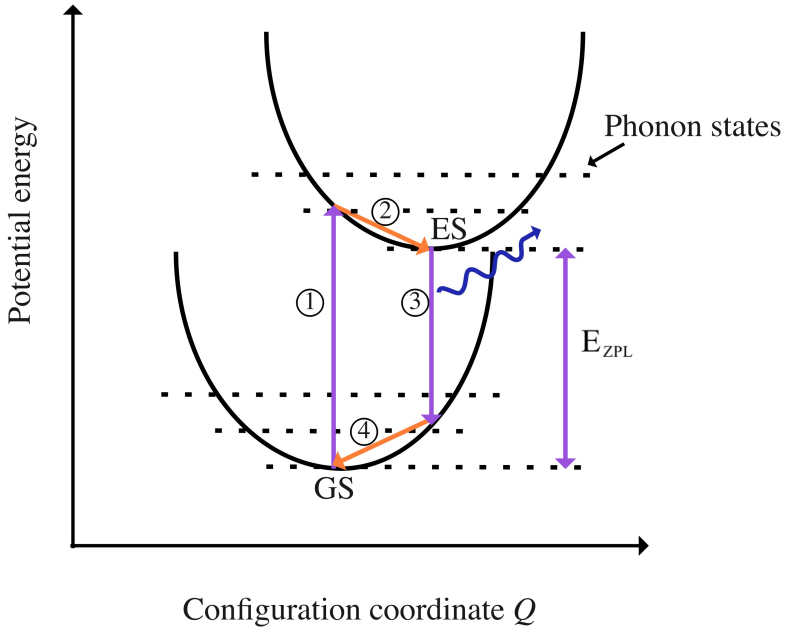

Figure 2.6: Configuration coordinate model for a defect-related transition from the ground state (GS) to the excited state (ES). Based on Ref. [21].

a time by a direct transition from ES to GS are called single-photon emitters (SPE) and are discussed more in detail below.

In addition to emission from a localized energy transition, other luminescence processes may happen in a semiconductor. As mentioned an electron can transition from E_C to E_V in direct and indirect band gaps. Such transitions will give peaks in an emission spectrum and indirect band gap semiconductors will have broader emission peaks representing the band gap. Recombination of an EHP can also occur between defect states and the band edges. Luminescence peaks from recombination with deep level defects and band edges will typically have strong intensities and might make quantum defect emission harder to detect in a luminescence spectrum.

2.2.3 Single-photon emitters in semiconductors

Defects that facilitate the ZPL described above are called single-photon emitters (SPE) and have an energy transition of a localized charge carrier directly from the excited state to the ground state. The photons from a SPE are emitted one at a time with a temporal delay between each occurrence [3]. For efficient spin-photon entanglement and scalable quantum information systems, reliable single-photon emission is essential. Only some defects and material types possess SPEs. Transitions that involve interactions of charge carriers with the valence or conduction band will give broader peaks and materials suitable for SPEs often have a wide band gap. Thus the large band gap of 4H-SiC is advantageous. Silicon is also a suitable candidate but its narrow band gap is problematic.

Long coherence times and ambient working temperatures are two aspects of SPEs present in semiconductors that make them ideal for quantum applications. [3] Bathen summarizes the

criteria for the semiconductor host of an SPE [3]. In addition to the presence of a wide band gap, the criteria include having a localized wavefunction for the charge carrier associated with the defect, which means it is isolated from the environment. The semiconductor should also have a point defect with one or more energy levels deep within the band gap. The SPE should furthermore have a weak electron-phonon coupling to ensure sharp emission peaks.

A Hanbury-Brown-Twiss interferometer is used for experimental measurements of whether a defect that emits photons is also an SPE. The interferometer consists of a beam splitter that splits the beam coming from a defect into two paths. Both paths end in single-photon counting detectors where the correlation or anti-correlation of the emitted photons are measured. For an ideal SPE, only one of the detectors will count a photon at a given time. A histogram can be created from the time delays between the detection of single photons. The correlation of the intensities observed at each detector is described by a second-order correlation function $g^{(2)}(\tau)$. One assumes a single-photon emission if $g^{(2)}(0)$ is seen to be less than 0.5 [22].

2.3 4H-SiC as host for quantum technology

The nitrogen vacancy (NV) center in diamond is the most studied point defect for quantum technology. The defect consists of a substitutional nitrogen atom next to a carbon vacancy and emits in the visible part of the spectrum. It has shown desired properties for quantum technology as it emits single photons and has long coherence times [19]. Due to diamond's difficulties in large-scale manufacturing and device integration, other materials are pursued as hosts for qubit candidates. With a mature fabrication technology and easier device integration than diamond, SiC appears to be a strong contender. Point defects that facilitate the sharp ES-to-GS transitions characteristic of an SPE have also been found in SiC. Defects in SiC have shown emission in the infrared and near-infrared region and are more compatible with wavelengths suitable for quantum communication and integration with fiber optics than the NV center in diamond which emits photons with wavelengths in the visible region. This section introduces the crystal structure and the silicon vacancy in 4H-SiC.

Crystal structure and defects in 4H-SiC

Silicon carbide is available in a variety of polytypes, which relate to distinct SiC crystal structures. The most utilized varieties in technology are 4H-SiC and 6H-SiC, both of which have a hexagonal structure, and 3C-SiC, which has a cubic structure. The 4H-SiC polytype is the most common polytype of all, used, e.g., in commercial power electronic devices. This polytype is the subject of this thesis. 4H-SiC also has the largest band gap of 3.26 eV [23]. The large band gap makes it easier for an SPE within the band gap to make a sharp ES-to-GS transition which is desirable for a qubit point defect.

The structure consists of carbon and silicon atoms in equal amounts that are covalently bonded together. The structure is bilayered stacked in an ABCB... sequence. Figure 2.7a shows the crystal stacking, while Figure 2.7b illustrates the hexagonal unit cell. The unit cell of 4H-SiC is hexagonal and the atoms take two inequivalent lattice sites, the hexagonal (h) and the

pseudo-cubic (k) [3].

There are many different defects in SiC. The most relevant for this thesis is the silicon-vacancy (V_{Si}). The V_{Si} is promising in terms of quantum technology and will be discussed further below. Other defects suited for quantum technologies that will only briefly be introduced here include the divacancy ($V_{Si}V_C$), with six ZPLs in infrared regime ($\sim$ 1100 nm) [24], the nitrogen vacancy center ($V_{Si}N_C$) which emits light in the near-telecom band [25] and the carbon antisite-vacancy pair, $C_{Si}V_{Si}$ (CAV). Both $CAV^{(-)}$ and $CAV^{(+)}$ have been identified in 4H-SiC. $CAV^{(+)}$ has four different configurations (*hh, kk, hk* and *kh*). Each configuration has two excited states, giving rise to a total of eight ZPLs. All ZPLs were identified by Ref. [26] and found in the 658-677 nm range.

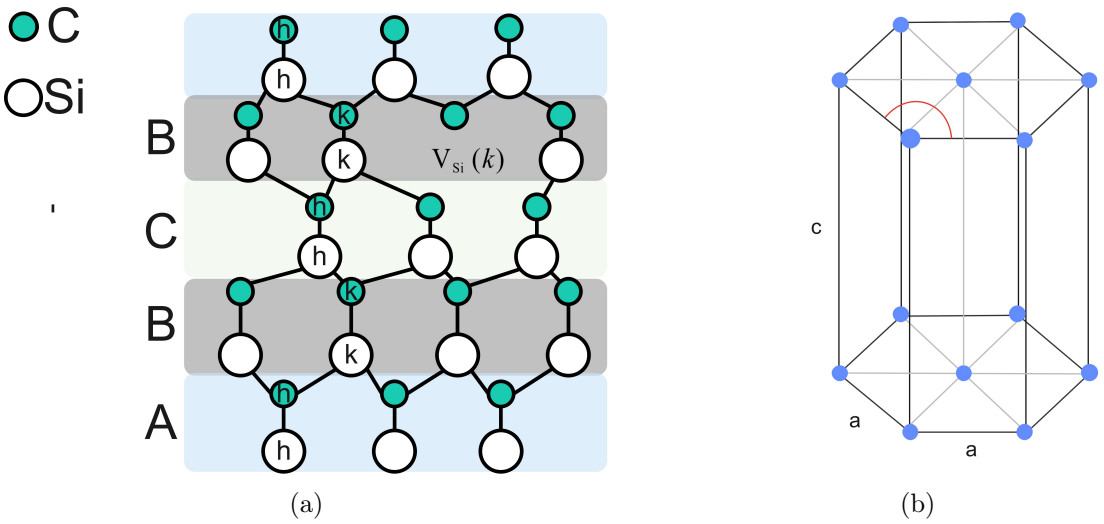

Figure 2.7: Figure (a) illustrates the 4H-SiC crystal structure with a silicon-vacancy on a pseudo-cubic (k) lattice site, while (b) illustrates the hexagonal unit cell

The silicon-vacancy in 4H-SiC

The V_{Si} is a well-known defect in 4H-SiC and it has been identified as a room-temperature SPE. With coherent spin control, it is a promising point defect for quantum technology applications. Since the structural sites in 4H-SiC have two different symmetries (k and h), defects at different symmetries will give rise to different local environments. Both V_{Si} configurations exists in three different charge state transition levels. Figure 2.8 shows the different energy levels for a hexagonal and a pseudo-cubic V_{Si}. The colored region in the figure corresponds to the negatively charged V_{Si}, which is the quantum compatible charge state of V_{Si} for both configurations. The V_{Si}^- exhibit both a high-spin ground state and single-photon emission while the other charge states remain dark and exhibit no identified spin signals [27]. The different defect configurations will lead to different ZPLs. The V1 ZPL is associated with the hexagonal environment of V_{Si}^-, while the V2 ZPL is associated with the pseudo-cubic environment; both exhibit single-photon emission and millisecond spin coherence times [26]. The hexagonal V_{Si}^- also exhibits emission from a higher-lying excited state which gives rise to a third ZPL, the V1'. The three ZPLs of V_{Si}^- are 862

nm (V1), 858.2 nm (V1') and 918 nm (V2). The V_{Si}^- also has the ability for optical monitoring and coherent manipulation of the spin state and therefore is a promising candidate for quantum technology [26]. Emission lines in the near-infrared region also make V_{Si}^- suitable as a quantum sensor in biological or medical science.

Since V_{Si}^- is the only quantum compatible charge state of the silicon vacancy, it is important to achieve the right position of the Fermi level for achievement of the highest possible signal. Control of the charge state is possible via fabrication of Schottky barrier diodes and this has shown enhanced emission from V_{Si}^- [27]. The Debye-Waller (DW) factor is the ratio of the emitted light from the ZPL to all the emitted light. Ref. [28] found a DW factor of $\sim 6\%$ for V_{Si}^-. For implementation in quantum communication, a high DW factor is necessary. Enhanced emission from V_{Si} can be realized by nanofabricated waveguides or implementation into photonic crystal cavities. Implementation of V_{Si} in cylindrical nanopillars have showed increased emission intensities [29]. The next section presents and discusses radiation from such photonic structures.

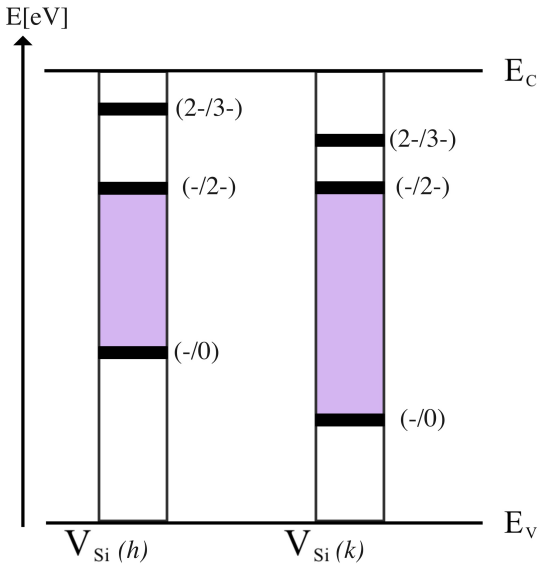

Figure 2.8: Charge states in the 4H-SiC band gap for V_{Si}. The colored regions indicate the quantum compatible charge state V_{Si}^- for each defect configuration. Figure adapted from Ref. [19]

2.4 Nanopillars as waveguides and other photonic structures

An optical waveguide is a structure that uses total internal reflection (TIR) at dielectric surfaces to confine and guide light. For TIR to happen the waveguide should have a larger refractive index compared to the material surrounding it. The refractive index is a measure of the capability of a material to guide light rays when traveling from one medium to another. In addition, the angle of incidence should be greater than a critical angle which depends on the media the light is traveling in [30]. Waveguides can be used as a photonic device to increase the collection efficiency from defect emission by directionalizing the emission. We define collection efficiency as the number of collected photons relative to the number of emitted photons.

Inside a non-structured material, a defect with SPE features will randomly emit photons in all directions. The direction of electromagnetic radiation from the SPE can be very different by tuning the material's structure to a waveguide. The electromagnetic waves in a structure in a size domain much larger than the propagating wavelength can be considered as rays and can be guided by TIR. This is similar to how lenses and mirrors alter visible light. The process then follows the principles of *Geometrical Optics*. Figure 2.9 shows how a cylindrical waveguide and a hemisphere or a solid immersion lens (SIL) in a size domain much larger than the wavelength will alter the light out of the structures. Depending on the refractive index of the material, rays incident on the material/air interface with a larger angle than the critical angle will be subjective to TIR. The numerical aperture of the SIL in Figure 2.9b will be increased compared to a flat surface. The light will refract depending on where it interact with the curved interface.

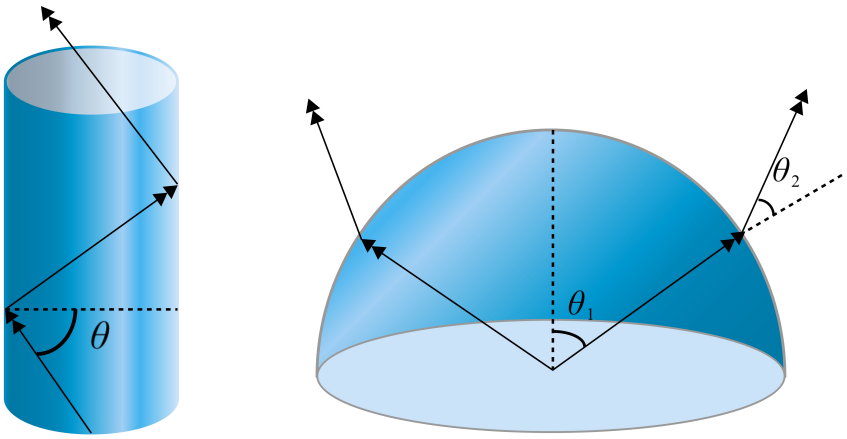

Figure 2.9: Schematic representation of (a) how light is guided through a cylindrical structure with a high refractive index, and where θ is larger than the critical angle, and (b) how the numerical aperture is increased for a solid immersion lens.

As long as the diameter of the waveguide is much larger than the wavelength of the emitted photons, we need not consider the wave nature of propagation. However, for QT applications waveguides in the same size domain as the wavelength of the emitted light is particularly interesting. The wave nature of photons must be considered when approaching this size domain. For structures in this size domain, a wave that is reflected more than one time inside a perfect waveguide reproduces itself and we are left with only two distinct plane waves. Electromagnetic waves that travel in discrete sets like this are known as *modes*. Modes are fields that maintain the same transverse distribution and polarization at all distances along the waveguide axis [31]. The number of modes in a waveguide depends on the wavelength, as well as the size of the waveguide. By solving *Maxwell's equations* for the physical parameters and boundary conditions of the system the modes can be found. If the dimension of the waveguide is half the size of the traveling wavelength the electromagnetic waves will travel as one mode. If the wavelength is decreased the number of modes will increase. The modes are both transverse electric (TE) and transverse magnetic (TM) waves. These modes can be found in [30] [32]. A commonly used waveguide is optical fibers which are cylindrical waveguides used in modern telephone and

computer communication. An optical fiber consists of a high refractive index dielectric material core surrounded by a dielectric with a lower index and the light travels through the fiber in the form of modes. The nanostructures considered in this project can be considered cylindrical waveguides similar to optical fibers. However, the nanostructures are surrounded by air, not a solid.

In a case where the distance between two waveguides is sufficiently small such that their fields overlap, light can be coupled from one and into the other [31]. This effect can be used to transfer electrical signals, called optical coupling. Coupling between waveguides can be considered a scattering effect. The light can differ between which waveguide it is mostly located, and also be divided equally between the waveguides. For quantum technology, coupled waveguides can collect and transfer the emitted photons from one quantum emitter to another one. In this project the distances between the nanostructures we study are large but coupling between SiC nanostructures might be useful for implantation on quantum photonic integrated chips [33].

Since SiC has a high refractive index (n $\sim$ 2.6 [34]), it exhibits considerable refraction and total internal reflection at the SiC-air interface, reducing the amount of defect luminescence collected. This combined with SiC being a promising host for SPEs has led to various research on how to enhance the collection efficiency of the luminescence emission. One of the most commonly implemented approaches for improving the collection efficiencies is the fabrication of a SIL on top of the emitter. Sardi *et. al.* [35] have demonstrated a scalable approach for the manufacturing of SILs on 4H-SiC. They found no correlation between the size of the lens and the enhancement of the V_{Si} emission. However, placing V_{Si} in the apex region significantly improved collection efficiency [35]. Arrays of nanopillars have improved manufacturing simplicity compared to SILs. Radulaski *et al.* have demonstrated that waveguiding in 4H-SiC nanopillars increases photon counts per second by three times for cylindrical waveguides with 600 nm and 1000 nm width and an 800 nm height [29]. The investigation of how the emitter's position within a photonic structure as well as the size and shape of a nanopillar influences the emission intensity and directionality is one of the main focus areas of this thesis.

2.5 Modelling computational electrodynamics

Numerical calculations of electromagnetic fields are interesting when studying luminescence from nanostructures. The Finite-Difference Time-Domain (FDTD) method is a numerical analysis technique used for modeling computational electrodynamics by solving Maxwell's equations. The FDTD method can be applied to many problems of propagation, radiation and scattering of electromagnetic waves. In this project, FDTD is used to model emission from SPEs in SiC nanostructures.

2.5.1 Maxwell's equations

Maxwell's equations describe how electric charges and electric currents create electric and magnetic fields. They also describe how an electric field can generate a magnetic field. Mathematically, Maxwell's equations relate the volume charge density ρ to the volume current density $\mathbf{J}$,

and four vector field magnitudes: the dielectric displacement field $\mathbf{D}$, the electric field $\mathbf{E}$, the magnetic flux density $\mathbf{B}$ and the magnetic field $\mathbf{H}$. Gauss' law for the electric and magnetic field is

$$\nabla \cdot \mathbf{D} = \rho \quad \text{and} \quad \nabla \cdot \mathbf{B} = 0, \text{ respectively.} \tag{2.4}$$

The dielectric displacement field can be related to the electrical field trough the electrical permittivity, ϵ:

$$\mathbf{D} = \epsilon \mathbf{E} \tag{2.5}$$

A change in the magnetic flux density will induce an electric field, this is expressed by Faraday's law,

$$\nabla \times \mathbf{E} = -\frac{\partial \mathbf{B}}{\partial t}. \tag{2.6}$$

The last equation is Ampere's law which expresses that a magnetic field is produced by an electric current and an electric field that changes with time. Ampere's law is given by:

$$\nabla \times \mathbf{H} = \mathbf{J} + \frac{\partial \mathbf{D}}{\partial t}. \tag{2.7}$$

The magnetic field $\mathbf{H}$ can be written as

$$\mathbf{H} = \frac{1}{\mu}\mathbf{B}, \tag{2.8}$$

where μ is the magnetic permeability. Substitution of equation 2.5 and 2.8 into Faraday's and Ampere's law respectively, gives

$$\frac{\partial \mathbf{H}}{\partial t} = -\frac{1}{\mu}\nabla \times \mathbf{E}, \tag{2.9}$$

$$\frac{\partial \mathbf{E}}{\partial t} = \frac{1}{\epsilon}\nabla \times \mathbf{H}. \tag{2.10}$$

These two equations can be written out as six coupled partial differential equations and form the basis of the FDTD numerical algorithm [36].

2.5.2 The Yee algorithm

The FDTD method was first introduced by Yee in 1966 [16]. He utilized that coupled differential equations from Maxwell's equations can be written out as finite differences and solved numerically for the time domain by iteration. Yee proposed spacial gridding to solve Maxwell's equations which are called the Yee cell. The Yee cell defines the spacial grid points for the **E**-field and the **H**-field. The grid is specifically intended to solve the curl components in Maxwell's equations and ensures that the curl is approximated on the same plane as the relevant vector component. The resulting differential equations for **E** and **H** are solved on the grid points to obtain "update equations" that express the (unknown) future fields in terms of (known) past fields [37]. For an illustration of how the Yee cell makes calculations of the magnetic field easier, Figure 2.10 shows how the **E**-components are along the edges and the **H**-components are shifted by a half step and calculated in the center of the faces. The same holds for the calculations of the **E**-components, which are calculated by the surrounding **H**-components along the edges. The calculation in time

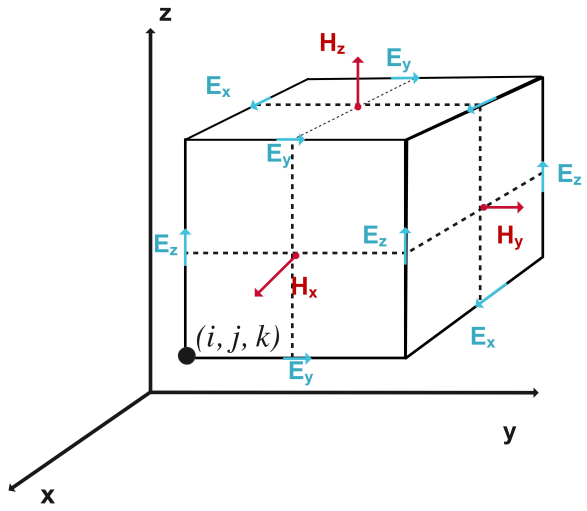

Figure 2.10: The Yee Cell with the associated **E** and **H** fields identified at the edges and surfaces [16]

then follows the same pattern as the fields and the **E**-fields are updated at half-integer time steps, while the **H**-fields are updated at integer time steps. For example, the E_x component in three dimensions is located at half x and integer y and z grid positions, i.e., $(i+\frac{1}{2}, j, k)$, while the E_y component is located at $(i, j+\frac{1}{2}, k)$. The magnetic field follows the opposite pattern, so H_x is calculated at $(i, j+\frac{1}{2}, k+\frac{1}{2})$. During the computation cycle the **E**-field is computed using stored **H**-field data and the **E**-field from the previous time step n. The E_x component is calculated with H_z and H_y components from the previous time step, such that:

$$\mathrm{E}_x|^{n+1}_{i+\frac{1}{2},j,k} = \mathrm{E}_x|^{n}_{i+\frac{1}{2},j,k} + \frac{\Delta t}{\epsilon_{i+\frac{1}{2},j,k}}\left[\frac{\mathrm{H}_z|^{n+\frac{1}{2}}_{i+\frac{1}{2},j+\frac{1}{2},k} - \mathrm{H}_z|^{n+\frac{1}{2}}_{i+\frac{1}{2},j-\frac{1}{2},k}}{\Delta y} - \frac{\mathrm{H}_y|^{n+\frac{1}{2}}_{i+\frac{1}{2},j,k+\frac{1}{2}} - \mathrm{H}_y|^{n+\frac{1}{2}}_{i+\frac{1}{2},j,k-\frac{1}{2}}}{\Delta z}\right]. \quad (2.11)$$

The E_y and E_z components are computed in the same manner with respectively the H_z, H_x and H_x, H_y components. Then the same method is used for the **H**-field which are computed with the **E**-field data just computed [38] [36]. Thus the **H**-field at time step n and the **E** field at time $n+\frac{1}{2}$ is given by:

$$\mathbf{H}^0 \to \mathbf{E}^{\frac{1}{2}} \to \mathbf{H}^1 \to \mathbf{E}^{\frac{3}{2}} \to \mathbf{H}^2 \to \mathbf{E}^{\frac{1}{2}} \to \cdots \to \mathbf{H}^n \to \mathbf{E}^{n+\frac{1}{2}}. \quad (2.12)$$

The cycle is continued until all the fields are zero or converged within a cut-off-value at $\sim 1\times10^{-6}$ and the simulation is stopped.

Before one conducts FDTD simulations, several decisions about settings like initial boundary conditions, structure attributes and initial source settings must be made. Field monitors that

collect the outputs of the FDTD algorithm are also required for the simulation. Chapter 3 gives an introduction to the layout of the simulation and discusses features such as monitors, mesh and perfectly-matched layer (PML) boundary conditions. Convergence tests of these parameters have also been performed. The simulations are performed using the FDTD solver in ANSYS Lumerical Software [39]. This software provides a simple graphical user interface, a well-developed scripting language as well as standard settings for simulation properties such as boundary conditions and mesh size.

Chapter 3

Methods

Nanostructures with implanted defects are characterized with cathodoluminescence and angle-resolved cathodoluminescence, which both are techniques that can be included in a scanning electron microscope. These techniques are presented in this chapter. Simulation properties such as mesh and boundary conditions, essential for modeling with FDTD are introduced, discussed, and tested for convergence. The method developed for simulations of an ensemble of defects in SiC nanostructures is described.

3.1 Samples and defect formation

Presented first in this chapter are the structures used for optical characterization. The ion implantation technique for the formation of defects is explained and numerical calculations used to project the location of V_{Si} are presented.

3.1.1 Sample fabrication

The nanopillars that are studied with cathodoluminescence and replicated in the simulations were processed by an earlier master student (Ref. [12]). The main process steps are described herein.

Photolithography is a technique used to define and transfer geometric patterns of electronic devices from a photomask onto the substrate. The process consists of three main steps. Firstly, the sample is coated with a resist, often a mixture of organic compounds. The resist is then exposed to UV light while covered by a mask with the desired pattern, and the technique is thus called *photo*lithography. The light exposure may lead to a more soluble resist in the areas not covered by a mask, or the opposite, lead to hardening of the uncovered resist. The first is called a positive resist, and the resist will dissolve chemically during the third lithography step, etching. The latter refers to a negative resist, and the non-exposed resist will dissolve during etching. In order to form a metal pattern on the wafer after the photoresist pattern has been developed a method called lift-off is used. A metal layer is deposited on the wafer before it is placed in an ultrasonic acetone bath. The areas containing photoresist are removed and the metal is left on

the exposed areas.

Reactive ion etching (RIE) was used by [12] to achieve the vertical nanostructures on the wafer. RIE is a form of dry etch where a plasma of reactive gases is bombarding the substrate. Ions accelerated by an electric field will break bonds in the sample and create volatile species which are ventilated out from the etching chamber. The structures were fabricated by deposition of a SiO_2 layer with plasma chemical vapor deposition on a 4H-SiC wafer. Then after photolithography, RIE was used to pattern the SiO_2 layer. Finally, the SiO_2 layer was used as a mask for the RIE of the final nanopillars. The structures fabricated with this process were proven in [12] to enhance the emission intensity of the V_{Si}^-.

Images of the nanopillars obtained from a scanning electron microscope are shown in Figure 3.1. The pictures of the pillars from a side view are also used to measure the radius on top and bottom so similar structures could be simulated with FDTD. The measured sizes of the pillars in the figures are (a) 1.4 μm, (b) 1.9 μm, (c) 2.4 μm and (d) 2.4 μm. As the size of the pillar increase, the sidewalls become more straight, while the small pillars have a higher degree of tilted sidewalls. As seen in the images, some pillars also showed a tail on parts of the sidewalls, this was especially the case for the pillars with r = 1.4 μm.

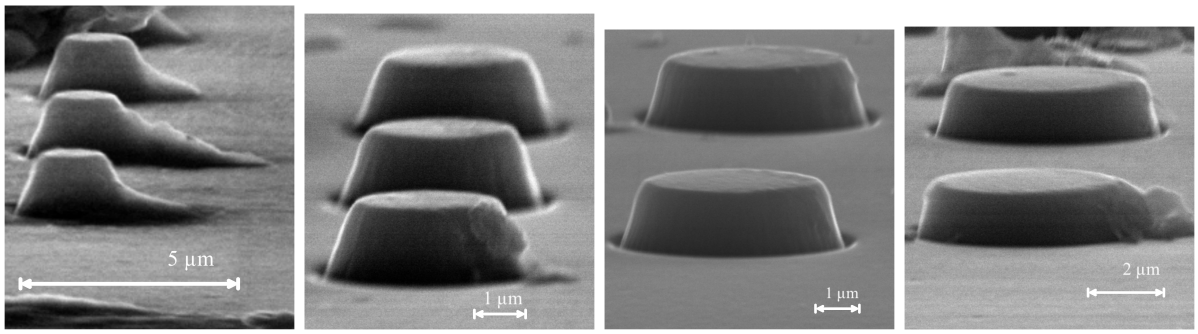

(a) (b) (c) (d)

Figure 3.1: SEM pictures of nanostructures with measured radius (a) 1.4 μm, (b), 1.9 μm (c) 2.4 μm and (d) 2.9 μm.

3.1.2 Ion implantation

Native defects are always present in materials however, for further introduction and control of the defect location and concentration, ion implantation is a common method. For this thesis ion implantation was employed to produce the intrinsic V_{Si} on-demand. Ions that are extracted from a solid or gas source are accelerated by an electric field towards a target. Typically the energies of the ions range from a few keV to several MeV. The depth, or the projected range, and the distribution of the ions are determined by the ions' energies and the angle of the incident ion beam. The number of ions present in the target after implantation is controlled by the time in which the sample is exposed to the ion beam, termed the fluence of ions. When the ions enter the target they interact elastically with the atoms in the lattice. The ions will lose their kinetic energy during the scattering events and finally come to rest. A random collision of ions gives a Gaussian distribution of implanted ions with the peak at an average projected range. *Channeling*

occurs if the incident ions follow open pathways through the crystalline material, if this happens the distribution of ions will no longer be random. Thus, to obtain the Gaussian distribution, the ion channeling should be suppressed by making sure the incident angle of the ion beam is not parallel to the crystal plane [3].

3.1.3 Defect formation

For the formation of V_{Si}, the samples used in this project were implanted with 21 kV He ions at an incident angle of 7° and with a fluence of 1×10^{11} cm^{-2}. A possible formation of the silicon vacancy may occur via the formation of a Frenkel pair (i.e., V_{Si} + Si_i). The Frenkel pair could either recombine and leave the lattice in its original arrangement. Or the Si interstitial could gain enough kinetic energy from the collision event to leave the interstitial site, resulting in an isolated silicon vacancy. Heat treatment of an ion implanted material can lead to defect migration or transformation into defect complexes like the $V_{Si}V_C$ and CAV in 4H-SiC.

The control over the distribution of implanted defects and the lattice damage is important when conducting defect studies. The relation between the change in ion energy and the distance traveled is called the stopping power and is used for the interactions between the implanted ions and the lattice atoms and electrons. From this, we can gain information about the depth of the implanted defects. The ion range and vacancy generation in the material can be simulated using Monte Carlo calculations as implemented in the SRIM code (the Stopping and Range of Ions in Matter [40]). Results from the SRIM simulation of 21 keV He ions with an incident angle of 7° in SiC are shown in Figure 3.2. The concentration of V_{Si} can be predicted after ion implantation, the displacement energy was set to 15 eV for the SRIM results presented here. Figure 3.2a shows the distribution of He ions, while Figure 3.2b shows the expected number of V_{Si} per angstrom relative to the depth in the material. The V_{Si} is expected to be found from the surface and until a depth of 200 nm below the surface, with the highest concentration at $\sim$ 150 nm. The projected range of He also has its peak at 150 nm. One should note that the SRIM simulations only present initial damage events. Dynamic annealing, which refers to the healing of damage to the lattice while the implantation process still occurs, is not accounted for in the SRIM simulations. This makes the point defects more mobile, and for most semiconductors, the percentage of vacancies that survive dynamic annealing is within 2-5% [3].

3.2 Scanning Electron Microscopy

One of the most frequently used instruments for studying the microstructure and morphology of materials is the scanning electron microscope (SEM). SEM images are created by scanning a focused electron beam (e-beam) over a surface and then detecting outgoing electrons generated by the e-beam. Unlike a light microscope, where the wavelength of the incident light is the limiting factor, an electron microscope can achieve higher resolutions as the resolution is instead dependent on the width of the incident e-beam, which can be as small as 10 nm. The electrons in the beam interact with the sample, generating different signals used to determine surface topography and composition. Some setups can also detect signals containing information about the optical properties of the sample. Figure 3.3a shows the various signals obtained from

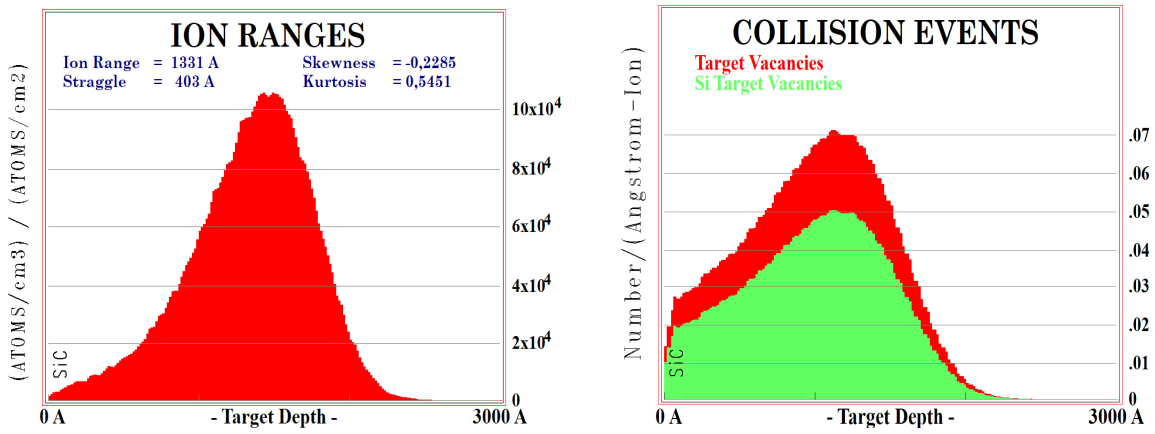

(a) (b)

Figure 3.2: Simulation results from SRIM with 21 keV He implantation at a 7° incident angle. Figure (a) shows the projected range of ions, while (b) shows the number of V_{Si} per angstrom relative to the depth in the material.

interaction with an e-beam.

To obtain a SEM image, we are dependent on two main processes, *backscattered electrons* and *secondary electrons*. Backscattered electrons result when the incident electron scatters and gets re-emitted at an angle greater than 90° by the atoms in the sample. Such scattering processes can occur hundreds of nanometers below the surface. Thus backscattered electrons give us information about the bulk properties of the material. SEM images formed from backscattered electrons also contain information about the chemical composition of the material.

Signals resulting from secondary electrons provide information about the surface topography. These electrons are generated in the sample when an incident electron has enough energy to emit an electron from an atom in the sample, forming a secondary electron. The secondary electron then travels through the sample towards the detector. The electron travels through the material, and several inelastic collisions with other atomic electrons will occur, leading to a loss in the electron's kinetic energy. As a result, only the secondary electrons generated a few nanometers below the surface will be able to escape the sample and can be captured at the detector. The kinetic energies of secondary and backscattered electrons are different since the majority of the backscattered electrons conserve most of their energy. This energy difference makes it easy to distinguish between the electron signals [41]. The SEM uses secondary electrons and electron backscattering detectors to image the sample. Other signals obtained when focusing the e-beam on the sample are characteristic X-rays, auger-electrons, and cathodoluminescence.

Figure 3.3b shows the main parts of the SEM set up with the e-beam generated from a heated LaB_6 filament. The electrons are accelerated by the potential difference between the filament acting as the cathode with high negative potential, and an anode with a ground potential. Acceleration voltages of 0.5-30 kV are obtainable for the e-beam. The condenser lens and the objective lens rely on electromagnetism to focus the e-beam. A magnetic field focuses the beam through an axis to get a narrow and coherent e-beam in the condenser lens. Before hitting the

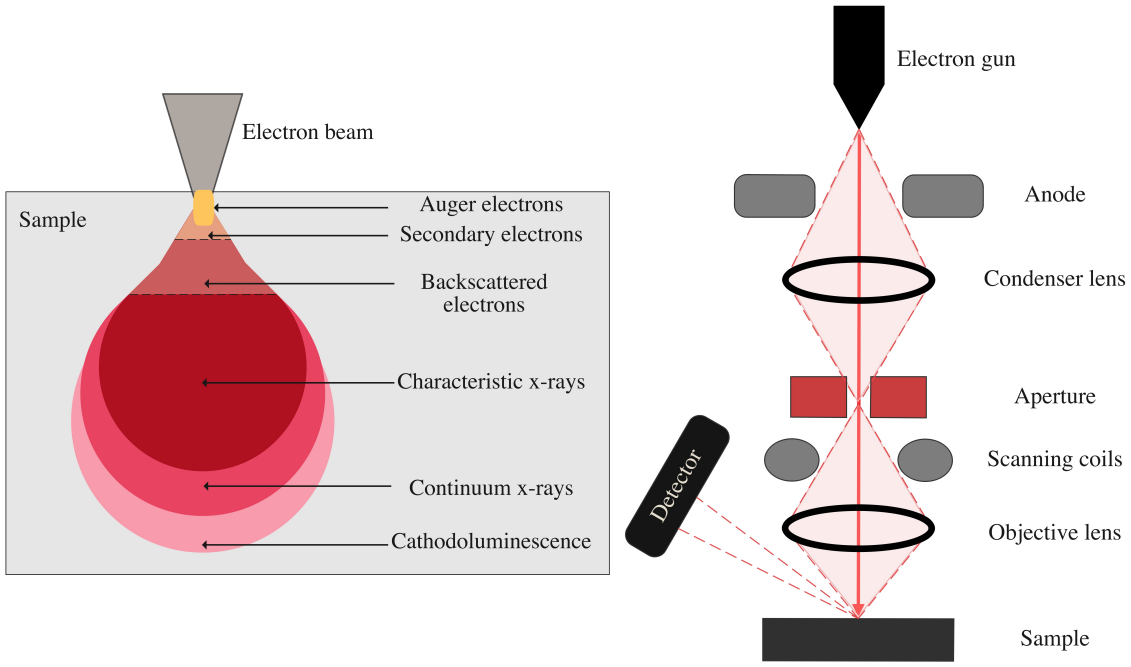

(a) (b)

Figure 3.3: Figure (a) illustrates the interaction volume and the different signals produced in a sample by the e-beam. Figure (b) schemtically illustrates the SEM microscope.

sample, the e-beam passes the objective lens to get focused into a small spot with the size of 4-10 nm on the sample surface. The scanning coils move the beam in x- and y-directions across the sample surface. The magnification of the SEM image is directly related to the length of the line scanned on the sample. The main focus of this thesis has been to investigate defect emission, which has been done with cathodoluminescence spectroscopy included in the SEM setup and explained below.

The SEM used in this work was a JEOL JSM IT300. Up to 200.000 magnification with 4-10 nm resolution may be obtained using a LaB_6 filament. The e-beam current is measured using a Keithley 6485 PicoAmperimenter, ranging from 10 pA to $\sim$ 1 μA. A Gatan Model 1905 Temperature Controller for the Gatan c1002 cold stage runs at 80 K to 473 K with a liquid N_2 cooling system for low-temperature measurements.

3.3 Cathodoluminescence spectroscopy

Cathodoluminescence (CL) and angle-resolved cathodoluminescence (ARCL) were used for the characterization of the defect emission in 4H-SiC. This section presents a basic overview of the characterization methods. As explained earlier, an electron can be excited from the valence band to the conduction band by an energy greater than the band gap energy. In a direct band gap material, the electron will typically quickly return to the ground state through an energy loss close to the energy of the band gap. In indirect band gap materials, described in section 2.1.2, the recombination happens with a change in crystal momentum, frequently through recombination at defects or traps within the band gap. In materials with a direct band gap, the luminescence

will mainly result from band-to-band recombination, while in indirect band gap materials a bigger portion of the luminescence results from recombination involving defect states. EHPs can recombine at defects either by interchanging charge carriers with the band edges or by internal excited-to-ground state energy transitions. The luminescence terminology distinguishes techniques based on the source of excitation. In cathodoluminescence, a focused e-beam is used as the excitation source, distinguishing it from e.g. photoluminescence, where photons are used as the excitation source.

Cathodoluminescence spectroscopy is a useful technique to characterize the optical response of materials, providing good spatial resolution. It is especially useful for identifying defects that have sharp and distinctive peaks in the emission spectra. CL systems are commonly integrated in electron microscopes, with the focused e-beam serving as the excitation source. The probability for excitation of an electron in the ground state increases as the energy of the secondary electrons decreases through scattering events. When the electron recombines to the ground state, light is emitted from the sample and collected by the parabolic mirror in Figure 3.4. The emission is then directed toward the spectrograph and detector, from which we extract the luminescence intensity as a function of wavelength, referred to as a spectrum.

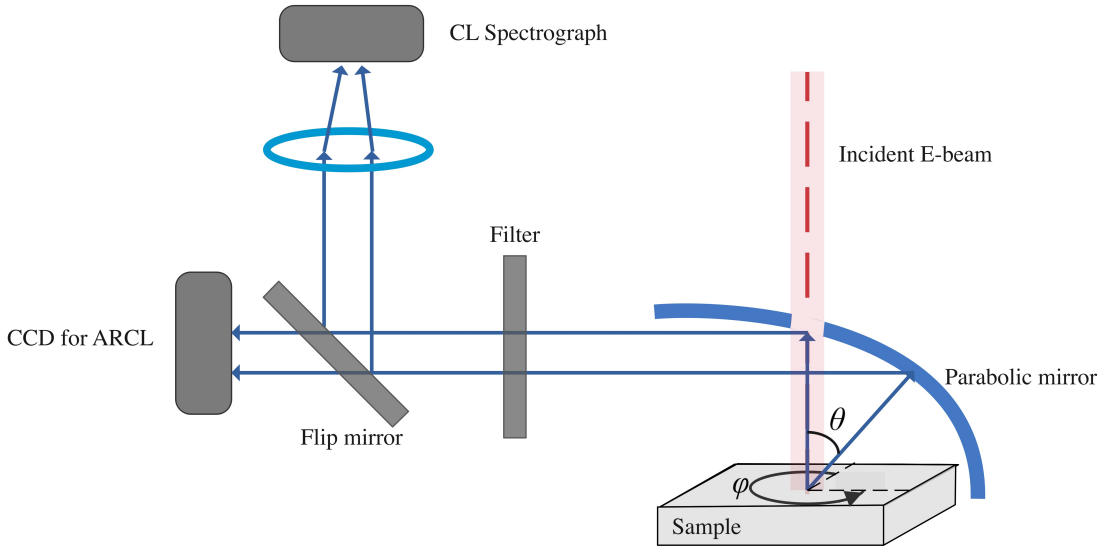

Figure 3.4: Illustration of the CL setup inside the SEM chamber. The flip mirror is engaged while performing spectral analysis. For ARCL measurements, the mirror is unengaged and the emission reaches the CCD screen. θ and ϕ are indicated relative to the sample.

In luminescence measurements, samples can emit photons over a broad spectral range. A filter may be included in the setup to selectively remove parts of the spectrum that are not of interest for a given measurement. Filters can e.g. be used to prevent saturation at the detector from signals outside the spectral region of interest or to check for certain spectrograph artifacts in the spectrum. For example, when looking at emissions from V_{Si}^{-} we use a 700 nm longpass filter to better see the emission peaks corresponding to the ZPL around 862 nm. Furthermore, the rate of radiative recombination to non-radiative recombination is typically higher at low temperatures. Thus CL measurements are more efficient at low temperatures, and liquid nitrogen is used to

cool the sample stage to 80 K [42].

A Delmic SPARC Cathodoluminescence System was utilized for the CL setup. An Andor Kymera 193i spectrograph with two motorized double grating turrets, Grating Turret 1: Mirror and 300 g/mm grating blazed at 500 nm were used for measurements in this project. A bandpass filter with a wavelength of 700 nm was used for spectrum filtration. An UV detector Andor Newton 940 CCD camera with 2048×512 array of back-illuminated (BU2) sensors was used and covers from 250 to 1100 nm wavelengths.

3.3.1 Angle Resolved cathodoluminescence

Angle-resolved cathodoluminescence (ARCL) is a technique used to collect information about the angular distribution of luminescence from a sample. From an ARCL measurement, we obtain luminescence intensity as a function of emission angle from the sample. The flip mirror in the illustration, Figure 3.4, is not engaged while performing ARCL so that the emission is sent from the parabolic mirror to the charge-coupled device (CCD) camera. Each pixel on the CCD corresponds to a unique point on the parabolic mirror and as a result, the CCD camera image can be directly converted to a radiation pattern for the hemisphere above the sample. The directions are described by an azimuthal angle ϕ from 0 to 2π and a zenithal angle, θ from 0 to π, the angles are indicated on the sample in Figure 3.4.

When an e-beam induces luminescence from a material, the outgoing radiation can be *coherent* and *incoherent*. Transition radiation can be generated when an electron passes through an interface between two media with different refractive indices. The interface transition polarizes electrons near the interface, resulting in an effective vertical dipole moment. Transition radiation emission profiles show high intensities for large angles of θ and low intensities normal to the surface [42]. The angular distribution of transition radiation is illustrated in Figure 3.6a. If the emitted radiation has a fixed phase with the E-field of the incoming electrons we call it coherent, this is the dominant process in metals. However, in semiconductors, incoherent radiation from spontaneous luminescence dominates [43]. Because incoherent emission is generally oriented randomly within the material, it is emitted roughly in a *Lambertian* emission distribution. Excitation of incoherent radiation can be very efficient because a single energetic electron in the incident e-beam can easily produce multiple photons through a cascade of excitation events. Incoherent luminescence is usually excited more efficiently by the cloud of slow secondary electrons rather than the primary beam. The number of secondary electrons participating in the signal generation is also much greater than the number of primary electrons. As a result, the signal is mainly obtained by secondary electrons and incoherent radiation from the same structure is frequently much stronger than coherent radiation [42].

With the refractive indices, n_1 and n_2, of the materials at both sides of the interface we can find the angle of incidence of the refracted incoherent emission relative to the surface normal, θ_2 from Snell's law

$$n_1 \sin\theta_1 = n_2 \sin\theta_2 \tag{3.1}$$

where θ_1 is the angle of the light at the other side of the interface, indicated in Figure 3.5. By

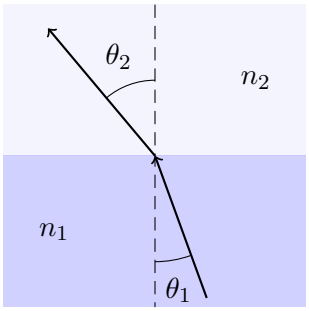

Figure 3.5: Refraction of light rays between two materials with refractive indices n_1 and n_2.

differentiating Snell's law with respect to θ_2, it can be shown that the radiance of incoherent emission has a Lambertian emission profile [44]. This means that the profile follows a cosine dependence of the angle of the refracted light, θ_2. The radiance will be highest for emission normal to the surface and decrease as the emission angle on the semiconductor-air interface increases [44]. This cosine-dependent emission profile will differ if the surface is not flat, for example, hemispherical surfaces will have a hemispherical angular radiation profile with emission intensity more spread out compared to a flat surface. The emission for surfaces with round shapes will thus be spread over a larger area. The radiation profiles for a flat semiconductor and a hemispherical surface, are shown in Figure 3.6b and 3.6c. The shape of the nanopillars will thus also influence the emission profiles.

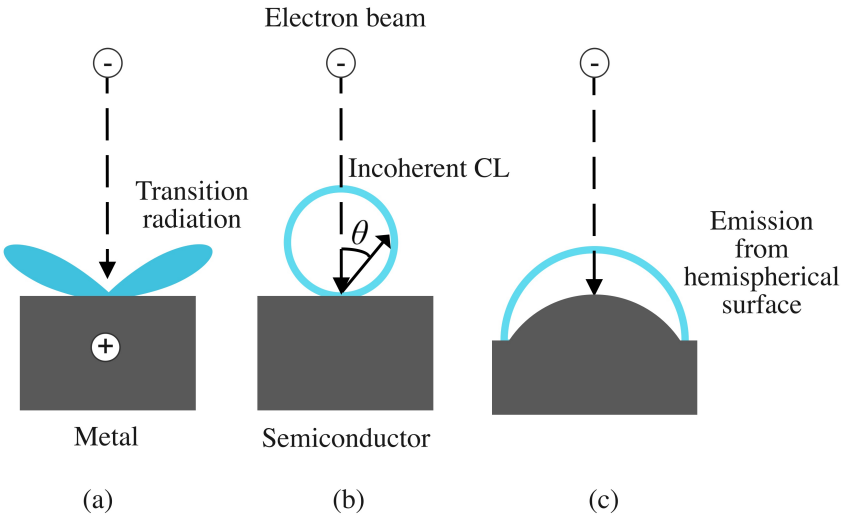

Figure 3.6: Transition radiation induced by an e-beam in (a) a metal, (b) shows the Lambertian emission profile for a flat semiconductor surface and (c) is the emission profile of incoherent emission from a hemispherical surface.

With ARCL we can extract a map of intensity as a function of ϕ and θ. Thus we obtain information about the angular distribution of the luminescence intensity. This complements standard spectral measurements, in which information about the angular distribution is not recorded. In particular, ARCL allows us to understand how nanostructures influence the angular distribution of the luminescence emitted by the sample.

3.4 Simulations of emission from single-photon sources in SiC Nanostructures

The FDTD method has been used for simulations of single-photon sources in SiC nanostructures. The use of numerical calculations of Maxwell's equations provides classical calculations of electromagnetism. When performing a simulation of quantum mechanical effects and structures in the size domain of the emitted wavelengths it is therefore important to keep in mind the classical nature of the modelling method. Nonetheless, we consider single dipoles embedded within nanopillars to be suitable approximations of single-photon emitting point defects. Simulation parameters such as boundary conditions, mesh and sources are described in this section. Before describing the method development for simulations of an ensemble of defects in nanostructures, field projections in FDTD are explained.

3.4.1 Simulation layout

The FDTD simulation consists of several different components, as illustrated in Figure 3.7a for a circular pillar on a substrate. The boundary condition used is called perfectly matched layers (PML) and is seen in orange in the figure. The region delimited by the PML is called the simulation region, everything inside this region will be included in the simulation. In the simulation region, the maximum simulation time, mesh settings and the properties of the PML are specified. The yellow lines represent monitors in the xy plane which are used to record simulation results, several monitors can be used during one simulation to collect fields from different areas.

The objects in the simulation, such as the pillar and the substrate (Figure 3.7a), are defined by data points containing the material's refractive index. The experimental material data points for the refractive index need to be adapted to a model which contains data for all wavelengths. This is done by Lumerical with a Multi-coefficient Material Model (MCM) between data points for experimental material data [39]. Figure 3.7b shows a plot of the real part of the permittivity for 4H-SiC over a wavelength span which corresponds to the bandwidth of the ZPL and PSB of V_{Si}. The model proposed by FDTD gives a good fit to the experimental material refractive index. The experimental material data for the refractive index of 4H-SiC was adapted from [34].

FDTD provides calculations with one wavelength at a time. Results with several wavelengths are possible, but the simulations are time-consuming and simulations with one wavelength are chosen as sufficient for this project. The refractive indices in the wavelength span plotted below also shows small differences between $\lambda = 860$ nm and $\lambda = 960$ nm. This indicates that differences between the behavior of waves within this wavelength span will be very similar so it is sufficient to perform simulations with one central wavelength at 895 nm for an ensemble of defects. However, for simulations of structures in the size domain of the wavelength, simulations with a wavelength equal to V1s ZPL at 862 nm have been done. Due to the principles of TIR discussed in section 2.4, the refractive index will have a greater impact on the EM fields for bigger structures than for structures in the size domain of the emitted wavelength.

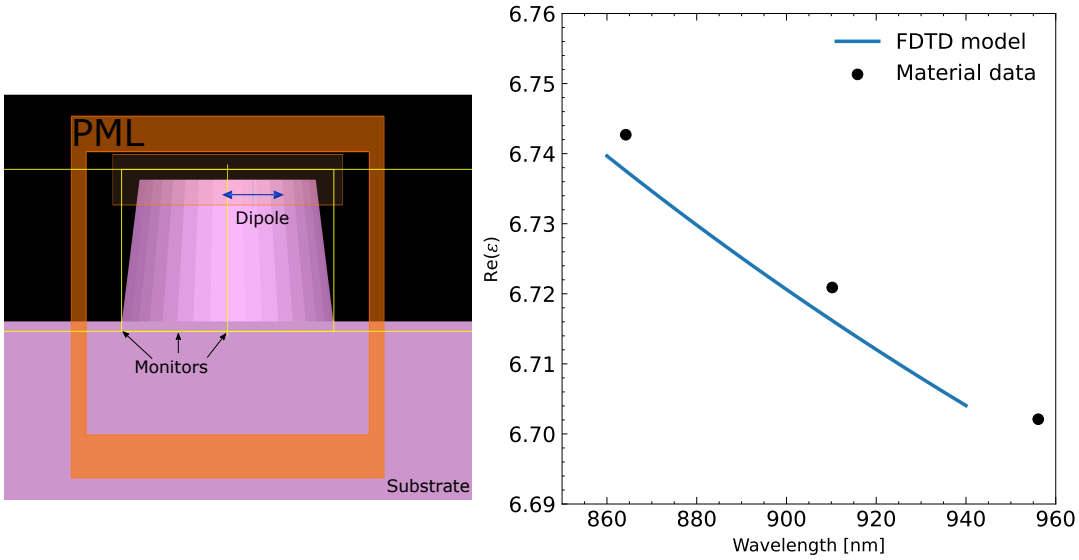

(a) (b)

Figure 3.7: Panel (a) shows the simulation setup, (b) shows the FDTD material model fit to the experimental refractive index adapted from [34]

3.4.2 Open Boundary Conditions

Since the FDTD algorithm relies on neighboring Yee cell data, it is important to pay attention to the edge of the simulation region. In this thesis, we consider a system where radiation eventually propagates out of the system. Absorbing boundary conditions, also known as perfectly matched layer (PML) boundary conditions, are utilized to describe such an open system and are commonly used in FDTD. To minimize reflections and absorb outgoing waves, PML boundaries are implemented as an absorbing dielectric material [39]. The PML boundaries that are used herein were proposed by Bérenger in 1994 [45].

The boundaries are "perfectly matched" because to suppress reflection at the boundaries the impedance of the interior simulation domain and the PML is matched. The impedance for the interior domain is given by

$$\eta = \sqrt{\frac{\mu}{\epsilon}}, \tag{3.2}$$

where μ is the magnetic permeability and ϵ is the electric permittivity. The impedance of the interior and the impedance of the PML, η_{PML} must thus be equal. So that

$$\eta_{\text{PML}} = \eta \quad \rightarrow \quad \frac{\mu_{\text{PML}}}{\epsilon_{\text{PML}}} = \frac{\mu}{\epsilon}. \tag{3.3}$$

For finite structures, $\mu = 1$ and $\epsilon = \epsilon_r$ since the structure is surrounded by air [46][47]. A need for multiple layers arose from a limitation of PML to reflect an exact continuous wave. Since FDTD implements a discretized version of a wave, small numerical reflections do exist. The structure must extend through the PML since the electromagnetic fields are calculated both within the simulation area and within the PML. Therefore it can be seen that the substrate in Figure 3.7a extends completely through the PML. The fields inside the PML are propagating

and it is important that the material properties also are defined here.

The PML has a finite size which is determined by the number of layers specified for the boundary. The absorption at the boundary increases as the number of layers increases. Reflection from the PML is a possible source of error in a FDTD simulation. There will always be small reflections from the PML, these reflections may re-interfere with the source or simply re-interfere with the scattered fields. The reflection from the PML can be reduced with an increasing number of PML layers [39]. The number of PML layers has been convergence tested and the test results are presented in the last part of this chapter.

3.4.3 Meshing - step size

The mesh used by FDTD is as illustrated by the Yee cell in Figure 2.10, rectangular and Cartesian in style. It is critical to understand that each mesh point is used to calculate important simulation variables, including material characteristics and geometrical information, and electric and magnetic fields. On a finite grid, solving Maxwell's equations offers two fundamental challenges. On one hand, we will have numerical mistakes related to the limited mesh size even in homogeneous materials. On the other hand, the simulation of a wave's propagation will be affected by dx, dy, dz, and dt, and so it will not be the same on a finite mesh as it is in actual space. Using a smaller mesh will decrease the errors from these challenges and result in a more accurate representation of the structures. However, it comes at a cost in terms of memory needs and simulation time. In the FDTD method, the simulation time scales as $\frac{1}{dx^4}$ for 3D simulations.

One of the features of the FDTD solver is the conformal mesh approach, which allows for accurate results even when using a coarse mesh. Since FDTD uses a Cartesian coordinate system, curved objects are not easily modeled and can lead to artifacts such as staircase interfaces, since the curved surface permittivity appears like a staircase. Lumerical, therefore, uses conformal mesh technology along curved dielectric interfaces to provide sub-cell accuracy to electromagnetic fields. In general, this method accounts for sub-cell features by using an integrated solution of Maxwell's equations near the interface of an object. The method utilizes the electric field component along the edges of a cell, rather than using its area and volume which are partially filled with the object's material [48]. A conformal mesh provides greater accuracy for a given mesh size and makes it possible to run simulations much faster without sacrificing accuracy. The conformal mesh adjusts the mesh size to the material's refractive index. The wavelengths in materials with greater refractive indices will be shorter, necessitating a smaller mesh size.

If more than two materials are found in the same cell, the method reverts to staircasing for that cell, which involves evaluating the material at each position of the Yee cell. It is thus not possible to account for structure variations that occur within a single Yee cell. The staircasing can be reduced by applying an inner finer override mesh at the edges of the structure where we are interested in the outgoing emission [39]. The mesh override region, shown in faded orange on top of the pillar in Figure 3.7a, is used to specify a finer mesh in regions where a higher resolution is needed. In this case, it is used on the top of the structure because the angle is steeper here and it is also the region where the emission from defects is obtained. The step size of the conformal

mesh and the mesh override region have been tested for convergence.

3.4.4 The source

There are several different sources to choose from in Lumerical but the most relevant source for this project is an electric dipole source. A dipole radiation pattern is emitted by the dipole. The electric dipole is a point source equivalent to an oscillating point charge which will give the representation of luminescence from an excited defect. Different properties can be set for the source, such as the orientation, the wavelength and the position.

The simulation software provides total control over the source's time signal, and can therefore introduce an impulse with a very large bandwidth, or a continuous-wave signal with only a single wavelength component. The dipole is placed 150 nm below the surface of the pillar which complies with the projected range of the ions used for defect formation in the physical nanopillars. It should be kept in mind that an electric dipole is a classical object used to model luminescence from a point defect. Thus "photons" emitted from the dipole are viewed as waves by FDTD, and the quantum principle related to wave-particle duality is not taken into account.

3.4.5 Field projections in FDTD

FDTD performs calculations of the near-field, which is essentially the field within the FDTD grid. However, the field of interest is often the field further away from the simulation region called the *far-field*. The near-field obtained from FDTD can be used to obtain the far-field by a near-to-far-field transformation based on a Fourier transform. As long as the EM fields are known anywhere on a plane or closed surface the far-field can be calculated [39].

The built-in function in the Lumerical software, *farfield3d*, was used for the far-field calculation. The standard three-dimensional (3D) far-field was calculated on a hemispherical surface 1 meter from the simulation. Since the far-field data is 3D it has to be flattened and the default in FDTD is that the data is plotted as if we look straight down on this hemisphere. The field is plotted as a function of direction unit vectors u_x and u_y, which both range from -1 to 1. Thus the point (u_x, u_y) = (0,0) corresponds to the middle of the hemisphere where the EM field is a result of wave propagation with normal incidence [39] Figure 3.8 shows the far-field of a pillar with r = 2.4 μm obtained from a simulation with one dipole.

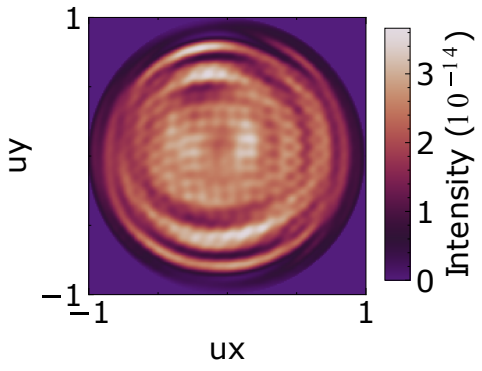

Figure 3.8: Far-field of emission from a single dipole at distance of 1 m from simulation region.

The same polar coordinates are used as the ones related to ARCL, referring to the azimuthal angle $\phi \in [0, 2\pi]$ and the zenithal angle $\theta \in [0, \pi]$. The hemisphere where the far-field is collected, with an indication of θ and ϕ is shown in Figure 3.9. The coordinate transformation between spherical and cartesian coordinates are:

$$u_x = \sin\theta\cos\phi, \quad u_y = \sin\theta\sin\phi, \quad u_z = \cos\theta, \tag{3.4}$$

$$u_z = \sqrt{1 - u_x^2 - u_y^2}, \quad u_x^2 + u_y^2 + u_z^2 = 1. \tag{3.5}$$

Polar plots of the radiation profile can be formed by the built-in *farfieldspherical* function in Lumerical. This function interpolates the far-field data from u_x and u_y coordinates to spherical coordinates. This makes it possible to extract a cross-section of the hemisphere and obtain a representation of how the emission is spread out as a function of the zenithal angle, θ.

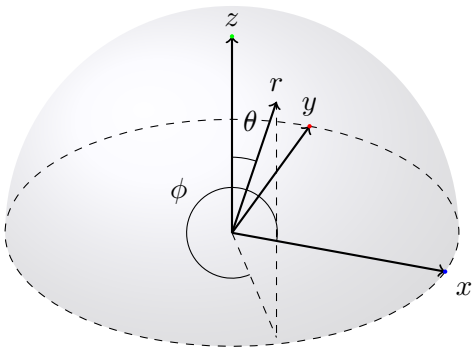

Figure 3.9: Hemisphere with an indication of the azimuthal angle ϕ ranging from 0 to 2π and the zenithal angle θ ranging from 0 to π

Lumerical provides a different function *farfieldexact3d* which projects complete complex vector fields to specific locations. This function can be used for calculations of the so-called intermediate field, which is beyond the simulation region but not yet the far-field. The field calculated with this approach are also angle-resolved from a 3D hemisphere and plotted in 2D as explained above for the far-field.

The signal collected on the parabolic mirror during ARCL measurements is obtained from a large area and a far-field projection at a distance of 1 m could be sufficient for comparison with ARCL. The development of the simulations in this project is presented in the following section and the development focuses on the far-field emission.

3.5 Method Development of FDTD Simulations

A major part of the work presented in this thesis was to develop a framework based on FDTD to simulate wave propagation in structures relevant for point defect based QT, including nanostructures, to support the experimental results from CL and ARCL. This section explains the development of the simulations concerning the far-field intensity for modeling the emission from an ensemble of defects in SiC nanostructures.

A Lambertian shape of the emission through a flat surface was confirmed by performing a simulation with a dipole in the substrate. The far-field intensity image obtained from this simulation is shown in Figure 3.10b and is acquired with the *farfield3d* function in Lumerical, explained in Section 3.4.5. Figure 3.10a shows a polar plot extracted from the $\phi = 0°$ cross-section of the image in Fig. 3.10b. The polar plot is obtained by using Lumerical's *farfieldspherical*-function, which extracts a cross-section of the far-field for a specified ϕ value. A script showing the acquisition of the polar radiation profile can be found in Appendix B.2. The plot describes the intensity as a function of θ and gives information about how the emission is spread out on the 3D hemisphere above the simulation region. The θ=0° point in the polar radiation profile (Fig. 3.10a) corresponds to the center of the far-field image (Fig. 3.10b). High intensities for θ=0° indicates a large portion of the emission being normally directed from the structure, while intensities at higher values of θ indicate outward-directed emission.

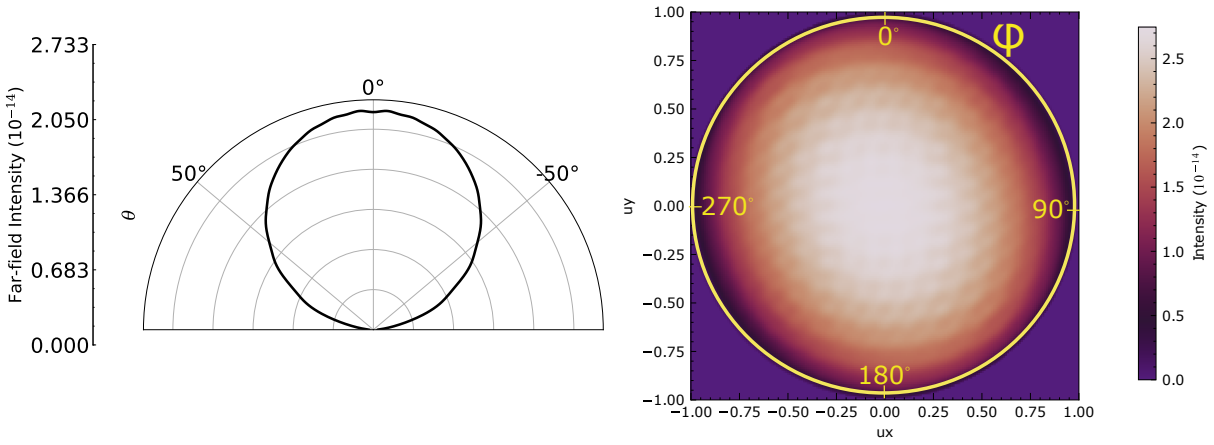

(a) (b)

Figure 3.10: Far-field emission from a dipole source under a flat surface. Figure (a) is the polar emission profile extracted from the cross-section where $\phi = 0°$ in (b).

3.5.1 Geometries of physical nanopillars

Figure 3.11 shows the geometry of the pillars and how the different properties are defined on the nanopillars when setting them up in the FDTD simulation. Table 3.1 lists the experimental pillar bottom radii with corresponding values for$_{\text{top}}$ radii and the angle α. The dimensions have been chosen based on available SiC structures that were measured using a ruler application in the SEM software. As α decreases and r_{top} approaches r_{bottom}, the more straight are the sidewalls of the pillars. These measures were used to make the same structures in Lumerical. All of the pillars have a height of 1.4 μm. When developing the method for the simulations of the nanostructures, the smallest pillar was used as a starting point.

The goal of the FDTD simulations was to get simulation results that corresponded to experimental results and then use simulations to explore the influence of different geometries and emitter positions. The experimental pillars are technically too big for the term "nano". Due to practical limitations, structures at the nano scale are not available yet. The developed simulation

method will also be used as a tool to explore structures with nano-dimensions. The experimental ARCL measurements are discussed more in detail in Chapter 5.

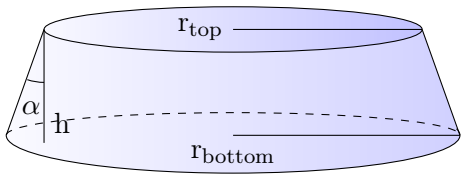

Figure 3.11: Schematic illustration of a nanopillar with an indication of the different variables.

Table 3.1: Measures for the different experimental nanopillars

Structure	r_{bottom} (μm)	r_{top} (μm)	h (μm)	α
I	1.4	0.60	1.4	30°
II	1.9	1.25	1.4	25°
III	2.4	1.8	1.4	23°
IV	2.9	2.5	1.4	16°

3.5.2 Simulation of radiation from an ensemble of defects in SiC

The ion-implanted structures used for experimental measurements in this thesis have an ensemble of defects spread over a given volume. Each defect is independent of its neighbors and emits radiation with a random phase that varies on a time scale. This type of emission is called spatial incoherence. Figure 3.12 shows the far-field emission from a simulation performed with one dipole in the pillar. The dipole orientation is indicated as the green arrow in Figure 3.12b. The orientation of the dipole is the reason for the field being stronger at the top and bottom of the image. Simulations of an ensemble of defects required implementations of additional dipole sources.

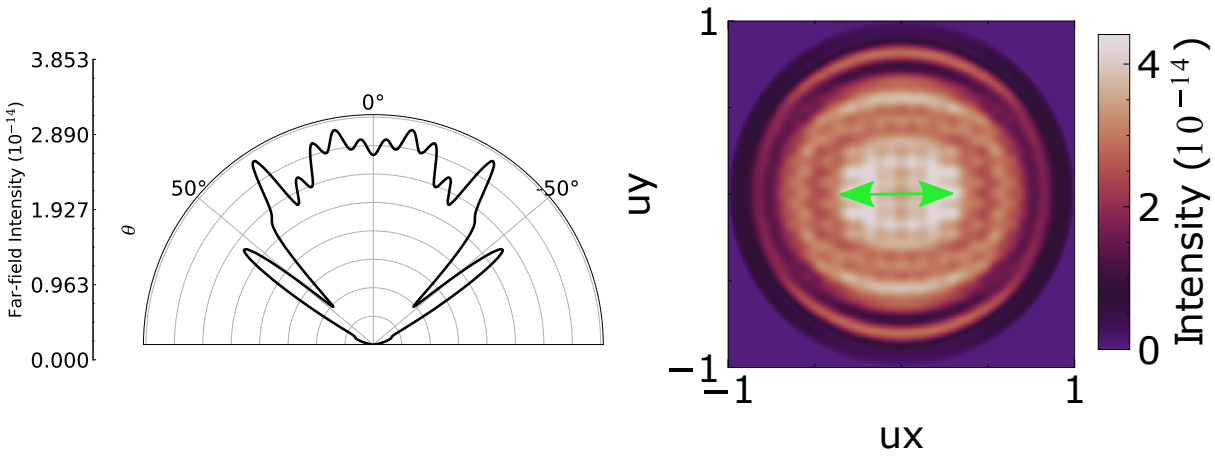

(a) (b)

Figure 3.12: Emission intensity from one dipole in a pillar with $r_{bottom} = 1.4$ μm. (a) Emission profile extracted from the $\phi = 0$ cross-section. (b) Far-field intensity image, the green arrow illustrates the dipole orientation, which corresponds to $\phi = 0°$.

FDTD is fundamentally a coherent simulation method when several dipoles are used in one

simulation. Direct simulations of incoherent emission are complex and time-consuming. One possible way is to use averaging over an ensemble of dipoles in each simulation. However, this is also time-consuming as it requires a large number of simulations. Instead, the simulation can be carried out by running one simulation for each dipole individually and then adding the coherent results incoherently. This approach has no statistical error, and the total number of simulations required to do this is typically less than what is necessary for ensemble averaging [39]. For example, the electric field of three dipoles is given by three independent simulations and then summed:

$$|E|^2 = \frac{|E_1|^2 + |E_2|^2 + |E_3|^2}{3}. \tag{3.6}$$

Figure 3.13 shows the difference in the radial emission profiles for coherent emission with two dipoles in the same simulation (Fig. 3.13a), and incoherent emission with the sum of results from two independent simulations (Fig. 3.13b). Both results are obtained with the dipoles in (x,y) positions (0,0) and (0.4,0).

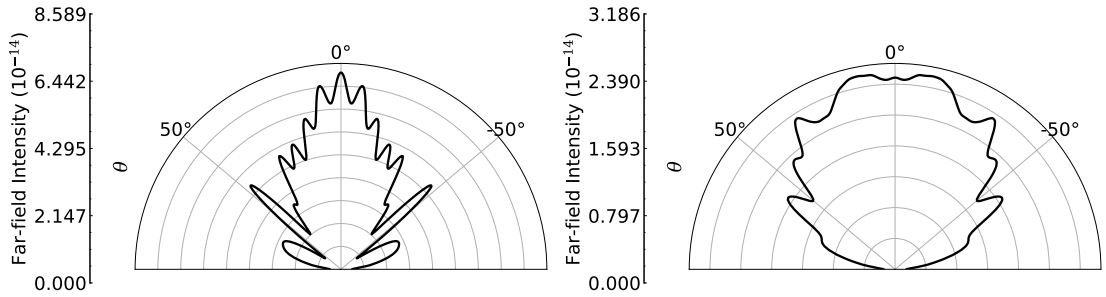

(a) (b)

Figure 3.13: Polar emission profiles from (a) two dipoles in the same simulation and (b) sum of emission from two dipoles in independent simulations. Both radiation profiles are extracted from the $\phi = 0$ cross-section.

The dipoles are positioned in the pillar using a random number generated between 0 and 1. This gives random dipole positions spread out in the xy-plane. To obtain comparable results from pillars of different dimensions, the same seed of random numbers is used for every structure. The script used for the positioning of the dipoles can be found in Appendix B.1. The x and y positions of the dipole were calculated with the following approach:

$$r = r_{\text{pillar}}\sqrt{n}, \quad \theta = n2\pi \tag{3.7}$$

$$x = r\cos(\theta), \quad y = r\sin(\theta) \tag{3.8}$$

A convergence test was conducted on the number of dipoles concerning the shape of the emission profiles to determine how many dipoles were sufficient for the simulations. First, all dipoles were arranged inside a small area in the middle of the structure. The radiation profiles in Figure 3.14 show that the number of dipoles has little to no influence on the shape of the emission profile.

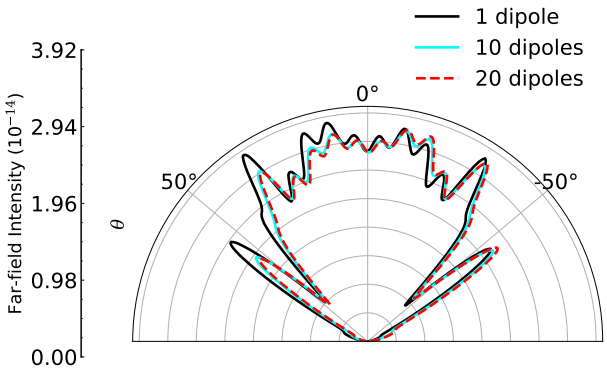

Figure 3.14: Far-field radiation profile as a function of θ for a pillar with r_{bottom} = 1.4 μm. All dipoles were placed inside a small area in the middle of the pillar. The emission profiles are extracted from ϕ=0°.

Next, we did a simulation where the dipoles were placed randomly around a larger area. The changes in the emission profiles with this approach are larger, and the emission intensities for larger angles of θ are increased in comparison to when all dipoles were placed in the middle. When performing the ARCL measurements the e-beam is placed at one point, but due to scattering events, we expect to detect emission from a larger area around this point. The experimental emission profiles we obtained from ARCL showed higher intensities on the sides, meaning higher angles of θ. Figure 3.15a shows the emission profile from this simulation, it can be seen that the shape of 10, 20 and 30 dipoles is similar and thus 10 dipoles in the r=1.4 μm pillar were chosen as sufficient for simulations of an ensemble of defects. However, the emission profiles are not symmetric due to the random position of the dipoles. A different randomized placing will give a slightly different emission profile. The intensity image obtained from simulations with dipoles placed over a larger area, Figure 3.15b, shows a more spread-out intensity compared to the image from dipoles in the center. For the other pillar sizes, the number of dipoles is scaled to the area of the structure so that the density of dipoles is the same when comparing the structures.

3.5.3 Influence of the dipole's orientation

The source settings in Lumerical's FDTD can change the orientation of the dipole source. The orientations are given by the angles θ and ϕ, where θ sets the orientation relative to the z-axis and ϕ determines the orientation in the plane. The silicon vacancies in an ideal SiC crystal are all aligned with the same dipole orientation, along the crystal c-axis [33]. An oscillating dipole will emit light normal to its oscillating direction, θ was therefore set to 90°, so the dipole is oscillating in the xy-plane.

Since the radial emission profiles are extracted from the intensity image at a specific ϕ value, the orientation of the dipole will influence the radial emission profiles. The intensity images will, on the other hand, get influenced by the ϕ orientation of the dipole. The ϕ orientation of the dipole was randomized during simulations with several dipoles to see how this influenced the

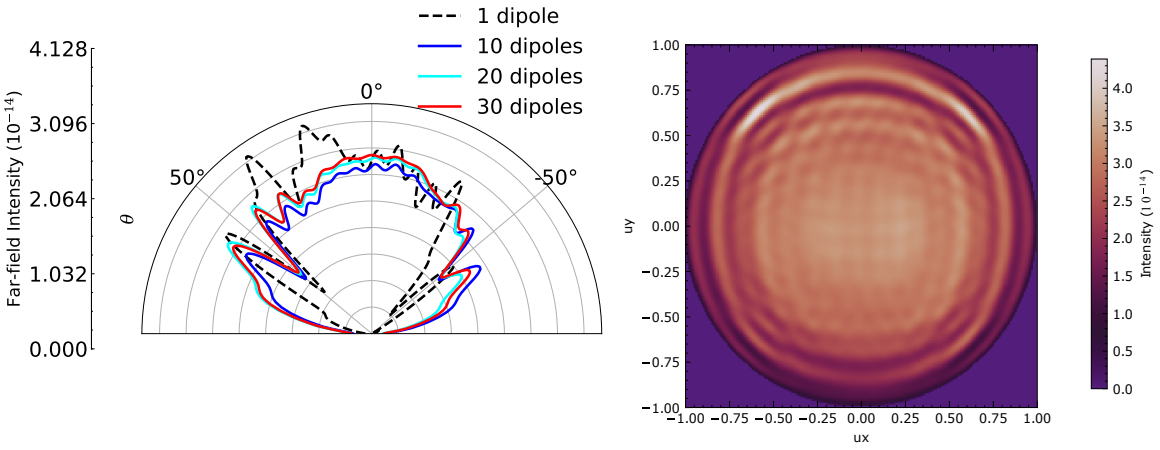

(a) (b)

Figure 3.15: a)Radial emission profiles from the ϕ=0° cross-section for the different numbers of dipoles in a pillar with r=1.4 μm. The dipoles are positioned randomly in the xy plane. (b) is a far-field emission image from simulation with 20 dipoles.

emission profiles, the results from these simulations are shown in Figure 3.16. The simulations showed that more dipoles are required for convergence of the emission profile with a randomized ϕ orientation of the dipole. As an approximation, we assume that the defects in SiC have the same orientation because they are in a crystalline material and a ϕ=0 orientation was used for all dipoles.

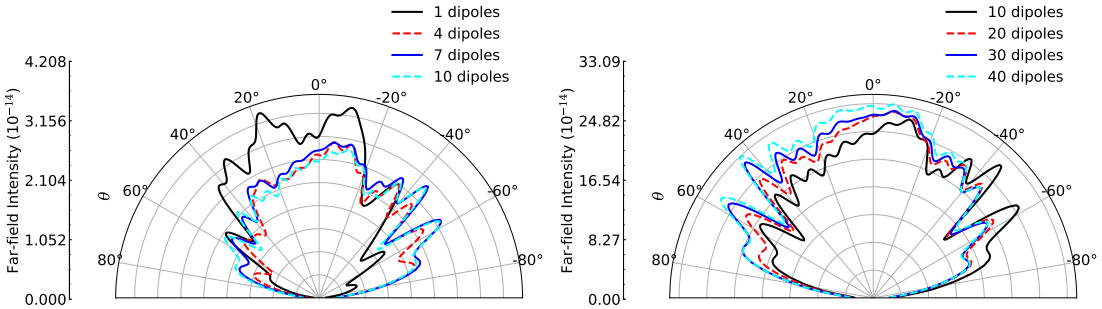

(a) (b)

Figure 3.16: Polar emission profiles from the ϕ=0° cross-section obtained from simulations done on a pillar with r_{bottom} = 1.4 μm. The dipoles have random positions as well as a random ϕ orientation in the plane.

The result from two simulations performed with respectively $\phi = 0$ and random ϕ values are compared in Figure 3.17. The emission profiles are obtained by plotting the average polar emission profiles for all ϕ values, and the plot shows that both approaches give a similar shape to the emission profile. The shape of the emission profile is roughly the same for the different dipole configurations, except for small differences at $\theta = 0$. Since the simulations are time-consuming, 10 dipoles have been chosen, all with the same ϕ=0 orientation, for simulations of an ensemble of defects in SiC nanostructures with r_{bottom} = 1.4 μm.

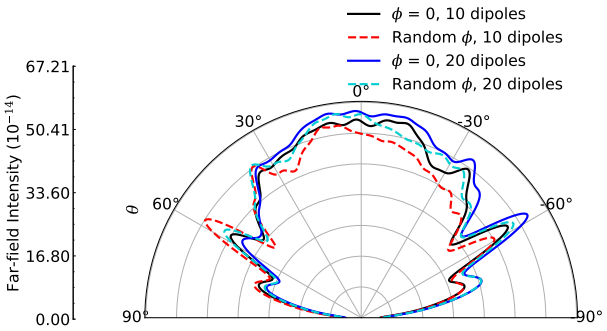

Figure 3.17: Comparison of polar emission profiles plotted as an average for the $\phi \in [0, 90°]$ cross-section. One simulation was done with random orientation of the dipoles in the plane and one with all dipoles in the same orientation. The simulation was conducted on a pillar with $r_{bottom} = 1.4$ and $r_{top} = 0.6$ μm

SiC substrate grown 4° off main crystal axis.

The substrate used in the experimental part is grown 4 ° off the crystal *c*-axis. The nanopillars have however a straight orientation without any offset because they are fabricated with directional ion etching [12]. Therefore the defects which contribute to the luminescence will have a direction of 4° from the main crystal axis. To investigate how this offset influenced the simulations a dipole with θ=94° were placed in the pillar with $r_{bottom} = 1.4$ μm. The emission profile from a simulation with a 4° offset is compared to the one with an 0° offset in Figure 3.18. There is an insignificant difference between the two and therefore the simulations for the rest of this project were done with a 0° offset of the dipole.

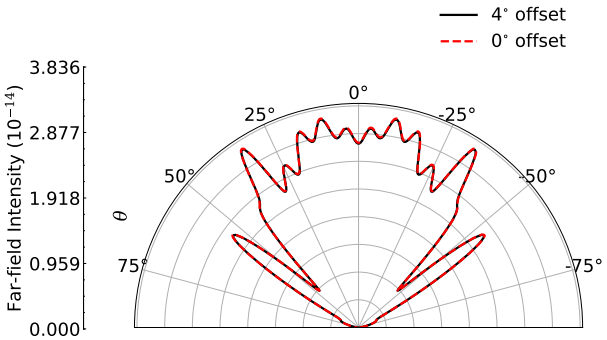

Figure 3.18: Emission profiles from the ϕ=0° cross-section for one dipole with 4° and 0° offset from the main crystal axis in a pillar with $r_{bottom} = 1.4$ μm and $r_{top} = 0.6$ μm.

3.5.4 Simulations of nanostructures from the literature

The simulations of SiC nanostructures were initially inspired by Ref. [29]. The researchers behind this paper showed an increased light collection when placing V_{Si} into a nanopillar. A

simulation with similar structures as in this paper was conducted for a pillar with $r_{bottom} = 0.3$ μm, $r_{top} = 0.24$ μm and h = 0.9 μm. The x and y components of the far-field are shown in Figure 3.19. The results acquired from these simulations are qualitatively similar to the results presented in [29].

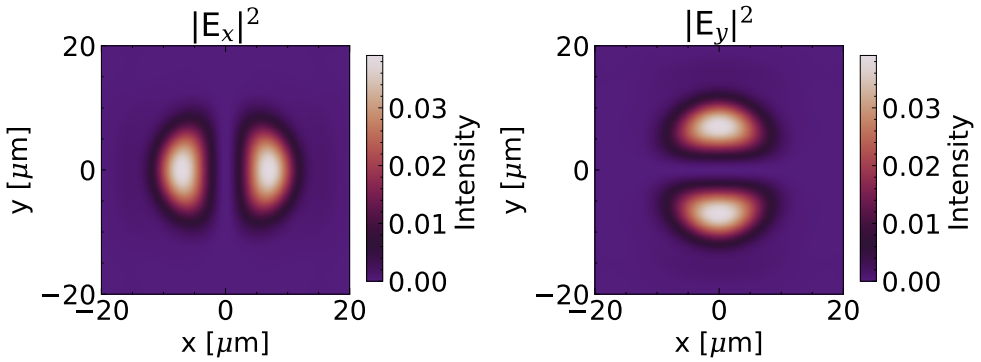

(a) (b)

Figure 3.19: Far-field emission profiles for the (a) x- and (b) y-component of the electric field.

3.6 Convergence tests and sources of error

When using numerical calculations, there will always be some numerical errors. It is crucial to understand the sources of these errors. Since a reduction of errors often leads to increased simulation time and memory requirements, we need to consider what is necessary for our application [39]. Sources of errors might come from several of the simulation objects, mainly from the PML and the mesh size, which therfore need to be convergence tested.

Quantifying the level of convergence

Generally, it is challenging to know the correct answer when performing a convergence test. There are different approaches to the determination of the error. In this project, we look at the difference between two convergence steps, given by

$$\Delta\sigma(i) = \sqrt{\frac{(\sigma_i - \sigma_{i-1})^2}{\sigma_i^2}}, \tag{3.9}$$

where σ_i and σ_{i-1} is a simulation result, for example, transmission, from one convergence step i and the previous step i - 1. $\Delta\sigma$ should approach zero but may reach some constant value as other parameters may dominate the errors. However, the sources of error in an FDTD simulation will never be eliminated, and one must decide what level of error is acceptable for the purpose. When comparing simulation results to experimental results from cathodoluminescence, the error of the simulation should be at the same level as the uncertainty from the CL experiments which have a resolution of a few nanometers in optimized conditions.

3.6.1 Mesh

As explained in Section 3.4.3, Lumerical uses a graded mesh. There are primarily two sources of error related to graded meshing. As a result of changes in the grid size, small scatterings of the field can occur and cause small gains or losses. Mesh grading may affect PML performance and lead to more reflection from the PML. A decrease in grid size will increase the simulation time, so the size of the simulation mesh and the grid size of the mesh override region have been convergence tested for transmission. As seen in Figure 3.20a, ΔT approaches zero at a mesh accuracy of 3, which we found was sufficient for further simulations. The grid size of the override mesh region has also been convergence tested for transmission, and as seen in Figure 3.20b, the level of error decrease as the size of the inner mesh decrease. A 20 nm mesh size gives the best result from the convergence test. Because this project required running many simulations the inner mesh size was set to 40 nm, with the error only reduced to ~ 0.05 for transmission.

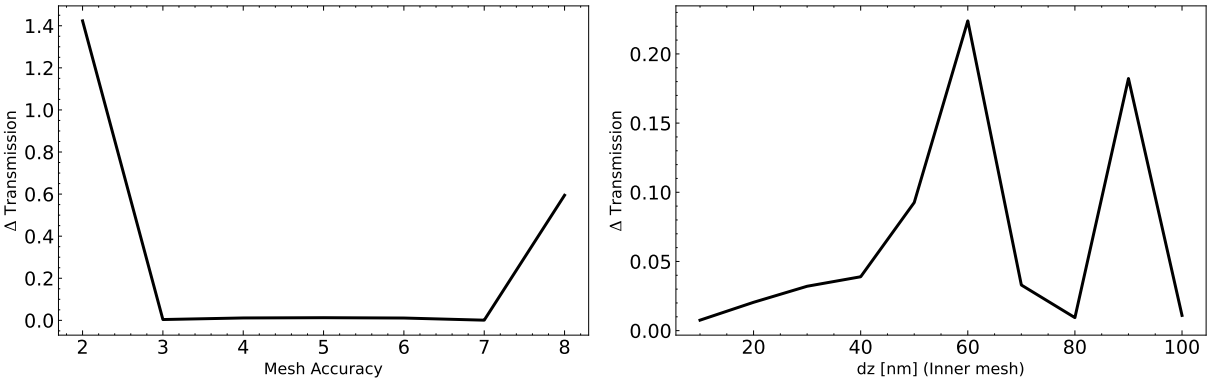

(a) (b)

Figure 3.20: Panel (a) shows the convergence of mesh accuracy in the simulation region with respect to transmission, and (b) shows the convergence of the override mesh region with respect to transmission. Both tests were conducted on a straight angled pillar with r = 2μm

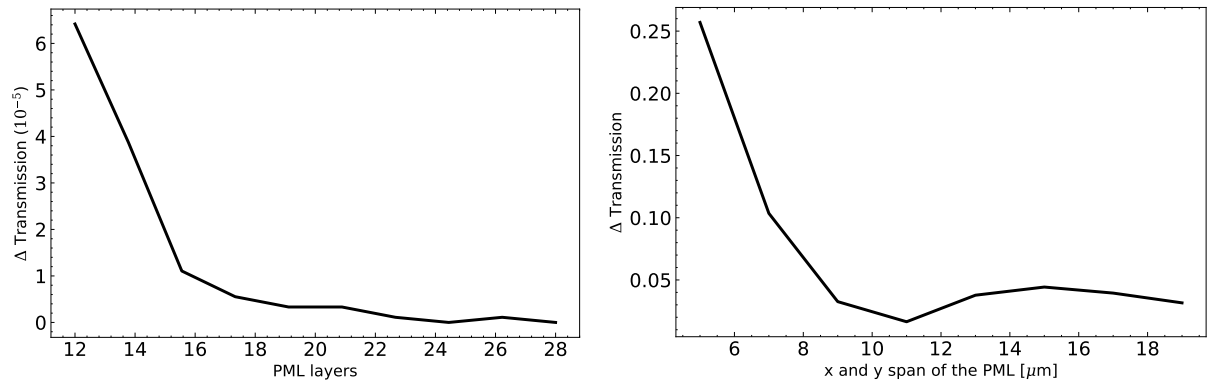

(a) (b)

Figure 3.21: (a) Convergence of number of PML layers. (b) is the convergence of the x and y span of the simulation region with respect to transmission. Both tests were conducted on a pillar with r_{bottom} = 1.5 μm and r_{top} = 1.25 μm.

3.6.2 Boundary conditions

The primary source of error resulting from the PML is reflection. Any reflection from the PML might re-interfere with the dipole source and result in inaccurate power normalization. As the number of PML layers increases, the reflection will decrease. The PML region must therefore be large enough to ensure that all of the radiation hits the monitor over the pillar before going through the PML. Both the size of the PML and the number of layers have been tested for convergence of transmission. The convergence results are shown in Figure 3.21. The number of PML layers influences the simulation time and has been convergence tested to find the optimal number for the simulations. The results show that the difference in transmission with the number of layers is small, $\Delta T \sim 10^{-5}$. When we approach 18 layers ΔT goes towards zero, and 18 layers are chosen as sufficient for the simulations.

The convergence tests of the size of the PML are analyzed for transmission and in addition for the shape of the polar emission profile for one dipole. Figure 3.22a shows how the far-field intensity at $\theta = 0$ varies as the size of the simulation region increase. When the size of the simulation region increases, the polar emission profiles, shown in Figure 3.22b, increase in intensity for angles of θ near -80° and 80°, we expected to see this in the experimental polar emission profiles, and a larger PML size is therefore needed. This is also something that one could expect to get from the experimental polar emission profiles, and thus a larger PML size is required. The size of the simulation region was set to 15 µm for a pillar with a radius of 1.4 μm. This corresponds to 6 μm on each side of the structure and was employed in the remaining simulations. The convergence test was done with the dipole placed off-center, thus the radial emission profiles obtained from the convergence test are not symmetric. The same dipole position was used for each PML size.

The z-span of the simulation region was also varied. This convergence test showed that the size above the pillar had no impact on the transmission collected at the monitor. However, the electric fields in the simulation are affected by how deep the PML expands into the substrate. The FDTD software checks the fields for convergence and stops the simulation when they reach some finite value. The PML was extended 1.25 μm down through the substrate to avoid divergence of the simulations.

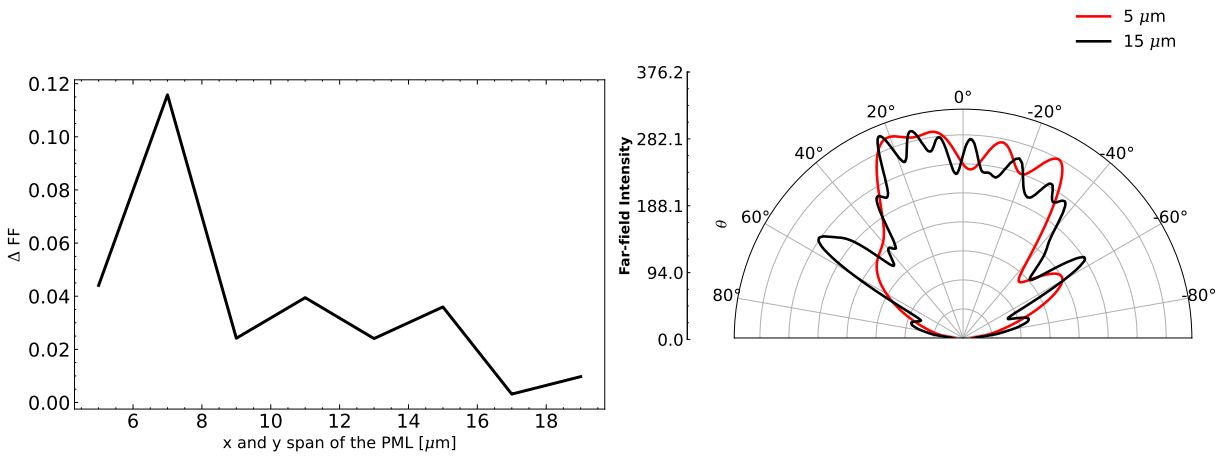

(a) (b)

Figure 3.22: (a) shows far-field intensity at $\theta = 0$ with respect to the size of the simulation region. (b) shows polar emission profiles of two simulations with xy-span = 5 μm and 15 μm. The test was conducted on a pillar with $r_{bottom} = 1.5$ μm and $r_{top} = 1.25$ μm.

Chapter 4

Results and discussion

This chapter focuses on the spectrum and angle-resolved cathodoluminescence characterization of a SiC sample with nanostructures and their characteristics. The silicon vacancy was identified, and the CL parameters were optimized to maximize the detection of the silicon vacancy's intensity. The emission from V_{Si} is investigated concerning the size of the nanostructures as well as compared to emission from the substrate. Emission profiles from nanostructures of different sizes are compared. An important aim of the present work was to develop a simulation model which could be compared to experimental results, in particular the ARCL results. The results from CL and ARCL are therefore compared to respectively the near and far-field obtained from FDTD simulation results. The electromagnetic fields are simulated with the FDTD method and are used to explore the influence of emitter position in nanopillars as well as structures in a size domain that are not practically possible to make in the lab.

The nanopillars measured with CL were introduced in section 3.1.3. The bottom (r) and top radius (r_{top}) measured from SEM images of the pillars are presented in Table 4.1. A SEM image of a pillar with r = 1.9 μm is shown in Figure 4.1a. The image shows that the surface roughness of different pillars varied. The smallest pillars, with r = 1.4 μm, have the steepest sidewalls, and as the pillar size increases the angles sidewalls become more straight. All pillars are from the same sample which was implanted with 21 keV He ions to a fluence of 1×10^{11} cm^{-2}. It's also worth noting that the fluence is large, therefore single defect emission is unlikely, and this study focuses on the emission from an ensemble of defects. Figure 4.1b displays a schematic illustration of a pillar where the location of V_{Si} is displayed as the light blue region in the upper part of the pillar. The silicon vacancies generated with ion implantation are from the SRIM simulations in section 3.1.3 expected to be found in a Gaussian distribution from the surface and until a depth of 200 nm, with a peak at 150 nm.

Table 4.1: Radius measurement of the different experimental nanopillars

Structure	r (μm)	r_{top} (μm)
I	1.4	0.60
II	1.9	1.25
III	2.4	1.8
IV	2.9	2.5

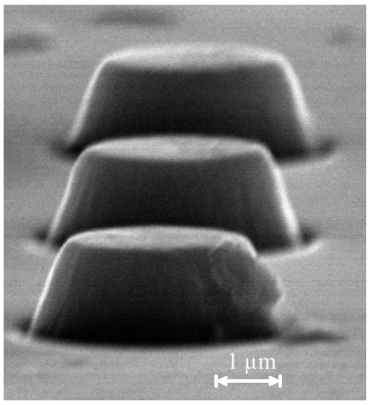

(a)

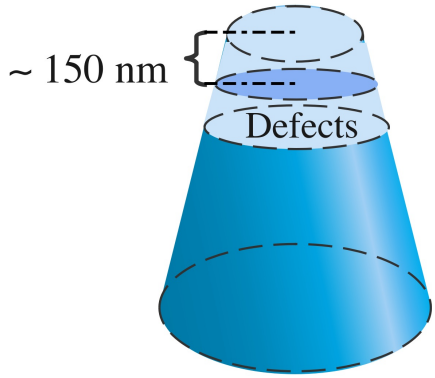

(b)

Figure 4.1: (a) SEM image of a nanopillar with r = 2 μm. Figure (b) is an illustration of the pillar with the light blue area indicating the expected location of V_{Si} with the peak of the defect concentration at 150 nm below the surface.

4.1 Cathodoluminescence measurements

The results from the CL measurements are presented in this section. CL was used for the identification of the V_{Si}^- and the acceleration voltage and probe current were optimized with respect to emission from V_{Si}^-. Intensity maps of the nanostructures obtained with the optimized parameters are presented here for an examination of how the shape and size of the nanostructures influence the emission. Lastly, the near-field obtained from FDTD simulations of an ensemble of defects in nanostructures is compared to the CL intensity maps.

4.1.1 Identification of V_{Si}

CL spectroscopy was used to identify the V_{Si}^- in the substrate and the nanostructures. A pillar with r = 2.4 μm is shown in Figure 4.2c for reference. As described in section 3.3, the CL setup is included in the SEM instrumentation. The SEM e-beam excites states in the semiconductor, including the defect states of V_{Si}. The resulting CL emission is collected on a diffraction grating to produce a spectrum. The e-beam will also excite states across the band gap as well as other deep-level defects. A CL spectrum for 4H-SiC showing the emission peaks from the band gap and the deep-level defects is shown in Figure 4.2a. The band gap emission appears around 400 nm, while the peak from deep-level defect emission is located at $\sim$ 500 nm and with a tail down towards 800 nm. This spectrum is obtained with the central wavelength set to 600 nm. The zero-phonon line (ZPL) of V1' and V1 is located at 858 and 862 nm, respectively, i.e., a higher central wavelength is needed to reveal emission from V_{Si}. Figure 4.2b shows the spectrum obtained with the central wavelength set to 800 nm. In this spectrum, the ZPL corresponding

to V_{Si} is visible and indicated in the figure, the phonon-side band (PSB) is seen as the broader peak at longer wavelengths than the ZPL. The spectrum also shows a peak at $\sim$ 790 nm; the identity of this peak is unknown and it did not appear on every measurement. The intensity of the tail belonging to the deep-level defect emission is considerably stronger compared to the emission from V_{Si}. In order to reduce the influence of this luminescence for further identification of V_{Si}, it was efficient to apply a longpass filter blocking out light with $\lambda < 700$ nm. Figure 4.4 is an example of a spectrum with a filter.

To further improve the CL signal, the acceleration voltage and probe current of the e-beam should be varied and optimized. The next section presents current and voltage tests of the CL signal concerning the CL intensity of V_{Si} for optimization of the CL signal for further characterization of the nanostructures.

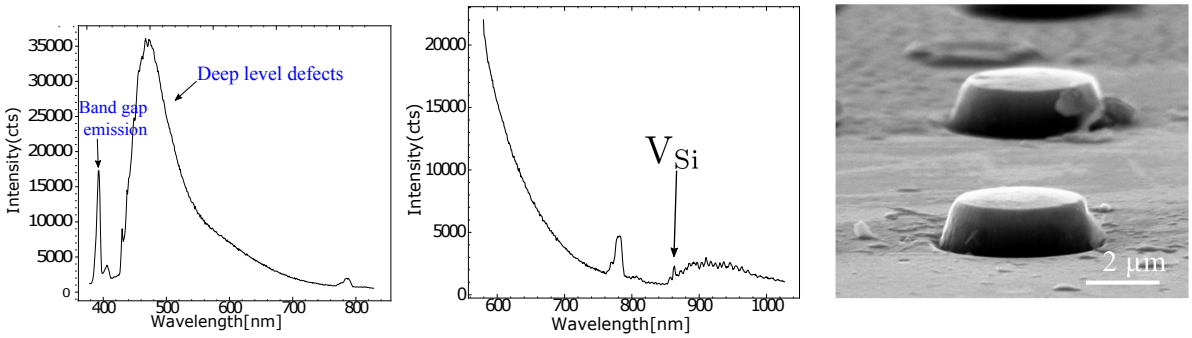

(a) (b) (c)

Figure 4.2: CL measurements on the 4H-SiC substrate, taken without filter with a central wavelength at (a) 600 nm and (b) 800 nm. The spectrum was obtained with an acceleration voltage of 10 kV and a probe current of 0.5 nA. Panel (c) is a SEM picture of two pillars with r = 2.4 μm. The image is obtained with an acceleration voltage of 18 kV.

4.1.2 Optimization of the cathodoluminescence signal

The signal from the sample relies only on the acceleration voltage and the probe current when the parabolic mirror is properly aligned. The probe current determines the number of electrons present in the beam, while the acceleration voltage determines the energy of the electrons and how deep the sample is probed. CL-series with changes in the acceleration voltage and the probe current have been performed for optimization of the CL signal from V_{Si}^{-} as the main focus. The voltage and current tests were conducted with the central wavelength at 850 nm and with a 700 nm longpass filter.

Voltage test

The silicon vacancies generated with ion implantation are, as mentioned, expected to be found from the surface and until a depth of $\sim$200 nm, with a peak at $\sim$150 nm. When electrons are directed towards a sample, the acceleration voltage of the electrons determines how deep the majority of the electrons will penetrate the sample, and hence the probing depth. The electron trajectory from an incident e-beam in solid materials can be simulated using the software program

CASINO [49]. CASINO simulations of the predicted penetration depth for acceleration voltages from 5 to 10 kV can be seen in Figure 4.3. A plot of probing depth on the x-axis and CL intensity on the y-axis is shown in the figure. The peak of the graphs shows where most of the CL signal is collected for a given acceleration voltage, indicated in the top right corner of the figure. From the simulation result, the highest CL intensity in the 0-200 nm depth is expected for 5 kV and 10 kV. However, to find the optimal acceleration voltage for CL characterization of V_{Si} in the sample used in this project a voltage test was performed with 5, 10, 15, and 20 kV. The probe current during the voltage test was held constant at 0.2 nA.

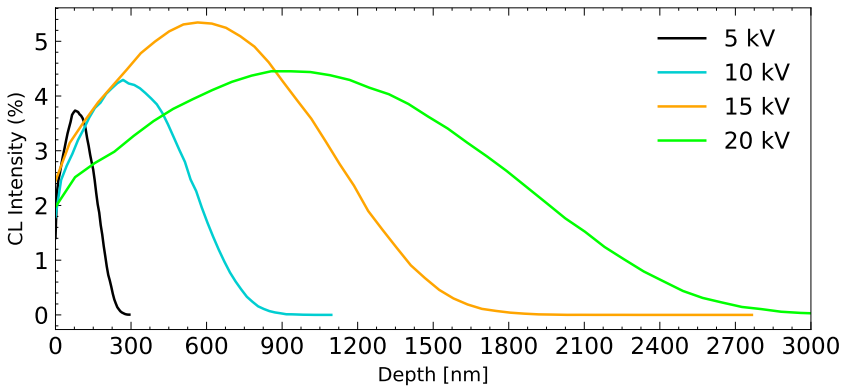

Figure 4.3: Results from Casino simulations for acceleration voltages from 5 kV to 20 kV. The CL intensity is plotted as a function of the e-beam's probing depth in nm.

Figure 4.4 presents the CL spectra for the different acceleration voltages. V_{Si} is indicated with an arrow in all spectra. The peak below V_{Si} (at $\sim$ 840 nm), appears on every measurement and should not be confused with V_{Si}. This peak was present also at background measurements with zero current and tended to shift as the central wavelength shifted, thus the peak is not considered a signal from the sample. The Casino simulations of the acceleration voltages indicate that when the acceleration voltage is increased, the probe will reach deeper into the sample and thus the spectrum obtained will represent more of the bulk properties of the material. This can also be seen in Figure 4.4 for high acceleration voltages where the V_{Si} peak is smaller compared to the deep level defects, indicating that the electron probe reaches deeper than the projected depth of implanted defects. The intensity of near band edge emission and deep-level defect emission from other defects is expected to rise proportionally to the interaction volume, and therefore to the acceleration voltage. For the lower acceleration voltages, 5 and 10 kV, it can be seen that the difference between the emission peak corresponding to other deep-level emission and the emission peak from V_{Si} is smaller compared to a larger difference for 15 and 20 kV, which probe deeper in the sample indicating less V_{Si} deeper in the sample. From this voltage test, 10 kV is found to be the optimal acceleration voltage for identifying emission from implanted V_{Si}.

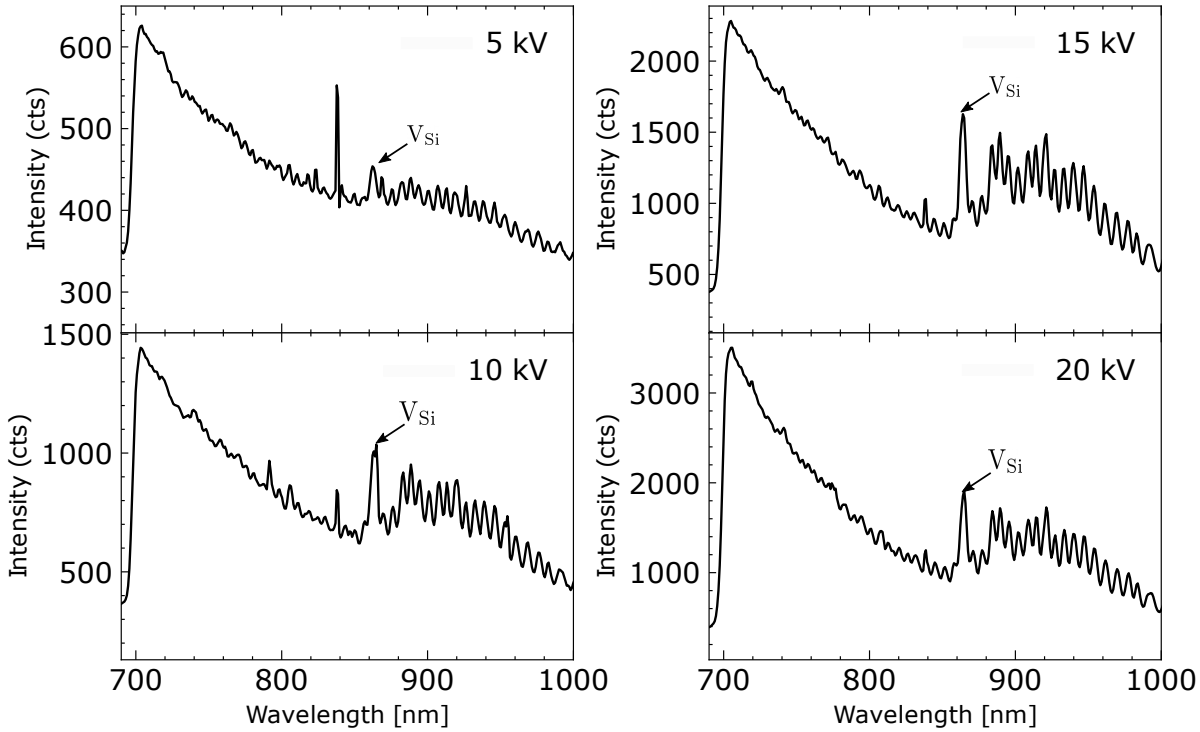

Figure 4.4: Voltage test of the CL signal, the probe current was held constant at 0.2 nA

Current test

High probe currents result in more electrons incident on the sample and will give higher emission intensity from the material. The signal-to-noise ratio will thus increase with an increasing probe current. However, high probe currents can lead to sample damage as well as a higher signal from other deep-level defects. Through a current test, the probe current was optimized for emission from V_{Si}^{-}.

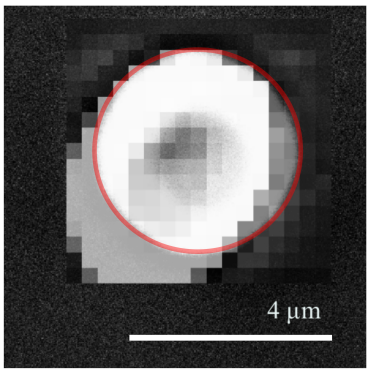

Figure 4.5: Drift of SEM image during CL measurements. The bright pixels indicate the SEM contrast in the pixels during the CL measurements, the pixels are shifted to the left compared to the initial SEM picture taken at the beginning of the measurement. The measurement was done with an acceleration voltage of 10 kV and a probe current of 0.3 nA.

High probe currents may also lead to an accumulation of charge in the probed area or charging of the sample. During CL measurements, charging of the sample led to an increase

in the signal from deep level defects which reduced the signal-to-background ratio from the V_{Si} peak. The following current test was therefore conducted on six different pillars to avoid a different degree of charging between the measurements. Charging may also potentially cause drift in the SEM image while performing measurements. The SEM contrast map, obtained from a CL measurement, is shown in Figure 4.5. The red circle outlines the edges of the pillar, and the SEM pixels from the CL map do not match the shape of the pillar. This was due to the large drift of the image during the measurement. The pixels of the CL intensity map correspond to the same pixels as in the SEM contrast in Figure 4.5. The location of these pixels is used to look at where the majority of the defect emission on the nanostructures results from. The drift of the image also increases as the pixel size is decreased and small pixels are needed for good resolution. It was therefore critical to keep the drift as small as possible for further characterization of the pillars.

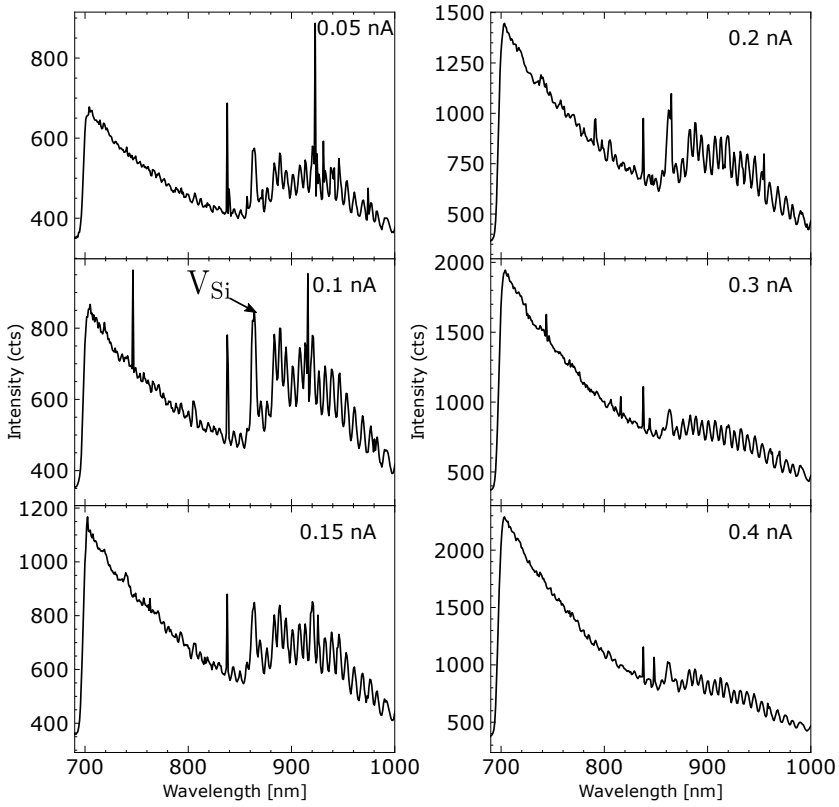

Figure 4.6: Current test of CL signal taken with 10 kV acceleration voltage, and 7 s exposure time.

The current test was performed for probe currents ranging from 0.05 to 0.4 nA, with the acceleration voltage held constant at 10 kV. The result from the current test is displayed in Figure 4.6. The V_{Si}^{-} peak is pointed out in the Figure with 0.1 nA and the peak to the left of V_{Si}^{-} should again not be considered a signal from the sample. The higher probe currents, on the right side of the figure, show a higher signal-to-noise ratio which increases together with the probe current. However, high probe currents result in less signal in the peak that belongs to V_{Si}^{-} compared to the emission intensity from other deep-level defects. From the 0.1 nA measurement, it is seen that the relation between the intensity from other deep-level defects and V_{Si}^{-} is almost

1:1. An increase to 1.15 nA shows significantly stronger intensity from deep-level defects. Thus, from this current test, a probe current of 0.1 nA was chosen as the optimal probe current for the detection of the ZPLs and PSB corresponding to V_{Si}^-. Other parameters that can be varied in the CL measurements are the exposure time, the central wavelength and the number and size of the pixels used. The exposure time refers to how long each CL pixel is exposed to the detector. A longer exposure time resulted in a higher signal-to-noise ratio and a CL signal with higher intensity. The sum of the exposure time and the number of pixels gives us the acquisition time which is the total time for a complete CL measurement. Longer acquisition times can also lead to drift in the image, and an exposure time of 7 s was found to be optimal for measurements in this project.

Optimized signal for V_{Si} observation

Finally, a spectrum where V_{Si}^- is measured by using the optimized acceleration voltage and probe current was taken. The purple line in the plot is located at 858 nm, which is associated with the V1' ZPL. The V1 ZPL is located at 862 nm and the peak in the spectrum can be a combination of the two ZPLs. The PSB of V_{Si}^- is located to the right of the ZPLs exhibiting longer wavelengths. The optimized probe current of 0.1 nA and acceleration voltage of 10 kV presented in this section were used for further characterization of the nanopillars both during the resulting CL measurements and characterization with ARCL.

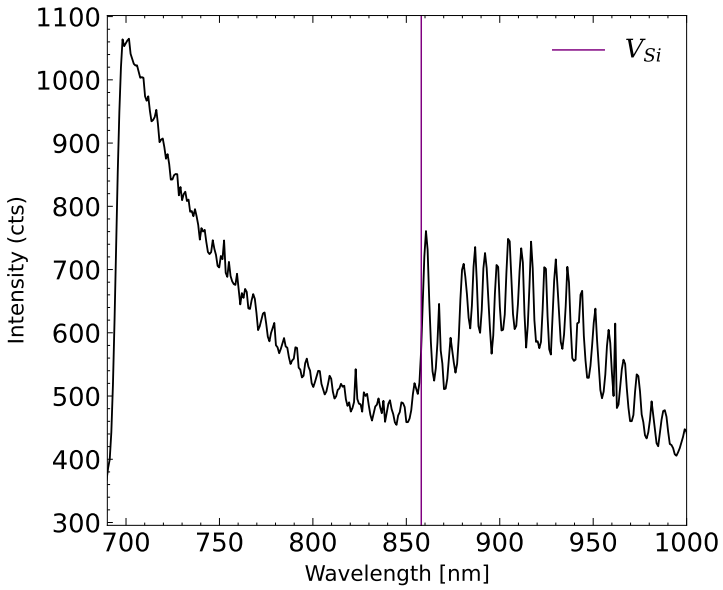

Figure 4.7: CL emission with visible emission from V_{Si}^-, the measurement is from the substrate and is obtained with 10 kV acceleration voltage, a probe current of 0.1 nA, and a 700 nm longpass filter.

4.1.3 V_{Si} emission from nanostructures

To investigate the influence of the nanostructures on the defect emission from V_{Si} and other deep-level defects, CL intensity mappings of the structures were performed and the spectra for the different pillar sizes were compared to each other as well as to the emission from the

substrate. SEM images of the structures are found in Figure 3.1 and the results are shown in Figure 4.10 and 4.11. The emission spectra are obtained by averaging over several pixels in the same measurement on respectively the substrate and the pillar. The presented intensity maps and spectra are raw data from the measurements and the signal-to-noise ratio is good enough to not affect the results. Figure 4.8a shows a pillar with r = 2.4 μm with white and blue circles as indications of where the emission spectra for the substrate and pillar are obtained. Figure 4.8b shows an outline of the top and bottom outer edges of the pillar. The emission spectrum for pillars with r = 1.4 and 1.9 μm are obtained in the same way.

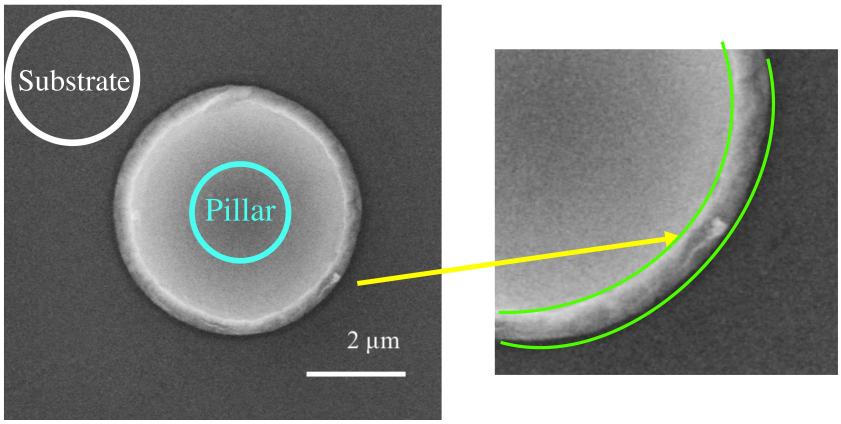

Figure 4.8: SEM image of a pillar with r = 2.4 μm. The circles in figure (a) indicate where the CL spectrum for respectively the substrate and the pillars are extracted from. Figure (b) shows a part of the pillar zoomed in on the sidewalls, the green lines correspond to the top and bottom outer edges of the pillar. The image is obtained with 20 kV acceleration voltage.

A measurement with a center wavelength at 600 nm without a longpass filter was performed on a pillar with r = 1.4 μm to investigate how the pillars impact emission from band-to-band recombination and deep-level defects. Figure 4.9 shows the intensity maps and spectra obtained from this measurement. A broadband filter implemented in Odemis was used to obtain the CL intensity maps. Bright pixels in the intensity map indicate a pixel where high intensities of wavelengths in the selected bandwidth were detected. Figure 4.9a shows an intensity map where the center wavelength of the broadband filter is set to 480 nm. The pixels around the pillar show higher intensities compared to the pixels on the pillar, meaning that the substrate show higher intensities for bandgap emission compared to the pillar. However, when the center wavelength is set to 700 nm in the broadband filter, as in Figure 4.9b, the pillar shows higher intensities compared to the substrate. The emission in this wavelength range corresponds to deep-level defect emission. The emission spectrum obtained from this measurement is displayed in Figure 4.9c, where the blue graph corresponds to the pillar and the black graph to the substrate. This spectrum outlines the differences between the substrate and the pillar seen in the intensity maps. The results from this measurement show that the emission intensity from deep-level defects is significantly increased by the pillar.

For investigation of how the nanostructures influence emission from V_{Si}, the center wavelength was set to 850 nm and a 700 nm longpass filter was applied. The emission spectrum for pillars with r = 1.4, 1.9, and 2.4 μm are shown in Figure 4.10. Emission from the substrate

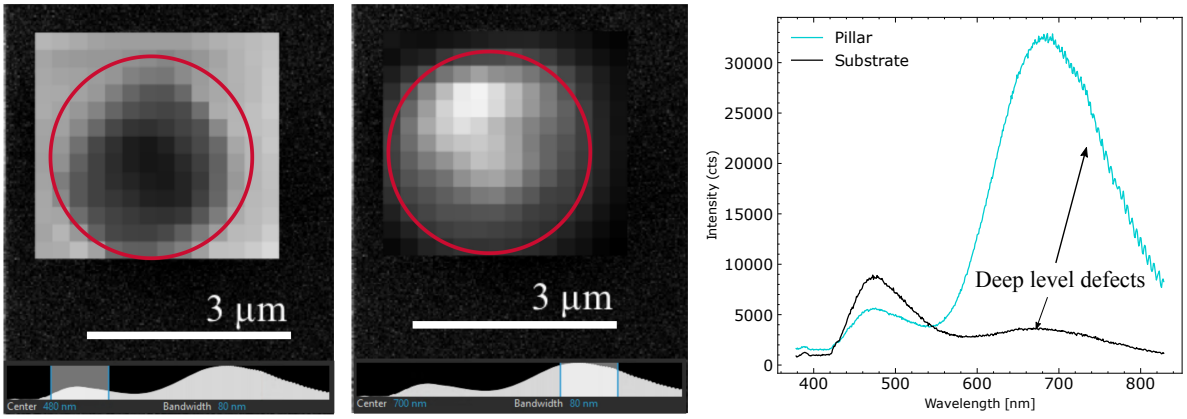

(a) (b) (c)

Figure 4.9: CL measurement without a filter of a pillar with r = 1.4 μm. The acceleration voltage was 10 kV, the probe current was 0.1 nA and the center wavelength was set to 600 nm. Panel (a) shows the CL intensity map with a bandwidth ranging from λ = 440 to 520 nm. Panel (b) shows the intensity for wavelengths ranging from λ = 660 to 740 nm. The emission spectrum obtained from the measurement is shown in (c) with the blue graph extracted from the pixels on the pillar and the black graph from pixels on the substrate.

collected during the same measurement is compared to the emission from the pillars. The pillar with r = 2.9 μm was not measured as the difference between this one and r= 2.4 μm was expected to be small. All of the pillars show an increased emission intensity relative to the substrate from V_{Si} as well as from the deep level defects. If we compare the intensity at the 862 nm peak, the emission intensity from the V_{Si}^{-} displays an increase of ∼23% in the smallest pillar compared to the measurement outside the pillar, while the two other structures, with r = 1.9 and 2.4 μm, had an increase of ∼9% and ∼16%, respectively. However, for the smallest pillar, the increase is the largest, also for the deep level defects. For r = 1.4 and 1.9 μm, the increase in the deep level defects is substantially larger than the increase in the emission from V_{Si}. Since the smallest pillar has the highest increased emission intensities both for V_{Si} and for the deep level defects, and its diameter is approaching the size of the emitted wavelengths, the enhanced emission may indicate a waveguiding effect. Note that the measurements are not from the same session and only one pillar of each size is measured.

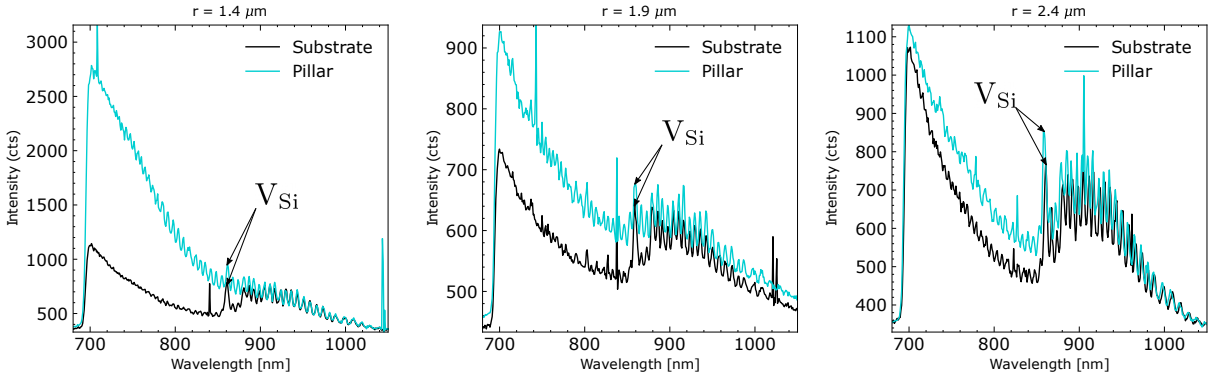

Figure 4.10: Emission spectrum obtained from CL measurements on the substrate and on pillars with r = 1.4, 1.9, and 2.4 μm. The blue graphs are from the pillars and the black graphs are from the substrate. An acceleration voltage of 10 kV and a probe current of 0.1 nA were used.

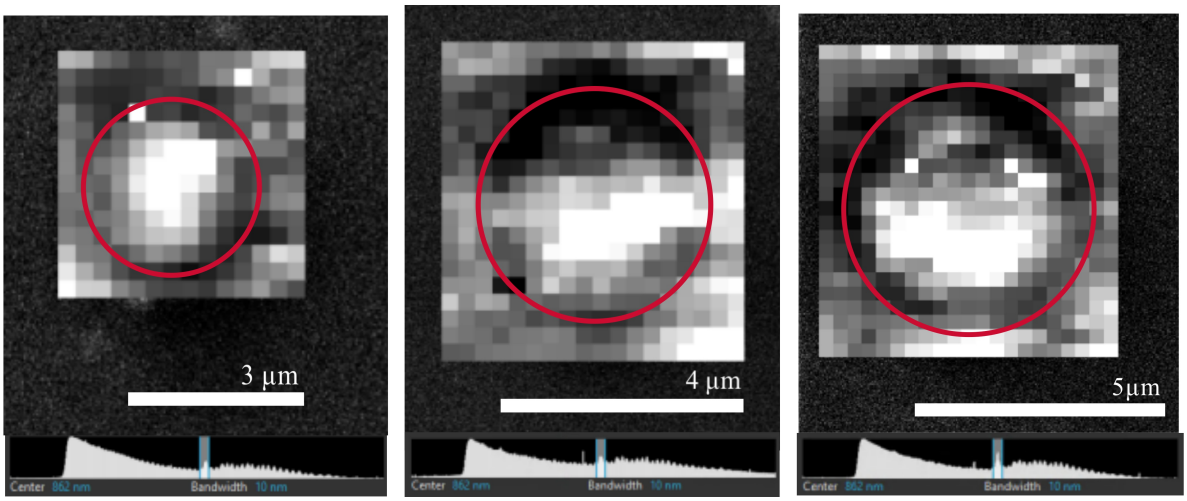

(a) (b) (c)

Figure 4.11: CL intensity maps of pillars with radius of (a) r = 1.4 μm (b) r = 1.9 μm and (c) r = 2.4 μm (Acceleration voltage of 10 kV and probe current of 0.1 nA). The bright pixels indicate high emission intensity in the selected bandwidth. The bandwidth is selected to 10 nm centered at 862 nm for all intensity maps. The spectrum with the selected bandwidth is indicated under each intensity map.

The structure's influence on the emission from V_{Si}^- has been explored by looking at CL intensity maps of the structures. The intensity maps for pillars with r = 1.4, 1.9, and 2.4 μm are shown in Figure 4.11. The wavelengths selected for the broadband filter range from 857 to 867 nm with the center at 862 nm, corresponding to the V1 ZPL of V_{Si}^-. The spectrum with the selected bandwidth is displayed under each intensity map. All intensity maps in Figure 4.11 show stronger intensities in the middle of the pillar. However, the intensities of the r = 1.9 and 2.4 μm pillars show intensities slightly shifted from the center of the pillar. This may be due to an uneven distribution of defects, or due to surface effects not visible on a SEM image. In addition, all intensity maps in Figure 4.11 show low intensities for the selected bandwidth in a circle on the outer edges of the pillars. These pixels correspond to the walls of the pillars as seen in Figure 4.8. This SEM image of the pillar also reveals more surface roughness on the sidewalls than on the top of the pillar and on the substrate. An explanation for the low intensities in this area might be the possible reflection of light inside the pillar, and the angle of the light refracted at the sidewall. The surface roughness of the sidewalls may also lead to the reflection of light inside the pillar and might lead to less signal collected in the CL setup. In this manner, the light reaching the CL detectors will be suppressed from the sidewalls.

4.1.4 Comparison with FDTD simulations

When producing a CL intensity map, the e-beam excites one pixel at a time, the emission from this pixel is collected on the mirror above the sample, detected at the spectrograph and converted to a spectrum. The information about the angles of the light is lost during this process but instead we gain information about the emitted wavelengths. As described above, the intensity maps are constructed by selecting the bandwidth of interest. Each pixel on the intensity map gives information about the emission intensity from only this pixel. For a better understanding

of the field obtained from FDTD simulations and to determine how the CL intensity maps can be compared to FDTD, a near-to-far-field analysis is conducted.

Near-to-far-field

Figure 4.12 shows the field at different distances from the simulation region for one dipole in a pillar with r = 2.4μm. Figure 4.12a shows the near-field which is collected from the monitor positioned 0.2 μm above the pillar. The area showing high intensity corresponds to the position of the dipole. The remaining images are of the field calculated outside of the simulation region, these are acquired with the *farfieldexact3d* function in Lumerical which calculates the field at a hemisphere above the simulation region similar to the far-field explained in section 3.4.5, this field does therefore contain information about the angular distribution of the emission.

As the distance from the simulation region is increased to 1, 2 and 3 μm in Figures 4.12b, 4.12c, and 4.12d the intensities are more spread out. However, the position of the dipole still shows the highest intensity for all distances. As the distance is increased further to 10 μm, in Figure 4.12e, the intensity is strongest in the center of the hemisphere, which is also right above the pillar. Some interference patterns can be observed but this is more clear when the distance is increased to 10 cm in Figure 4.12f. This image also shows the highest intensity at the center. The fields calculated further away from the simulation region are angle-resolved at a hemisphere, therefore, the near-field is most suitable for comparison with CL intensity maps. This is done by the summation of several dipoles with random positions. The sum of the near-field from each dipole then reveals information about the intensity at different positions in the pillar, giving qualitatively the same information we obtain from the CL intensity maps.

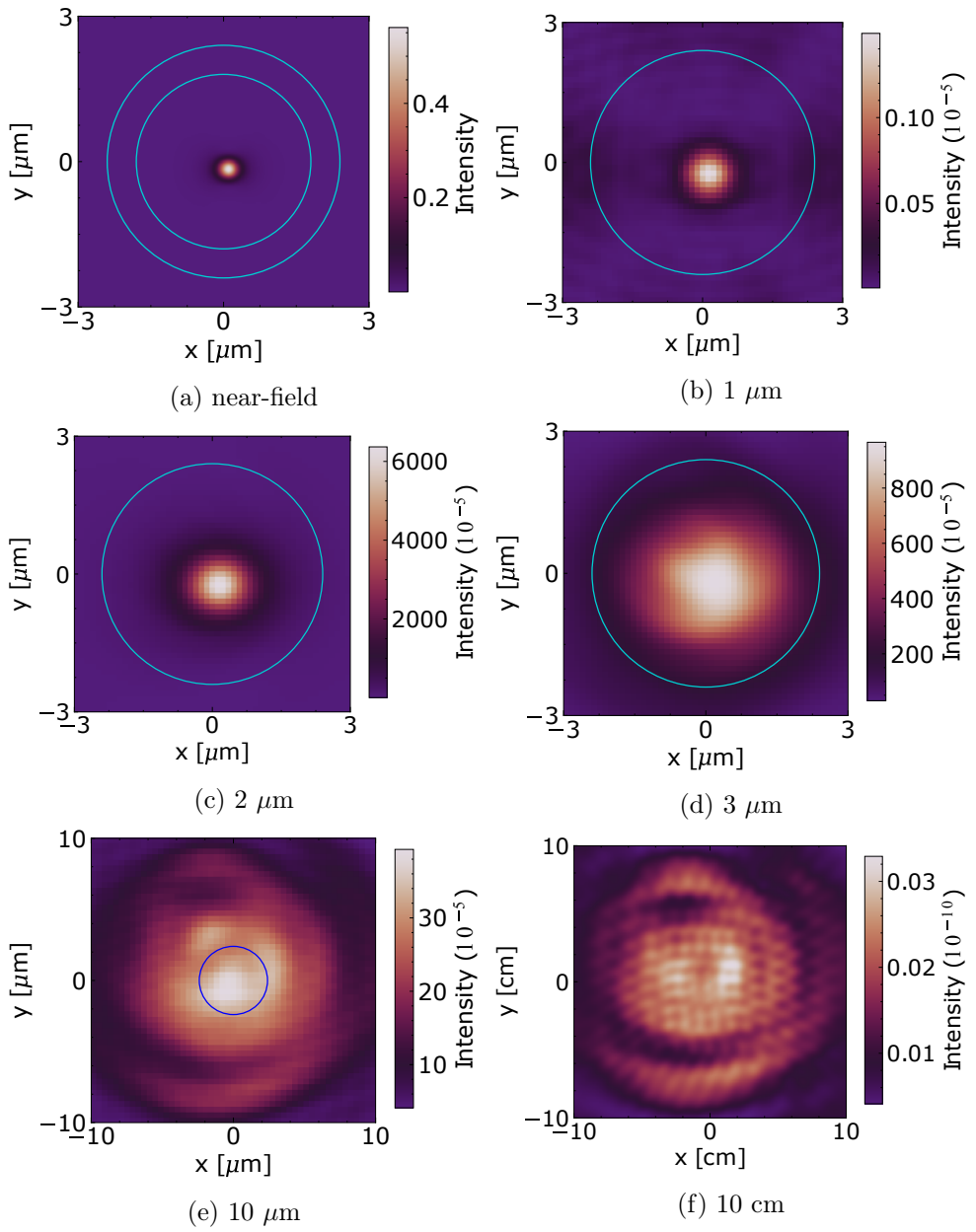

Figure 4.12: Series of fields calculated at increasing distances from the simulation region. The fields are obtained from a pillar with r = 2.4 μm. The bottom radius of the pillar is outlined as the blue circle in the pictures where it is visible.

Comparison between CL and FDTD

FDTD simulations of a pillar with r = 1.9 μm are conducted for qualitative comparison between the near-field and CL intensity maps. FDTD simulations can be used to investigate the variation in emission intensity on the pillar by looking at the intensity from the near-field related to the dipole position. The wavelength of the oscillating dipole was set to 895 nm to represent an average of both ZPL and PSB, but should ideally be set to 862 for replication of the V_{Si}^- ZPL. However, because the structures are much larger than the wavelength simulations with 862 nm gave similar results. The dipoles were placed 150 nm below the surface in the xy-plane within a radius of 1.25 μm, corresponding to the upper radius of the pillar. 125 dipoles are placed in the pillar and the field from all simulations is summed together. Figure 4.13 shows the sum of the near-field, and the intensity is divided by the number of dipoles. Even though the density of dipoles is slightly less in the center of the pillar, the intensity from the near-field is strongest at the center. Both CL and FDTD thus reveal intensity variation across the pillar.

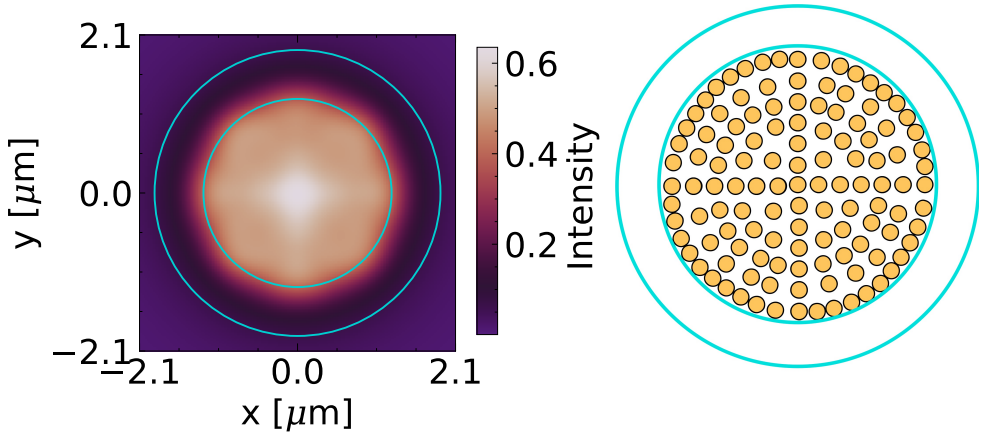

(a) (b)

Figure 4.13: (a) Near-field from the sum of 125 individual dipoles. The blue circles outline the upper and lower edges of the pillar with r_{bottom} = 1.9 μm and r_{top} = 1.25 μm. Figure (b) shows the dipole positions as yellow circles, the dipoles are placed within a radius of 1.25 μm

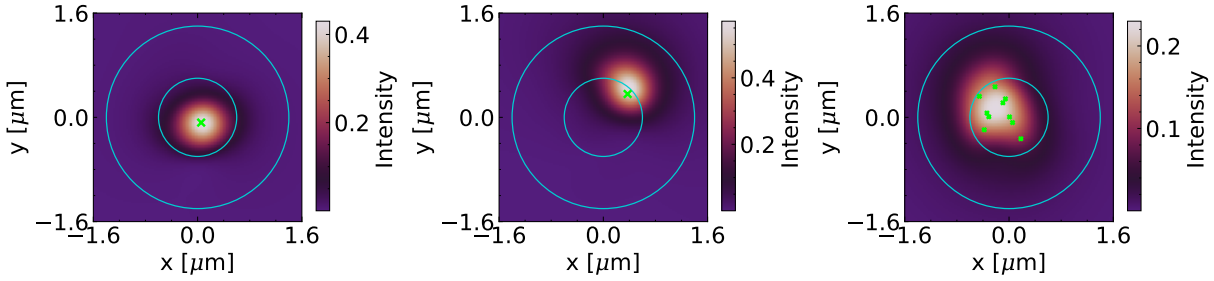

(a) (b) (c)

Figure 4.14: Near-field from a pillar with r = 1.4 μm. Figures (a) and (b) are from one dipole in two different positions. Figure (c) is the sum of the field obtained from 10 dipoles, the intensity is divided by the number of dipoles. The green crosses indicate the positions of the dipoles.

The pillars with r = 1.4 and 2.4 μm have also been simulated, but with random dipole

positions. A number of respectively 10 and 90 dipoles in each pillar give the same density of dipoles. Figure 4.14 shows the near-field from a pillar with r = 1.4 μm. Figures 4.14a and 4.14b show the field from two individual dipoles with different positions and figure 4.14c shows the near-field obtained from the sum of 10 dipoles, the intensity is in this plot divided by the number of dipoles. The green crosses represent the position of the dipoles, while the blue circles illustrate the top and bottom radii of the pillar. The sum of the near-field shows that the position of dipoles mostly influences the summed intensity, but as seen in Figure 4.14b, dipoles placed near the sidewalls have a more spread out intensity which is also stronger.

The near-field image from the pillar with r = 2.4 μm from one dipole placed near the edge of the pillar and the sum of the field from 90 dipoles are displayed in Figure 4.15. Figure 4.15a shows the field from an individual dipole which is shifted away from the position of the dipole, indicated with the green cross, and towards the center of the pillar. The intensity is also highest in the center of the pillar when all 90 dipoles are summed together in the figure to the right. The intensity from a dipole placed near the sidewall in the smallest pillar shows a more spread-out intensity compared to the pillar with r = 2.4 μm. The CL intensity map in Figure 4.11 also shows brighter pixels around the outer edges of the r = 1.4 μm pillar compared to the two other pillars with r = 1.9 and 2.4 μm. The near-fields obtained from FDTD simulations are not directly comparable to CL intensity maps, but the fields give information about the intensity with respect to the dipole position in the pillar which is somewhat similar to what we can read from a CL intensity map.

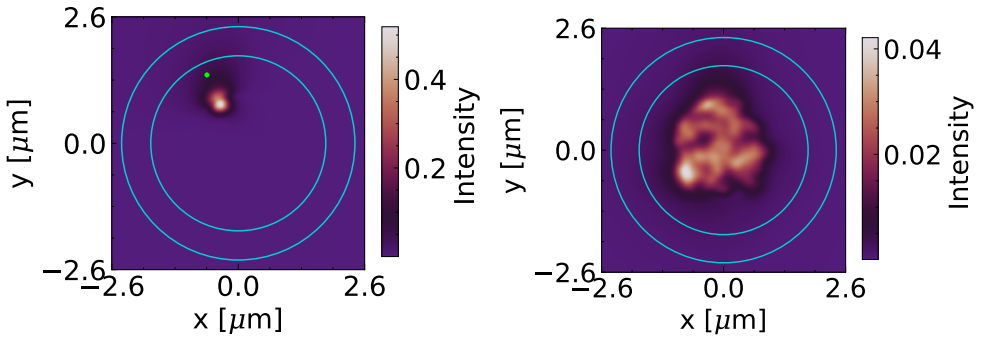

Figure 4.15: Near-field from (a) one dipole placed on the edge of the pillar and (b) the sum over 90 dipoles in a pillar with r = 2.4 μm. The blue circles indicate the top and bottom of the pillar.

4.2 Angle-resolved cathodoluminescence measurements.

Angle-resolved cathodoluminescence (ARCL) has been employed for the investigation of the nanostructures' radiation profiles. ARCL reveals the intensity in relation to the emission direction above the sample, see section 3.3.1. The luminescence from the band edge and the defects are considered to arise from Lambertian emitters, which means they emit incoherent CL signals. In addition surface effects like plasmons may be present, resulting in distinct radiation profiles. However, the near band edge emission and defect emission are often substantially stronger. The angle-resolved radiation will depend on the structure of the surface, thus the photonic properties

of the nanostructures can be determined by comparing the emission profiles of the nanostructures to the emission profiles of the substrate. The polar emission profiles obtained from ARCL are compared to simulation results of the far-field and used for validation of the developed FDTD simulation method.

Emission signals induced by the e-beam are collected by a parabolic mirror and projected onto a CCD screen. The software transforms the 2D picture from the CCD screen into a polar intensity plot. If the mirror is well-aligned, each pixel of the CCD screen will correspond to a point on the parabolic mirror and the polar intensity images are thus 2D representations of the hemisphere above the sample. The intensity image from ARCL is, therefore, best described by the far-field intensity simulated using FDTD. Some post-processing of the ARCL data is performed to represent the polar emission profiles from the 2D polar intensity data. The post-processing to obtain the polar plots as well as parameter choices for optimization of the polar plots are explained below.

4.2.1 Optimization of angle-resolved radiation profiles

As the signal from ARCL measurements is spread out over a 2D imaging array, it is suggested by the producer of the CL software used, Odemis, that the exposure time is longer than for normal CL measurements. The appropriate exposure time depends on the sample brightness as well as filter selection. Through a series with different exposure times, it was found that an exposure time of 60 s was sufficient for the measurements. It was noted that long exposure times might lead to drift during the measurement. However, the number of pixels used during an ARCL measurement was less than during the CL measurements and drift was not observed to be a problem during the ARCL measurements. All of the measurements were conducted with a 700 nm longpass filter and with an acceleration voltage and probe current of respectively 10 kV and 0.1 nA. For every AR measurement, a dark measurement was performed with zero probe current. This is performed to remove background effects and artifacts.

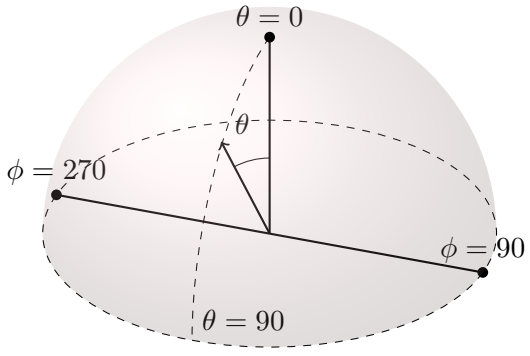

Figure 4.16: Schematic illustration of the hemisphere where emission is collected above the sample. The azimuthal angle ϕ ranging from 0 to 2π and the zenithal angle θ ranging from 0 to π are indicated in the figure.

Figure 4.17a shows a 2D intensity image as a function of ϕ. Bright areas correspond to the detection of high intensities. Each point in the image is associated with a distinct θ and ϕ angle

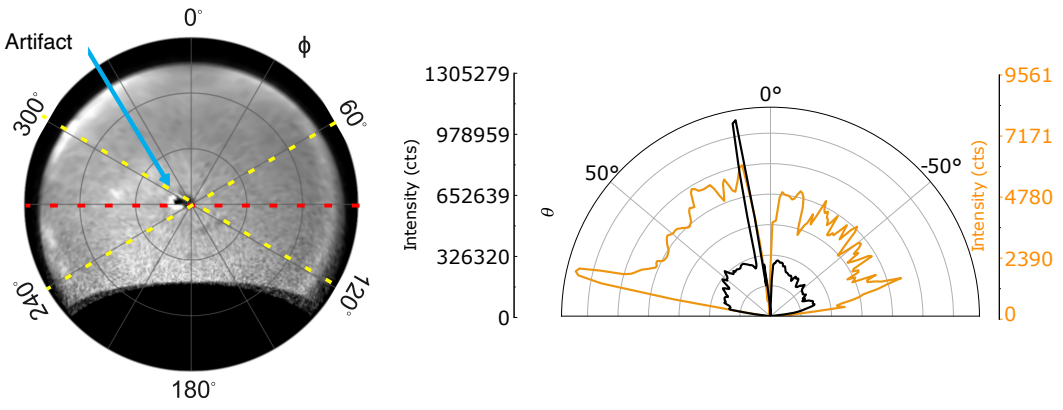

(a) (b)

Figure 4.17: (a) shows intensity as a function of ϕ. Figure (b) is a polar plot as a function of θ for the cross-section of $\phi = 90°$, 270 °(black graph), corresponding to the red line in Figure (a) and an average over $\phi = [240°, 300°]$ for positive θ and $\phi = [60°, 120°]$ for negative θ (orange graph). Obtained with an acceleration voltage of 10 kV and a probe current of 0.1 nA

on the hemisphere above the sample, the angles are indicated in Figure 4.16. The dark region between $\phi = 120°$ and 240° marks the end of the parabolic mirror. The polar emission profiles as a function of θ are obtained from the 2D polar intensity image. The polar emission profiles can be plotted by choosing a cross-section, represented by two ϕ values in the 2D intensity image. However, the mirror has an artifact visible as a bright spot on every measurement which appeared on the plot of the center cross-section. It was clear that the artifact did not come from the sample as the bright spot also was present on the background measurements taken with zero probe current. Figure 4.17b shows a plot of this cross-section, $\phi = 90°$ and 270°, which intersects with the bright artifact. Since the intensity is strong in the artificial spot, it becomes the dominating feature in the polar plot making detailed analysis difficult. A background measurement removed the bright spot to some degree but data from this region will be missing, and in some measurements, a part of the intensity from the artifact is not removed. The $\phi = 90°$ and 270° cross-section is a natural selection for plotting the polar radiation profiles. However, due to the artifact present on the parabolic mirror, a different approach was used. The area with the bright artifact is avoided by plotting the average intensity over ϕ in an interval on each side of the intensity image. This is presented in Figure 4.17b as the orange graph. Positive θ values correspond to $\phi = [240\ °, 300°]$ while negative θ values correspond to $\phi = [60\ °, 120°]$. The polar emission plots displayed in the rest of this section are plotted by the averaging process explained here. There is zero intensity in the middle of the plots, which is a result of the hole in the mirror for the incident e-beam.

4.2.2 Angle-resolved emission from V_{Si} in nanostructures

The V_{Si} signal from CL in the sample with nanostructures showed that the emission is enhanced on the pillars relative to the emission from the substrate. For investigation of the directionality of the emission from V_{Si}, each pillar size is measured with ARCL, and compared to measurements of the substrate. Figure 4.18a shows a polar emission profile for a pillar with r = 1.4 μm and the substrate while Figure 4.18b shows the 2D intensity images. The substrate, presented as the

black graph, shows the Lambertian emission profile we expect from a flat surface. The pillar shows higher intensities detected on the edges of the hemisphere, for high angles of θ, compared to the emission from the substrate. As the size of the pillar is increased the intensity on the edges decreases. Figure 4.19 shows results obtained from a measurement on a pillar with r = 2.4 μ and the substrate. This pillar also shows higher intensities outwards for higher θ angles. Interestingly, the difference between the pillar and the substrate is significantly larger for the pillar with r = 1.4 μm. The pillars with a larger radius all show similar behavior and the results obtained for r = 1.9 and 2.9 μm are found in Appendix A.1. The pillar with r = 1.4 μm has the sidewalls with the steepest angles. More of the light that would normally get reflected at a straight sidewall would escape a structure with titled sidewalls, this leads to more light escaping the semiconductor-air interface and providing the nanostructure with a lens-like effect.

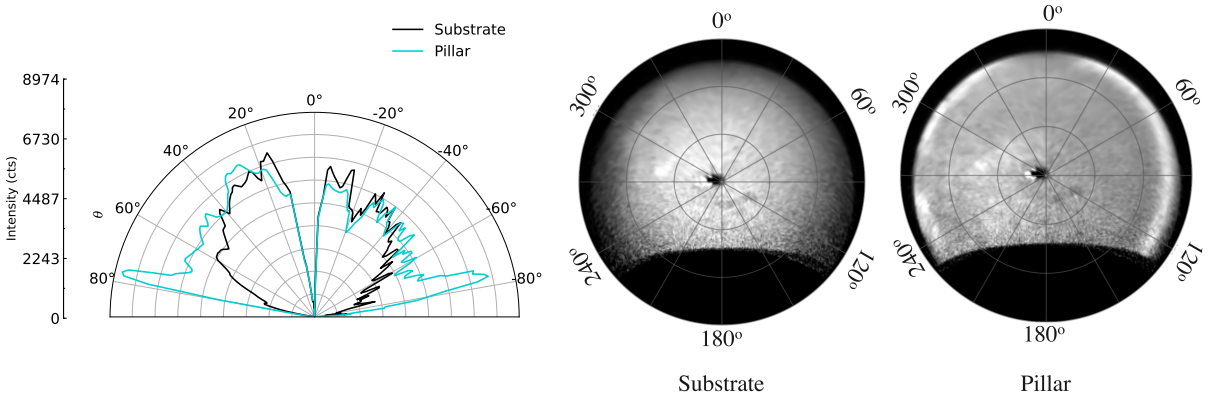

(a) (b)

Figure 4.18: Figure (a) is polar emission profiles extracted from ARCL intensity images in (b) of a pillar with r = 1.4 μm and the substrate from the same measurement. Obtained with an acceleration voltage of 10 kV and a probe current of 0.1 nA

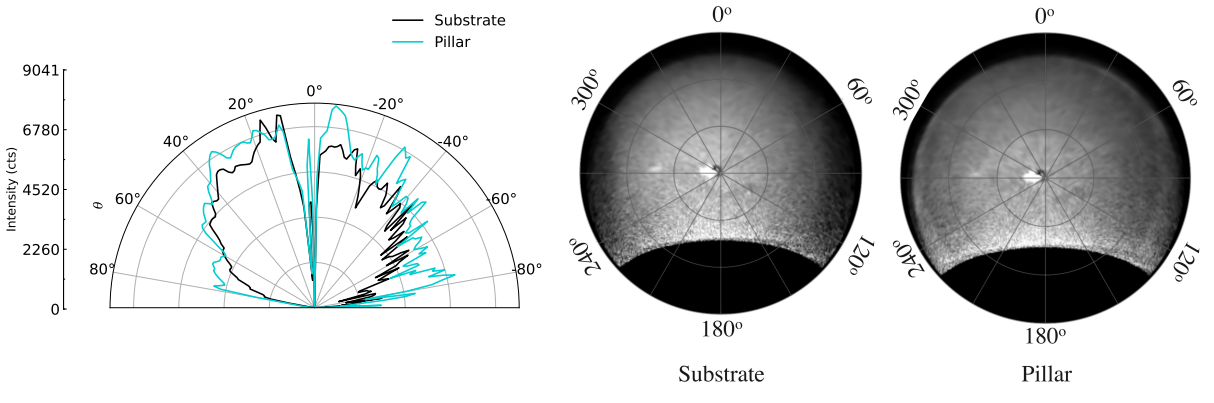

(a) (b)

Figure 4.19: Figure (a) is polar emission profiles extracted from ARCL intensity images in (b) of a pillar with r = 2.4 μm and the substrate from the same measurement. Obtained with an acceleration voltage of 10 kV and a probe current of 0.1 nA

Change of e-beam position

An AR measurement where the position of the e-beam was varied through a cross-section of the pillar was conducted to look for differences between different positions in the pillar. The e-beam will excite defects in an area around its position, thus the measured emission will come from a larger area than the e-beam spot size, but we assume the majority of the detected emission result from the position of the e-beam. Figure 4.20 shows the polar plots obtained from two measurements on each side of the pillar. A SEM picture of the measured pillar is displayed in Figure 4.20a, and the radiation profile in this Figure is obtained from the front of this pillar. The radiation profile in Figure 4.20b is obtained from the opposite side of the pillar. E-beam positions for (a) and (b) are also outlined in Figure 4.21c. The 2D intensity images are shown in Figure 4.21, where (a) and (b) in this figure correspond with (a) and (b) in Figure 4.20. Both e-beam positions show high intensities towards the upper edges on their respective sides, indicating an increased emission at large angles, in accordance with the previous measurements (Figure 4.18 and 4.19). However, the intensities from position (a) are substantially higher for high angles of θ and the radiation profile of position (b) shows higher intensities towards the (a)-side. The 2D intensity image for position (b) also reveals higher intensities towards the edges, but the difference is smaller due to higher intensities for ϕ between 240° and 300°. The differences in intensities may arise from an uneven distribution of defects or the shape of the pillar. The results motivate the development of FDTD simulations that can be compared with the ARCL measurements, in order to better understand the origin of the deviations from the Lambertian source.

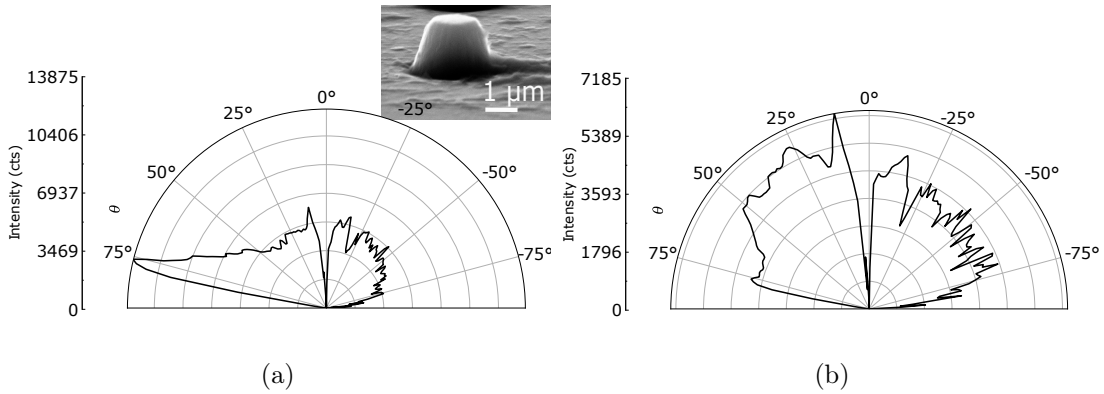

(a) (b)

Figure 4.20: Polar emission profiles from ARCL measurements on a pillar with r = 1.4 μm, the measurements are taken at two different points on the pillar. Figure (a) is from the side visible on the SEM picture, while (b) is taken from the opposite side. Obtained with an acceleration voltage of 10 kV and a probe current of 0.1 nA

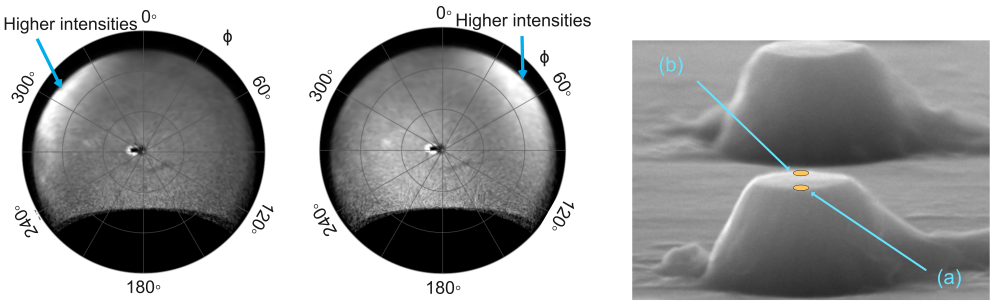

(a) (b) (c)

Figure 4.21: 2D intensity images from an AR measurement with the e-beam in two different positions (a) and (b). The e-beam positions are indicated in (c). Obtained with an acceleration voltage of 10 kV and a probe current of 0.1 nA

4.2.3 Comparison with FDTD simulations

The polar plots obtained from ARCL measurements show that as the pillar increase in size the shape of the polar plots looks more like the substrate with a Lambertian emission profile. A small pillar shows more outward-directed intensity, i.e., a stronger intensity at high θ angles. The method developed in section 3.5 is used for comparison between FDTD and ARCL results. The near-field from the simulations was used for qualitative comparison with CL results. However, when comparing ARCL with FDTD, the far-field calculated at a 1 m distance from the simulation region is suitable. The simulation results presented herein were obtained by summing individual dipoles incoherently and dividing the result by the number of dipoles. The polar radiation profiles are obtained from an averaging over several cross-sections in the ϕ=[0,90°] range of the far-field intensity images. The script for the averaging and the acquisition of the far-field can be found in Appendix B.2.

Figure 4.22 shows the far-field images from three simulations on pillars with r = 1.4 and 2.4 μm and the substrate. The sum of 10 dipoles is used in the simulation of the pillar with r = 1.4 μm and to obtain the same density of dipoles, 90 dipoles are summed in the pillar with r = 2.4 μm. The resulting intensity is divided by the number of dipoles. The positions of dipoles are randomized and will influence the far-field emission, but as the number of dipoles increases, this difference is less important. The far-field intensity images obtained from simulations of pillars with (a) r = 1.4 μm and (b) r = 2.4 μm, and (c) the substrate are displayed in Figure 4.22. The pillars in Figure 4.22a and 4.22b show intensities spread to the outer edges of the hemisphere, while the emission intensity from the substrate in Figure 4.22c is mostly centered. The intensity images from ARCL measurement of the pillars and the substrate in Figures 4.18 and 4.19 also show a similar trend.

Figure 4.23a shows the polar emission profiles obtained from the far-field images. The experimental polar plots from the corresponding pillars are shown in Figure 4.23b. The r = 1.4 μm and r = 2.4 μm data are from different measurements, which may be the cause of the intensity differences between these two pillars. The emission profiles from the substrate are also included and these intensity variations may also be because the data are from two different measurements. However, the substrate shows the expected Lambertian emission profile in both

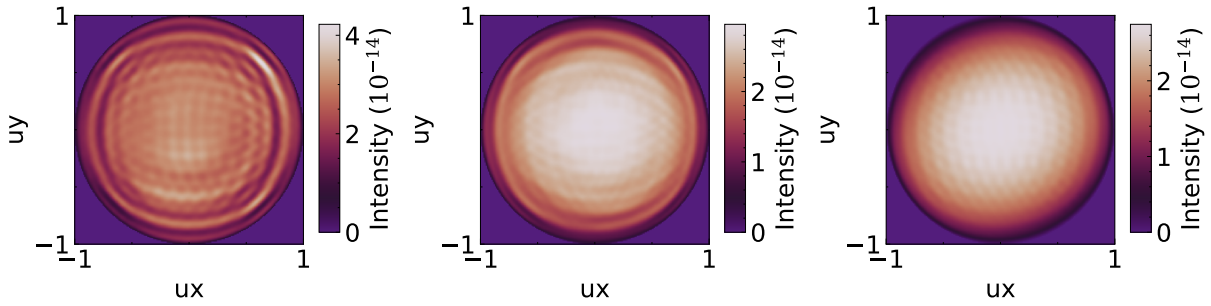

(a) (b) (c)

Figure 4.22: Far-field intensity for an ensemble of emitters in pillars with (a) r = 1.4 μm, (b) r = 2.4 μm and (c) from the substrate

the simulations and the experimental data, while the pillars in both figures deviate from the Lambertian profile. Similar to both the experimental and the simulation results is also the fact that the outward-directed intensity is higher for the pillars compared to the substrate. The variations between positive and negative values of θ seen in the radiation profiles from the FDTD simulations in Figure 4.23a are due to the positions of dipoles since the simulated pillars are symmetric. The smallest pillar, r =1.4 μm, shows in both figures the highest intensities for high θ angles, however, the ratio between the intensities at θ=0° and 80° differs between the simulation results and the experimental results. The emission profile from the simulation shows the highest intensities for θ=0°, while the experimental emission profile has the highest intensity at θ ∼80°. However, the far-field intensity obtained from FDTD qualitatively shows the same trends as the experimental results. The FDTD method is further used for comparison between experimental ARCL measurement with different e-beam positions and FDTD simulations for different dipole positions.

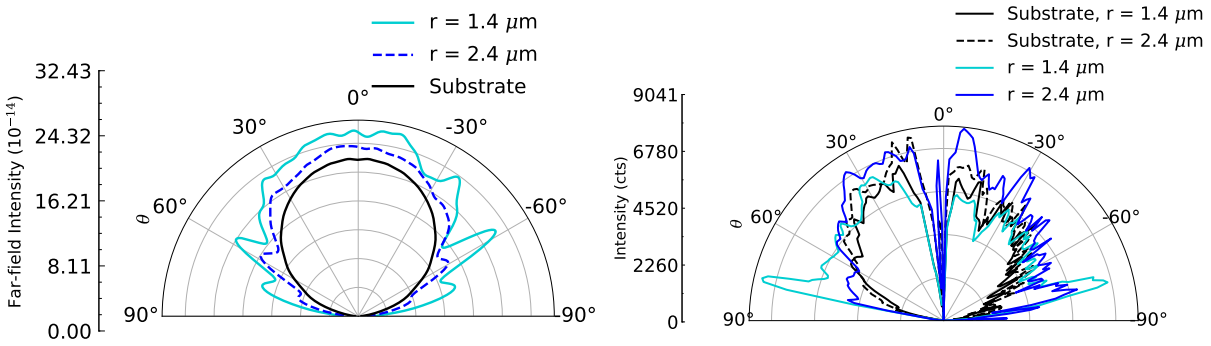

(a) (b)

Figure 4.23: (a) Radiation profiles obtained from FDTD simulations on a pillar with r = 1.4 and 2.4 μm and the substrate. The radiation profiles are plotted from an average of the $\phi \in [0, 90°]$ cross-sections. Figure (b) is the experimental ARCL radiation profiles from the corresponding pillars and the substrate.

Influence of emitter position

To better understand the non-uniformity observed in the CL and ARCL measurements a FDTD simulation conducted with one dipole in different positions is used. Figure 4.24 marks the different dipole positions, the top radius of the pillar is 0.6 μm. The numbers in the figure correspond to the four different dipoles with respectively (1) 0.6 μm, (2) 0.4 μm, (3) 0.2 μm, and (4) 0 μm offset from the center of the pillar in the x-direction. The far-field intensity obtained

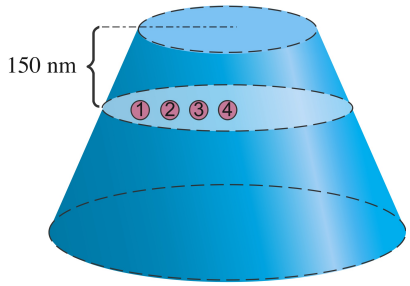

Figure 4.24: Dipole positions 1, 2, 3 and 4 in a symmetric pillar with r_{bottom} = 1.4 μm and r_{top} = 0.6 μm.

from the different dipole positions is displayed in Figure 4.25. The field from dipoles 1 and 3 tend to have higher intensities directed towards the opposite side of the dipole position. This can also be seen in the polar plots shown in Figure 4.26, where the radiation profiles for the different positions are displayed. The far-field intensity from dipole no. 2 however, has emission directed towards the same side as the dipole position. This position is also the one with the most outward-directed intensity. The far-field intensity obtained from FDTD in Figure 4.26 show similarities to the emission from ARCL shown in Figure 4.20. However, the pillar in the simulation is symmetric and differences observed from ARCL may come from asymmetric tendencies of the experimental nanopillar. Simulation results of an asymmetric nanopillar are presented in the next section and the pillar shape's impact on the emission is presented. This comparison between the ARCL measurements and the simulation results shows that the simulation method developed in this project can be used to explore the properties of structures in a size domain much smaller than what is practically possible in the lab.

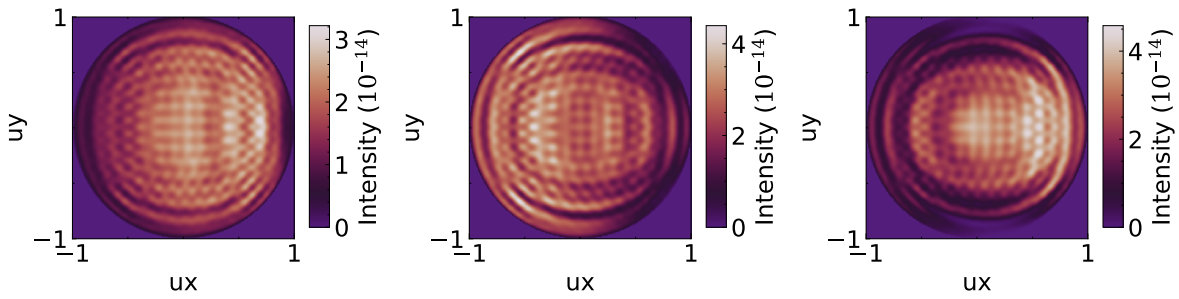

(a) Dipole no: 1 (b) Dipole no: 2 (c) Dipole no: 3

Figure 4.25: Far-field intensity from a pillar with different dipole positions

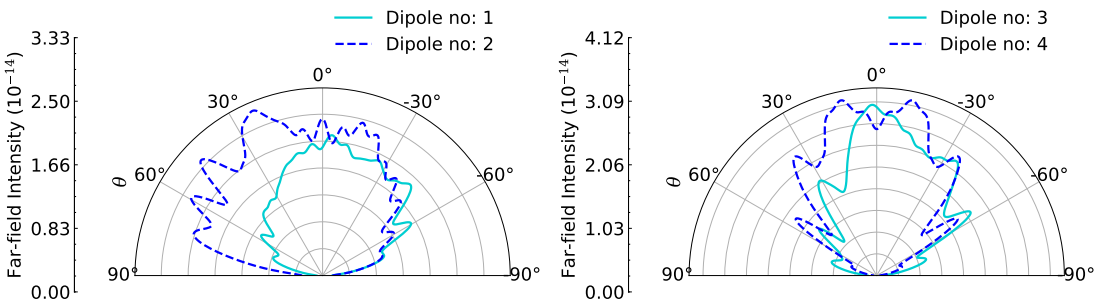

(a) (b)

Figure 4.26: Far-field radiation profiles extracted from the ϕ = [0,90°] cross-sections for the different dipole positions. Dipole 1 is placed near the edge of the pillar while 4 is placed in the center of the pillar.

Asymmetric nanopillar

Some of the experimental nanopillars were not fully symmetric and an asymmetric pillar has been simulated to look for similarities between this and CL/ARCL measurements. How the degree of cone-shaping affects the emission has also been tested with FDTD.

SEM images of the experimental nanopillars reveal a difference in the degree of tilting between the sidewalls on the pillars. Thus, simulations of an asymmetric pillar have been performed to see how this asymmetry influences the electromagnetic fields. The simulation was conducted by moving a dipole with λ = 862 nm through a cross-section of the pillar. The defect positions and the asymmetric pillar is illustrated in Figure 4.27a. The pillar is constructed so that the bottom of the pillar has its center in (0.3, 0.3) while the center of the top of the pillar is in (0,0). One side of the pillar has then steeper tilted sidewalls compared to the other side. Seven dipoles are introduced at a depth of 0.15 μm in a pillar with r_{bottom} = 1.4 μm and r_{top} = 0.6 μm. Dipole no. 4 is placed in the center of the upper part of the pillar. Dipoles 1, 2, and 3 and 5, 6, and 7 are placed with respectively a $\pm$0.2, $\pm$0.4, and $\pm$0.6 μm distance from the center. Figure 4.27b shows the near-field image obtained by the sum over dipoles no. 1 and 7. The image shows stronger intensity from dipole 7, which is placed near the sidewall with the smallest incline. These two dipoles also show the least intensities of all dipoles, and the intensity obtained from a sum over all 7 dipoles shows high intensity at the center of the pillar. The CL intensity maps in Figure 4.11 show intensities that are slightly shifted away from the center of the pillar. As the intensity of is stronger for dipole no. 7 than for no. 1, different angles of the sidewall may be a possible explanation for the intensity variation in the CL intensity maps.

The pillar from the ARCL measurement with two different e-beam positions also showed significant differences between the two different e-beam positions. The far-field from the simulation of the asymmetric dipole is presented for comparison to the ARCL results. Figure 4.28 shows the far-field intensity and the radiation profile of the dipole positioned in the center of the upper part of the pillar. The intensity from the center dipole is higher compared to the other dipole positions and the highest intensity for this dipole is directed towards the side with the

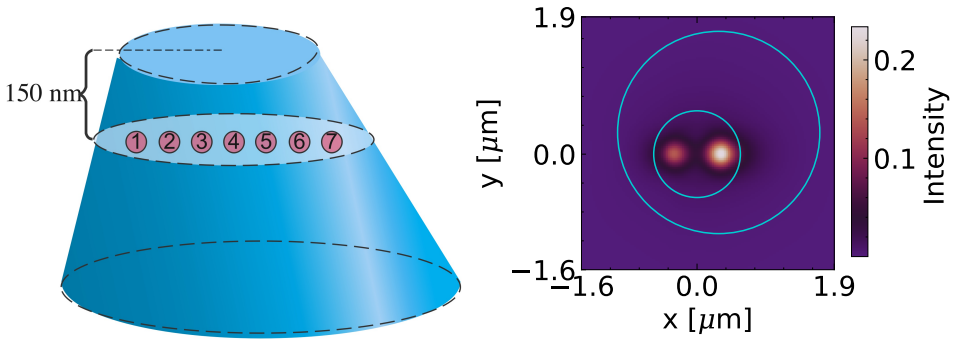

(a) (b)

Figure 4.27: Figure (a) is an illustration of an asymmetric nanopillar with an indication of the dipole positions 1-7. Figure (b) is the near-field obtained from the sum of simulation results from dipoles no. 1 and 7. The blue circles indicate the lower and upper edges of the pillar.

least steep sidewall, the upper part of the pillar seen from above in Figure 4.27b. The radiation profiles of the remaining dipole positions are shown in Figure 4.29. Dipoles no. 3 and 5 are positioned ±0.2 μm from the pillar center and show the highest intensities, apart from the dipole in the center. The far-field intensity images for these two positions are presented in Figure 4.30 in (a) and (b). The radiation from the dipoles shows that the majority of the intensity is found on the opposite side compared to the dipole position. For dipoles no. 2 and 6, placed 0.4 μm off the center of the upper part, the emission is found in the same direction as the position of the dipole. Dipoles no. 1 and 7 in the asymmetric pillar are situated furthest away from the center and also show the lowest intensities, which correspond to the results from the symmetric pillar. Dipoles no. 5, 6, and 7, placed on the least steep side, show higher intensities compared to their opposite positions on the steep side of the pillar.

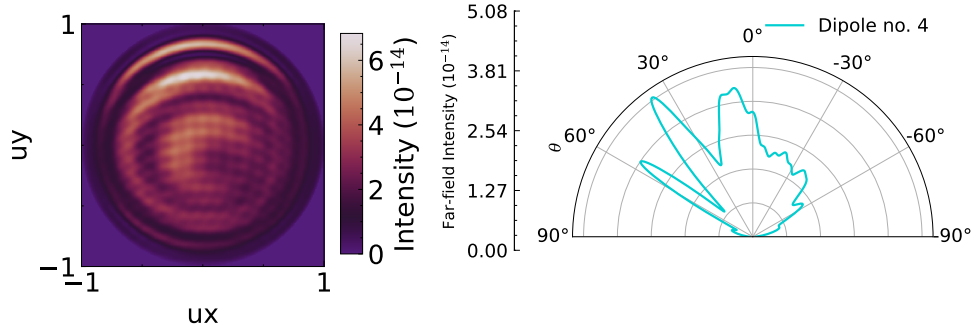

(a) (b)

Figure 4.28: Far-field intensity from an asymmetric pillar with one dipole in the center of the top part of the pillar. (a) is the far-field intensity image and (b) is the radiation profile extracted from (a) of the $\phi = [0,90°]$ cross-section.

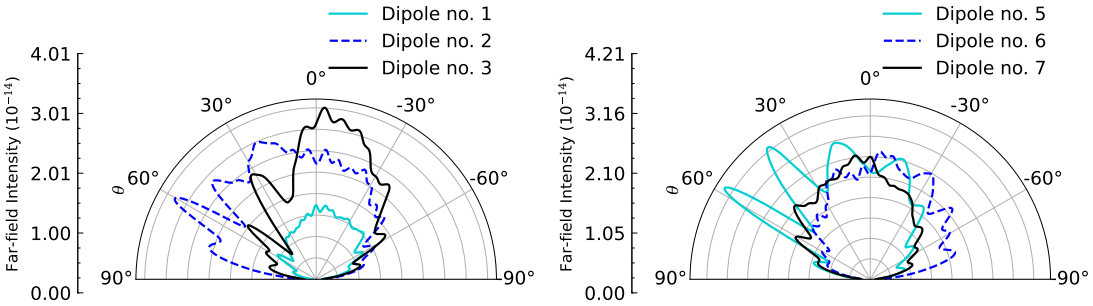

(a) (b)

Figure 4.29: Radiation profiles of different dipole positions in an asymmetric pillar. The positions in (a) are located on the pillar-half with the steepest sidewalls, while the positions in (b) are located on the opposite side.

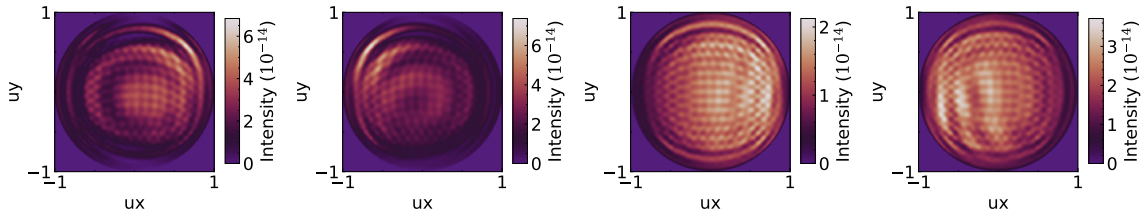

(a) (b) (c) (d)

Figure 4.30: Far-field intensity from dipole positions (a) 3 and (b) 5 corresponding to 0.2 μm offset from the center on each side of the pillar and positions (c) 2 and (d) 6 with 0.4 μm offset from the center of the pillar.

Degree of cone shaping

A pillar with a bottom radius (r) of 1.4 μm has been simulated with different top radii (r_{top}) to see how the degree of coning influences the far-field emission from one dipole source. The wavelength of the simulation was set to 895 nm. Figure 4.31 illustrates the pillars with the smallest and the largest r_{top}. Four structures were modelled with r tops set to 0.2, 1.0, 1.4, and 1.8 μm. The pillar with r_{top} = 1.4 μm corresponds to a pillar with straight side walls.

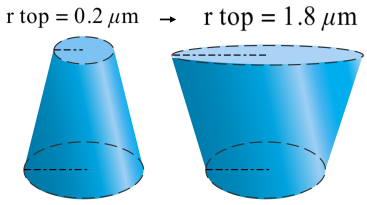

Figure 4.31: Illustration of two pillars with change in r_{top} from 0.2 μm to 1.8 μm

Figure 4.32 shows the far-field intensity images obtained from the simulations. The pillar with r_{top} = 0.2 μm in Figure (a), has the most cone shape and shows a more spread out intensity. As the top radius of the pillar increases, the emission intensity tends to show more interference patterns. The pillar with r_{top} = 1.8 μm, Figure (d), shows the highest intensity, and the straight

pillar in Figure (c) shows the next highest intensity. From the far-field intensity images and the radiation profiles in Figure 4.33, it can be seen that a larger fraction of the emission intensity is outward-directed for structures with r_{top} = 0.2 and 1.8 μm. While the intensity from the structures with r_{top} = 1 and 1.4 μm has lower intensities for higher angles of θ. The outward-directed emission could be connected to the tilted sidewalls for the pillar with r = 0.2 μm as this was something that also was observed in the smallest pillar in the ARCL measurements.

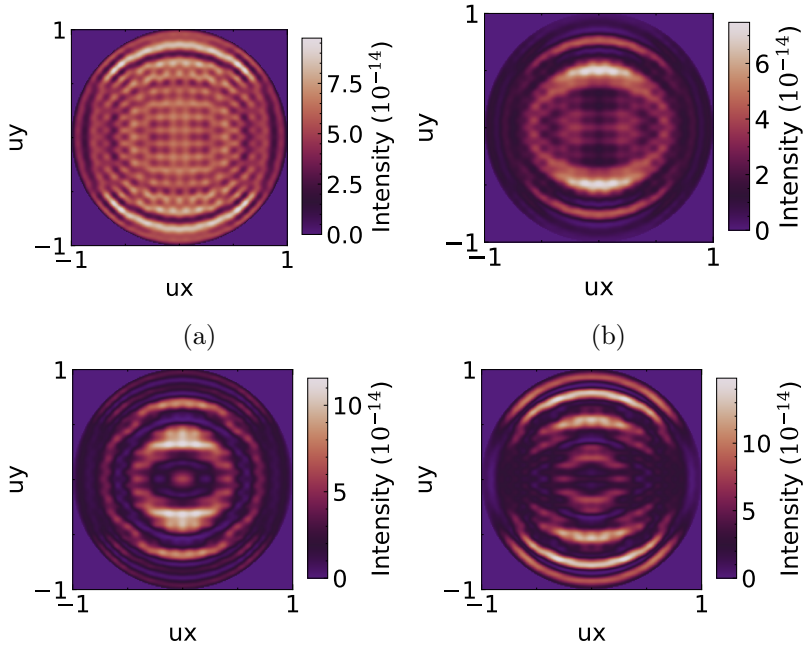

Figure 4.32: Far-field intensity from one dipole source in pillars with r bottom = 1.4 μm and for (a) r_{top} = 0.2 μm, (b) r_{top} = 1.0 μm, (c) r_{top} = 1.4 μm (straight pillar) and (d) r_{top} = 1.8 μm.

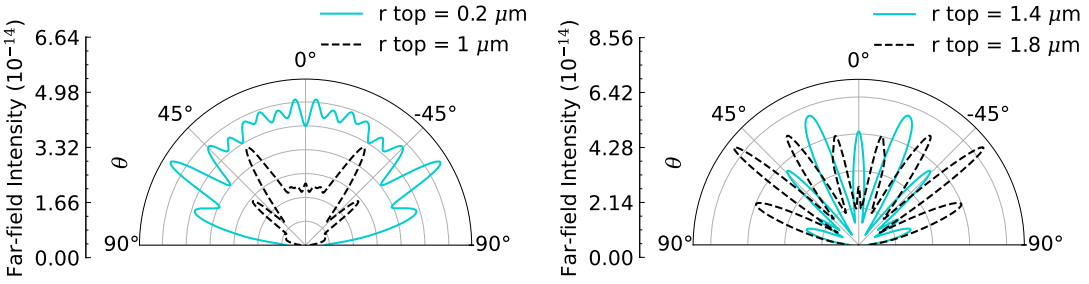

Figure 4.33: Average polar radiation profiles of pillars with r bottom = 1.4 μm and (a) r_{top} = 0.2 and 1.0 μm and (b) r_{top} = 1.4 and 1.8 μm. The radiation profiles are extracted from the $\phi \in$ [0,90°] cross-section.

4.3 Simulations of single emitters in SiC nanostructures

The FDTD method has been developed to model emission from quantum defects in SiC nanostructures measured by CL. The model has been qualitatively verified and later used to investigate the influence of pillar shape, size, and emitter position. Numerical simulations make it possible to further explore structures in a size domain that is not yet possible in the lab. Hence, an important aim of the project is to suggest structures for further experimental investigation. Structures in the same size domain as the experimental pillars have been simulated to investigate how the dipole position influences the emission. Then a pillar with straight sidewalls is simulated with a decreasing radius to see what happens with the emission and the far-field intensity when the structure size is in the size domain of the emitted wavelength. Different dipole positions in the pillar size that showed the highest intensity are also simulated and presented. For the implementation of nanostructures in quantum applications the directionality of the emission is of great interest and thus the far-field projections are used to present the results from the simulations.

4.3.1 Emitter depth

Different dipole position in the xy-plane of a pillar has shown differences in the far-field emission profiles. It is therefore also interesting to model how the far-field is affected by the dipole depth in a coned and a pillar with straight sidewalls. The far-field radial emission profiles from different dipole positions in a cone-shaped pillar with r bottom = 1.4 μm and r top = 0.6 μm are displayed in Figures 4.34 and 4.35. z = 0 μm indicates the dipole positioned at the bottom of the pillar, while at z = 1.4 μm the dipole is placed on the surface of the pillar. The z = 0 and 0.2 μm positions show the highest intensities and also have the most intensity directed normally to the structure. As the dipole height is increased the outward-directed emission increases and the overall emission intensity decreases. The z = 0.6 and 0.8 μm have the largest fraction of outward-directed intensities. For z = 1 μm a large part of the intensity is again directed normal to the structure, which is also the case for z = 1.2 and 1.4 μm. When the dipole is placed on top of the pillar both the emission collected normal to the structure and the emission collected for higher angles of θ are low compared to the other positions. These two top positions also have the most spread out far-field intensities.

The same simulations have been conducted for different dipole positions in a pillar with straight sidewalls and r = 1.4 μm. The far-field radiation profiles from this simulation are displayed in Figures 4.36 and 4.37. This pillar also shows that as the dipole is moved towards the surface the fraction of intensity directed normal to the surface decreases and the intensity at higher angles of θ increases. The dipole at the very bottom of the pillar gives the highest total intensity, but the dipoles at z = 0.2 and 0.4 μm show lower intensities than the dipoles at z = 0.6 μm, which differs from the cone-shaped pillar. The intensities of the different dipole positions in the straight pillar also do not change as much as in the cone-shaped pillar when the dipole is moved towards the top of the pillar. The fraction of outward-directed intensities is also higher in these two positions than in the straight pillar compared to the cone-shaped pillar. The far-field intensity images that the radiation profiles are extracted from for the cone-shaped and straight pillar can be found in Appendix B.3.

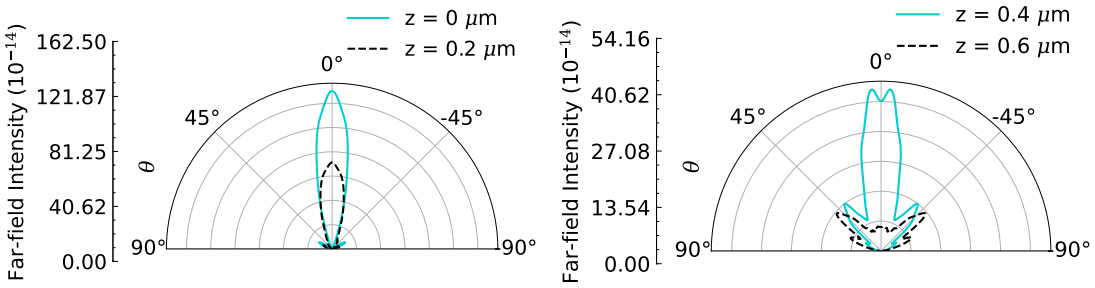

(a) (b)

Figure 4.34: Radial emission profiles from the ϕ = [0,90°] cross-section of the far-field intensity for dipoles placed (a) 0 and 0.2 μm and (b) 0.4 and 0.6 μm from the bottom of the pillar with r bottom = 1.4 μm and r top = 0.6 μm. The wavelength was set to 895 nm in the simulation.

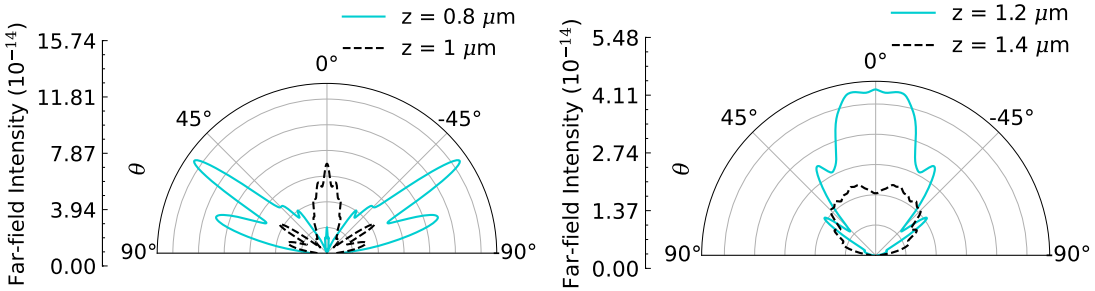

(a) (b)

Figure 4.35: Radial emission profiles from the ϕ = [0,90° of the far-field intensity for dipoles placed (a) 0.8 and 1.0 μm and (b) 1.2 and 1.4 μm from the bottom of the pillar with r bottom = 1.4 μm and r top = 0.6 μm. The wavelength was set to 895 nm in the simulation.

The straight and cone-shaped pillar also show differences in how widespread the emission is in the far-field. Figure 4.38 shows the far-field intensity images from the z = 0.6 μm for the cone-shaped and the straight pillar. The straight pillar shows a more concentrated intensity at the center and at only some parts around the edges, while for the coned pillar the intensity is more evenly distributed. This may indicate that the tilted sidewalls of the coned pillar influence the direction of the outgoing emission, while the emission from the straight pillar is to a greater extent directed in the same direction. The intensity from the straight pillar is also higher than the coned pillar when the dipole is placed 0.6 μm from the bottom of the pillar. Figure 4.38c shows a plot of the total far-field intensity for the dipoles' positions in the straight and cone-shaped pillar. The cone-shaped pillar shows larger intensities for the two lowest positions, but as the height of the dipole is increased, the intensity from the straight pillar is higher. The dipoles placed near the surface of the pillar show the lowest intensity in both pillars. The straight pillar with the dipole placed 0.6 μm from the bottom of the pillar, or 0.8 μm below the surface of the pillar, shows the highest total far-field intensity.

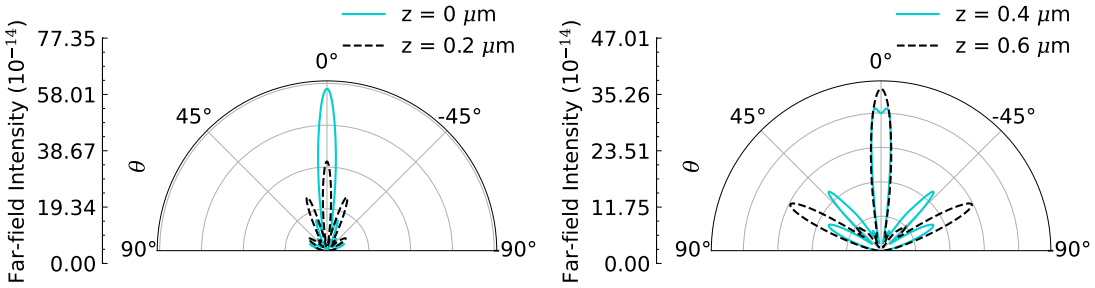

(a) (b)

Figure 4.36: Radial emission profiles from the ϕ = [0,90°] of the far-field intensity for dipoles placed (a) 0.8 and 1.0 μm and (b) 1.2 and 1.4 μm from the bottom of the pillar with straight sidewalls and r bottom = 1.4 μm. The wavelength was set to 895 nm in the simulation.

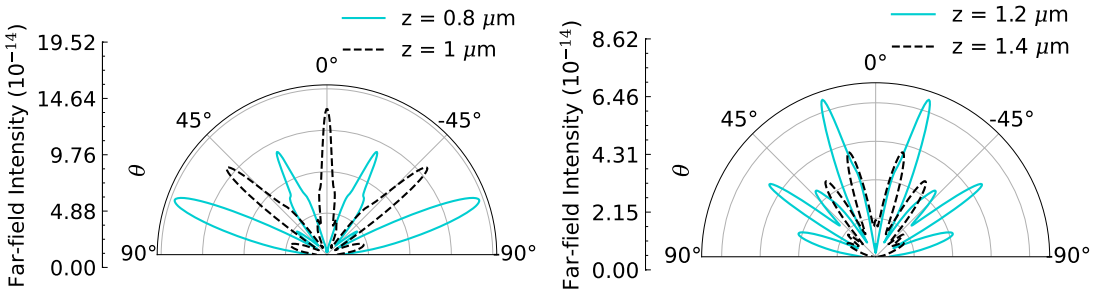

(a) (b)

Figure 4.37: Radial emission profiles from the ϕ = [0,90°] of the far-field intensity for dipoles placed (a) 0.8 and 1.0 μm and (b) 1.2 and 1.4 μm from the bottom of the pillar with straight sidewalls and r bottom = 1.4 μm. The wavelength was set to 895 nm in the simulation.

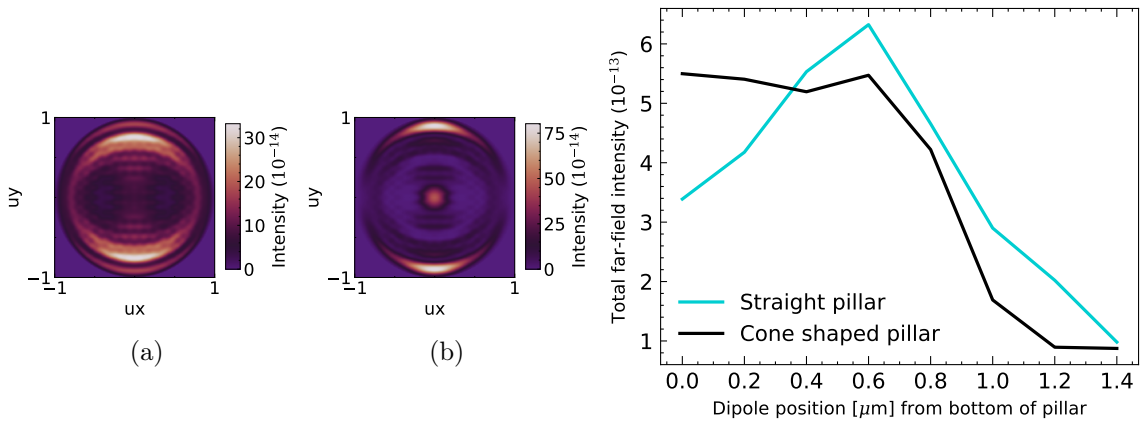

(a) (b) (c)

Figure 4.38: Far-field intensity from (a) a cone-shaped pillar and (b) a straight pillar with the dipole placed 0.6 μm over the bottom of the pillar. Figure (c) is the total far-field intensity of different dipole positions in a cone-shaped and a straight pillar.

4.3.2 Size dependence of nanopillar

With simulation tools such as FDTD, the possible structure sizes go below what is practically possible in the MiNa-lab today. Structures with decreasing radii have been simulated to investigate the emission when the diameter is in the size domain of the emitted wavelength. Figures 4.39 and 4.40 show the far-field intensity images obtained from these simulations. The wavelength in the simulations was set to 862 nm corresponding to the V1 line of V_{Si}^{-}. The intensity is lowest for the smallest pillar and increases as the radius is increased to 0.1 μm and again to 0.15 μm. When the radius is increased to 0.2 μm the increase in intensity is even bigger before it decreases again when the radius is increased to 0.25 μm. The far-field intensity when the radius is increased further gives intensities of approximately the same sizes. The pillar with r = 0.2 μm, which showed the highest intensity, shows emission which is detected for high angles of θ in the far-field. This can also be seen in Figure 4.41a where the radiation profile of r = 0.15 μm and r = 0.2 μm is plotted. With r = 0.2 μm the diameter of the pillar will be 400 nm, which is almost half the length of the wavelength. The total far-field intensity of pillars with a radius ranging from 0.05 to 1.4 μm is displayed in Figure 4.41b. The intensity does not change as much when the radius is increased from 0.25 μm, however, the curve shows some oscillation, and the cause of this oscillation is not known. Some radii like 0.55, 0.70, 0.90 and 1.05 μm show higher total intensities.

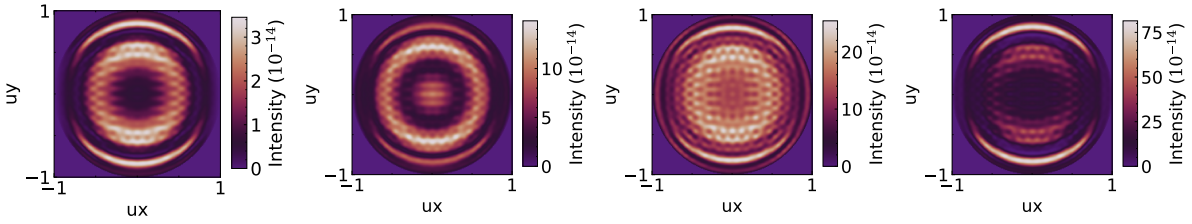

(a) r=0.05 (b) r = 0.1 μm (c) r = 0.15 μm (d) r = 0.2 μm

Figure 4.39: Far-field intensity from a pillar with straight sidewalls and increasing radius. The wavelength was set to 862 nm.

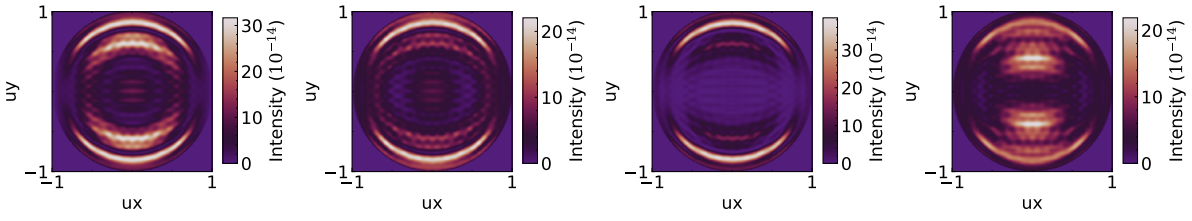

(a) r = 0.25 μm (b) r = 0.3 μm (c) r = 0.35 μm (d) r = 0.4 μm

Figure 4.40: Far-field intensity from a pillar with straight sidewalls and increasing radius. The wavelength was set to 862 nm.

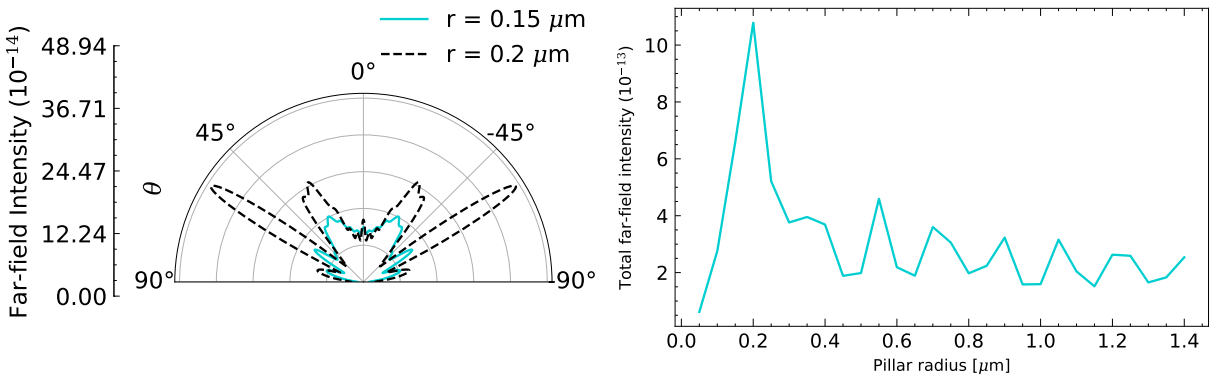

(a) (b)

Figure 4.41: (a) Radiation profile from the ϕ = [0,90°] cross-section of pillars with r = 0.15 and 0.2 μm. Simulated with λ = 862 nm (b) Total far-field intensity as function of radius.

Dipole position and pillar height of the r = 0.2 μm pillar

All dipoles in the above simulations were placed 0.15 μm under the surface of the pillar. Since the pillar with r = 0.2 μm showed significantly more intensity compared to the other pillars it was interesting to investigate how the dipole position in this pillar influenced the far-field intensity. Figure 4.42a shows a plot of the total far-field intensity for different dipole positions. The blue graph corresponds to dipoles placed in the center of the pillar, while the black graph corresponds to dipoles placed 0.2 μm from the center, so at the pillar wall. The highest intensities belong to the center dipoles positioned at 0.4 and 0.7 μm from the bottom of the pillar, which corresponds to respectively 1 and 0.7 μm under the surface of the pillar. The dipoles positioned at the very bottom and at the surface of the pillar show the least intensities. The far-field intensity images for the z=0.4 and 0.7 μm center positions are displayed in Figure 4.43a and 4.43b. The intensity obtained from the dipole at 0.7 μm is more widespread while for the dipole at 0.4 μm, the intensity is more concentrated at the edges. A pillar with r = 0.2 μm and dipoles placed in the center of the pillar 0.7 μm under the surface thus gives the highest far-field intensities.

The height of the pillar with r = 0.2 μm has also been varied and simulated. The height was varied from 0.2 μm to 1.4 μm in steps of 0.05 μm. The dipole was placed 0.15 μm below the top of the pillar. The total far-field intensity for the different heights is displayed in Figure 4.42b. The pillar with height = 0.5 μm shoes the highest total intensity, and the pillars with height below 0.4 μm show significantly lower intensities than the rest. The far-field intensity image of the pillar with height = 0.5 μm is displayed in Figure 4.43c.

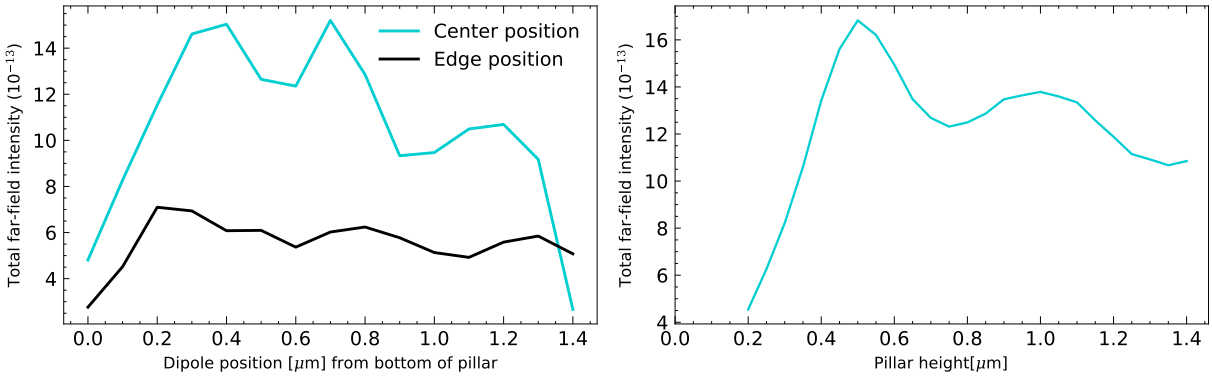

(a) (b)

Figure 4.42: Figure (a) shows total far-field intensity for different dipole positions in a pillar with r = 0.2 μm. The dipoles at the edge position are positioned 0.2 μm from the center of the pillar. Figure (b) shows the total far-field intensity for different height of the same pillar.

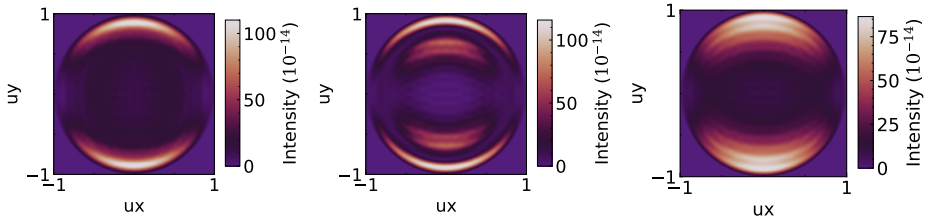

(a) (b) (c)

Figure 4.43: Far-field intensity from a pillar with r = 0.2 μm with the dipole positioned at the center of the pillar at (a) 0.4 μm and (b) 0.7 μm from the bottom. Figure (c) is the far-field intensity from a pillar with r = 0.2 μm and height of 0.5 μm.

4.3.3 Other possible photonic structures

The simulation method has also been used to explore structures with different shapes. A hemisphere, a rectangular waveguide, and a pyramid have been simulated. Results for all structures are presented here as an example of possible further exploration of nanostructures for quantum technology. Further exploration of the structures is possible for further work. Convergence tests of the simulation region of these structures were not conducted herein but should be performed for further simulations. Each structure is simulated both with size in the same domain as the experimental pillars (2.8 μm) and in the 400 nm dimension, corresponding to the pillar in section 4.3.2 with r = 0.2 μm that showed the highest intensities. Figure 4.44 illustrates the structures with the dipole position indicated as the blue arrow. The height of the structures was set to 1.4 μm and the dipoles were positioned 0.15 μm below the surface. All simulations were conducted with the wavelength set to 862 nm. This section presents the polar radiation profiles for the structures, the far-field intensity images from the simulations can be found in Appendix B.5.

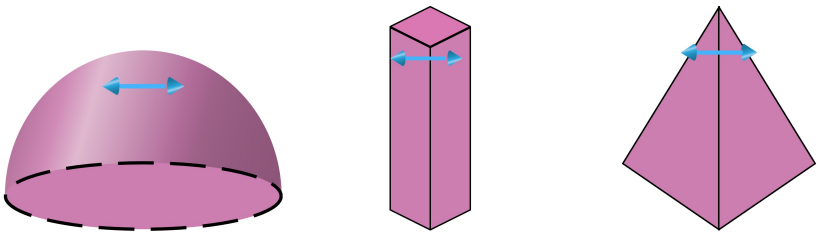

(a) (b) (c)

Figure 4.44: Illustration of the different structures simulated. The Figures show (a) a hemisphere, (b) a rectangular waveguide and (c) a pyramid.

Figure 4.45 presents the radiation profiles of the far-field intensity from hemispheres with (a) r = 1.4 and (b) 0.2 μm The dipole was positioned 0.15 m below the top of the hemisphere. The polar emission profile in Figure 4.45a shows the highest intensity at θ=0°. The radiation profile in Fig. 4.45b from the structure with r = 0.2 μm shows intensities at θ=0° which is almost doubled compared to the bigger one in Figure 4.45a. The far-field intensity is also more evenly distributed for the small hemisphere, as well as it shows higher intensities for higher angles of θ than the hemisphere with r = 1.4 μm.

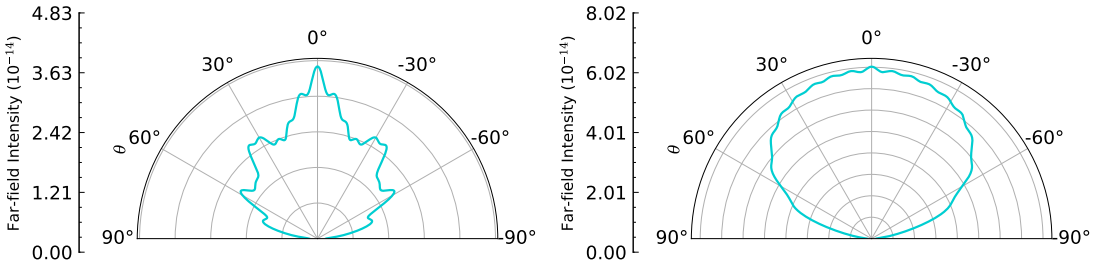

(a) (b)

Figure 4.45: Polar radiation profiles of the far-field intensity from a hemisphere with (a) r = 1.4 μm and (b) r = 0.2 μm.

The radiation profiles from the simulations of the rectangular waveguide of (a) 2.8 μm and (b) 0.4 μm is presented in Figure 4.46. The rectangular waveguide shows more intensity difference between the structure of 2.8 μm and the one of 0.4 μm compared to the hemisphere and the pyramid. The small structure shows intensities six times larger compared to the structure of 2.8 μm.

Figure 4.47 presents the radiation profiles obtained from the pyramid of (a) 2.8 μm and (b) 0.4 μm. Both the rectangular waveguide and the pyramid show higher intensities at θ = 0° for the large structure than for the structure of 0.4 μm. These structures are presented here for illustration of how the developed method can be used further.

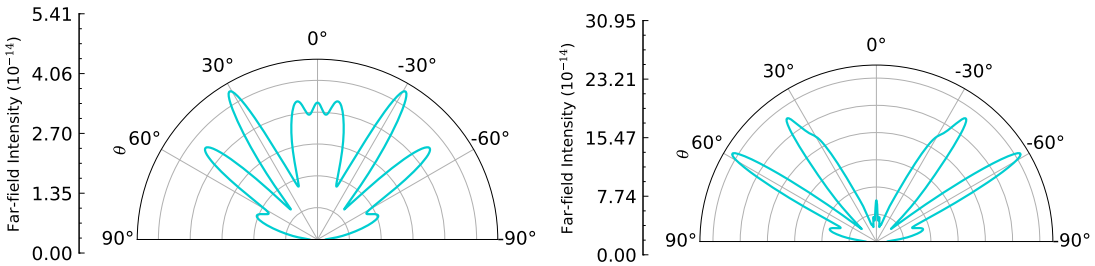

(a) (b)

Figure 4.46: Polar radiation profiles of the far-field intensity from a rectangular waveguide of (a) 2.8 μm and (b) 0.4 μm.

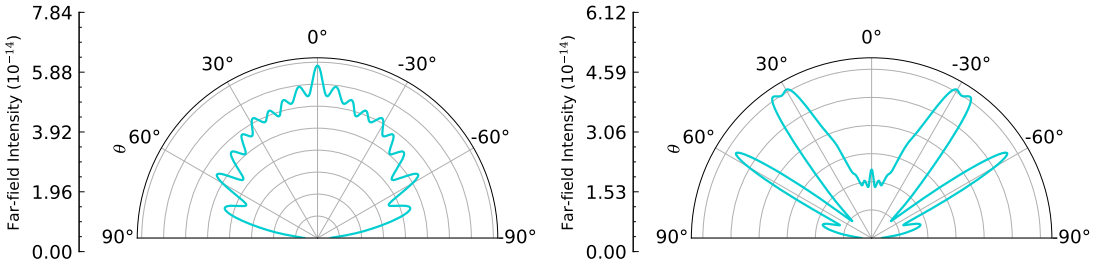

(a) (b)

Figure 4.47: Polar radiation profiles of the far-field intensity from a pyramid of (a) 2.8 μm and (b) 0.4 μm.

Chapter 5

Concluding remarks

5.1 Conclusion

In this work, experimental measurements with CL and ARCL have been used to verify the simulation method developed for modelling emission from single-photon emitters in SiC nanostructures. The V_{Si} was identified with CL in a SiC sample with nanostructures and measurements of structures with different sizes showed increased emission intensity from V_{Si}^- in the nanostructures compared to the intensity from the substrate. The nanostructures also showed higher emission intensities from V_{Si}^- in the center of the structures. The near-field obtained from the FDTD simulations was compared to the CL-intensity maps, and the simulations of the nanostructures also showed increased intensities at the pillars' centers.

The nanostructures' influence on the directionality of the V_{Si}^- emission was revealed with radial emission profiles from ARCL measurements. The angle-resolved emission profiles of the emission from the pillars and the substrate were compared and showed that the pillars deviated from the Lambertian emission profile obtained from the substrate. The FDTD simulation method was verified by comparisons between ARCL and FDTD results. Both radiation profiles from ARCL and FDTD showed the highest outward-directed emission from the smallest pillar with r = 1.4 μm. Features like the asymmetry of the pillar and dipole positions in the nanostructures were explored with FDTD and an asymmetric pillar shows intensity variations for different dipole positions.

Simulations with FDTD were further used for simulations of nanostructures not yet available in the MiNa-lab. The radius of a straight pillar was changed and showed significantly higher intensities for the pillar with a radius of 0.2 μm and the dipole placed 0.7 μm from the top of the pillar. The pillar height was also varied for this pillar and the highest intensities were obtained for a height of 0.5 μm.

5.2 Further work

This project has focused on optical characterization of the V_{Si} in 4H-SiC and the development of a simulation method for emission from defects in nanostructures. Further work is necessary for understanding the emission from nanopillars, but at the same time the developed method opens up many possibilities for further investigations and exploration of defect emission in optical structures. The following list presents some of the challenges experienced during this work that should be studied further and suggestions for new avenues to explore the present model.

- One of the challenges related to SiC nanopillars is the positioning of the emitter inside the pillar as well as the fabrication of pillars in the size domain of the emitted wavelength. The maximum enhancement of an emitter in a pillar has been shown for a pillar with half the size of the emission wavelength with a dipole positioned at about half wavelength from the top [50].

- V_{Si} has shown to be a possible candidate for quantum sensing and some of the remaining challenges include enhancement of defects in waveguides. Thus further improvement in integration and scalability of future devices is needed.

- The model developed in this project presents a simplification of the nanostructures. The complexity of the model can be increased by implementing surface roughness which will create a more realistic scenario.

- Other challenges of SiC as host QT include material fabrication and generation of quantum compatible point defects in SiC.

- The developed method may also be used to explore coupled or arrays of nanopillars. The use of classical electromagnetism opens up for the investigation of how different waveguides and defects will interact.

Bibliography

[1] Michael Riordan. The lost history of the transistor, Jun 2021.

[2] G. E. Moore. Electronics. 38, 1965.

[3] Marianne Etzelmüller Bathen. *Point defects in silicon carbide for quantum technologies: Identification, tuning and control.* PhD thesis, University of Oslo, 2020.

[4] The birth of quantum theory, Dec 2021.

[5] A Einstein. Annalen der physik, 322. *Iss*, 6:132, 1905.

[6] Jonathan P Dowling and Gerard J Milburn. Quantum technology: the second quantum revolution. *Philosophical Transactions of the Royal Society of London. Series A: Mathematical, Physical and Engineering Sciences*, 361(1809):1655–1674, 2003.

[7] Frank Arute, Kunal Arya, Ryan Babbush, Dave Bacon, Joseph C Bardin, Rami Barends, Rupak Biswas, Sergio Boixo, Fernando GSL Brandao, David A Buell, et al. Quantum supremacy using a programmable superconducting processor. *Nature*, 574(7779):505–510, 2019.

[8] David P DiVincenzo. The physical implementation of quantum computation. *Fortschritte der Physik: Progress of Physics*, 48(9-11):771–783, 2000.

[9] Oded Goldreich. Foundations of cryptography: Basic tools, cambridge u, 2001.

[10] Antonio Acín, Immanuel Bloch, Harry Buhrman, Tommaso Calarco, Christopher Eichler, Jens Eisert, Daniel Esteve, Nicolas Gisin, Steffen J Glaser, Fedor Jelezko, et al. The quantum technologies roadmap: a european community view. *New Journal of Physics*, 20(8):080201, 2018.

[11] Christian L Degen, F Reinhard, and Paola Cappellaro. Quantum sensing. *Reviews of modern physics*, 89(3):035002, 2017.

[12] Gard Momrak Selnesaunet. Nanostructuring of sic for novel defect-based quantum technologies. Master's thesis, 2021.

[13] Marcus W Doherty, Neil B Manson, Paul Delaney, Fedor Jelezko, Jörg Wrachtrup, and Lloyd CL Hollenberg. The nitrogen-vacancy colour centre in diamond. *Physics Reports*, 528(1):1–45, 2013.

[14] Lucio Robledo, Lilian Childress, Hannes Bernien, Bas Hensen, Paul FA Alkemade, and Ronald Hanson. High-fidelity projective read-out of a solid-state spin quantum register. *Nature*, 477(7366):574–578, 2011.

[15] JR Weber, WF Koehl, JB Varley, A Janotti, BB Buckley, CG Van de Walle, and David D Awschalom. Quantum computing with defects. *Proceedings of the National Academy of Sciences*, 107(19):8513–8518, 2010.

[16] Kane Yee. Numerical solution of initial boundary value problems involving maxwell's equations in isotropic media. *IEEE Transactions on antennas and propagation*, 14(3):302–307, 1966.

[17] Charles Kittel and Paul McEuen. *Kittel's Introduction to Solid State Physics*. John Wiley & Sons, 2018.

[18] Ben G Streetman, Sanjay Banerjee, et al. *Solid state electronic devices*, volume 10. Pearson/Prentice Hall Upper Saddle River, NJ, 2006.

[19] Marianne Etzelmüller Bathen and Lasse Vines. Manipulating single-photon emission from point defects in diamond and silicon carbide. *Advanced Quantum Technologies*, 4(7):2100003, 2021.

[20] Michael A Reshchikov and Hadis Morkoç. Luminescence properties of defects in gan. *Journal of applied physics*, 97(6):5–19, 2005.

[21] Ivan Pelant and Jan Valenta. *Luminescence spectroscopy of semiconductors*. OUP Oxford, 2012.

[22] Thomas Aichele, Ulrike Herzog, Matthias Scholz, and Oliver Benson. Single-photon generation and simultaneous observation of wave and particle properties. In *AIP Conference Proceedings*, volume 750, pages 35–41. American Institute of Physics, 2005.

[23] N Iwamoto and BG Svensson. Defects in semiconductors, point defects in silicon carbide, edited by l. romano, v. privitera, and c. jagadish, 2015.

[24] David J Christle, Abram L Falk, Paolo Andrich, Paul V Klimov, Jawad Ul Hassan, Nguyen T Son, Erik Janzén, Takeshi Ohshima, and David D Awschalom. Isolated electron spins in silicon carbide with millisecond coherence times. *Nature materials*, 14(2):160–163, 2015.

[25] Zhao Mu, Soroush Abbasi Zargaleh, Hans Jurgen von Bardeleben, Johannes E Froch, Milad Nonahal, Hongbing Cai, Xinge Yang, Jianqun Yang, Xingji Li, Igor Aharonovich, et al. Coherent manipulation with resonant excitation and single emitter creation of nitrogen vacancy centers in 4h silicon carbide. *Nano letters*, 20(8):6142–6147, 2020.

[26] Stefania Castelletto and Alberto Boretti. Silicon carbide color centers for quantum applications. *Journal of Physics: Photonics*, 2(2):022001, 2020.

[27] Marianne Etzelmüller Bathen, Augustinas Galeckas, Johanna Müting, Hussein M Ayedh, Ulrike Grossner, José Coutinho, Ymir Kalmann Frodason, and Lasse Vines. Electrical charge state identification and control for the silicon vacancy in 4h-sic. *npj Quantum Information*, 5(1):1–9, 2019.

[28] Z Shang, A Hashemi, Y Berencén, H-P Komsa, P Erhart, S Zhou, M Helm, AV Krasheninnikov, and GV Astakhov. Local vibrational modes of si vacancy spin qubits in sic. *Physical Review B*, 101(14):144109, 2020.

[29] Marina Radulaski, Matthias Widmann, Matthias Niethammer, Jingyuan Linda Zhang, Sang-Yun Lee, Torsten Rendler, Konstantinos G Lagoudakis, Nguyen Tien Son, Erik Janzen, Takeshi Ohshima, et al. Scalable quantum photonics with single color centers in silicon carbide. *Nano letters*, 17(3):1782–1786, 2017.

[30] Toshiaki Suhara and Masatoshi Fujimura. *Waveguide nonlinear-optic devices*, volume 11. Springer Science & Business Media, 2003.

[31] Saleh and Teich. *Fundamentals of photonics*. 1991.

[32] Helge Engan. *Waveguide propagation*. NTNU, Department of Physics, Institutt for elektronikk og telekommunikasjon, Trondheim, Norway, 2006.

[33] Stefania Castelletto, Alberto Peruzzo, Cristian Bonato, Brett C. Johnson, Marina Radulaski, Haiyan Ou, Florian Kaiser, and Joerg Wrachtrup. Silicon carbide photonics bridging quantum technology. *ACS Photonics*, 9(5):1434–1457, 2022.

[34] Shunchong Wang, Minjie Zhan, Gang Wang, Hongwen Xuan, Wei Zhang, Chunjun Liu, Chunhua Xu, Yu Liu, Zhiyi Wei, and Xiaolong Chen. 4H-SiC: a new nonlinear material for midinfrared lasers. *Laser & Photonics Reviews*, 7(5):831–838, July 2013.

[35] F Sardi, T Kornher, M Widmann, R Kolesov, F Schiller, T Reindl, M Hagel, and J Wrachtrup. Scalable production of solid-immersion lenses for quantum emitters in silicon carbide. *Applied Physics Letters*, 117(2):022105, 2020.

[36] Allen Taflove, Susan C Hagness, and Melinda Piket-May. Computational electromagnetics: the finite-difference time-domain method. *The Electrical Engineering Handbook*, 3, 2005.

[37] John B Schneider. Understanding the finite-difference time-domain method. *School of electrical engineering and computer science Washington State University*, 28, 2010.

[38] Umran S. Inan and Robert A. Marshall. *The FDTD grid and the Yee algorithm*, page 72–112. Cambridge University Press, 2011.

[39] Ansys lumerical FDTD simulation of photonic components. `https://www.ansys.com/products/photonics/fdtd`, 2021.

[40] Interactions of ions with matter. `http://www.srim.org/`, 2008.

[41] Joseph I Goldstein, Dale E Newbury, Joseph R Michael, Nicholas WM Ritchie, John Henry J Scott, and David C Joy. *Scanning electron microscopy and X-ray microanalysis*. Springer, 2017.

[42] Toon Coenen, Benjamin JM Brenny, Ernst Jan Vesseur, and Albert Polman. Cathodoluminescence microscopy: Optical imaging and spectroscopy with deep-subwavelength resolution. *Mrs Bulletin*, 40(4):359–365, 2015.

[43] BJM Brenny, T Coenen, and A Polman. Quantifying coherent and incoherent cathodoluminescence in semiconductors and metals. *Journal of Applied Physics*, 115(24):244307, 2014.

[44] E. Fred Schubert. *Light-Emitting Diodes*. Cambridge University Press, 2 edition, 2006.

[45] Jean-Pierre Berenger. A perfectly matched layer for the absorption of electromagnetic waves. *Journal of computational physics*, 114(2):185–200, 1994.

[46] Cole P Van Vlack. *Dyadic green functions and their applications in classical and quantum nanophotonics*. Queen's University (Canada), 2012.

[47] Martin H. Weik. *Wave Impedance*, pages 1913–1913. Springer US, 2001.

[48] Wenhua Yu and Raj Mittra. A conformal finite difference time domain technique for modeling curved dielectric surfaces. *IEEE Microwave and Wireless Components Letters*, 11(1):25–27, 2001.

[49] Monte carlo simulations of electrontrajectory in solids (CASINO). `https://www.gegi.usherbrooke.ca/casino/What.html`, 2016.

[50] Faraz A Inam and Stefania Castelletto. Understanding the photonics of single color-center emission in a high-indexed nano-pillar. *Journal of Applied Physics*, 130(8):083102, 2021.

Appendix A

Angle-resolved cathodoluminescence

A.1 Polar emission profiles of pillars with r = 1.9 and 2.9 μm

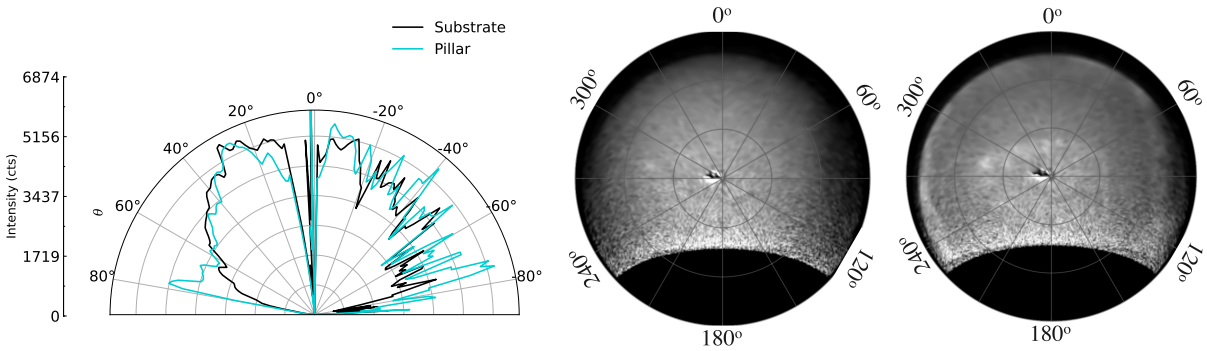

(a) (b)

Figure A.1: Polar emission profiles from ARCL for a pillar with r = 1.9 μm.

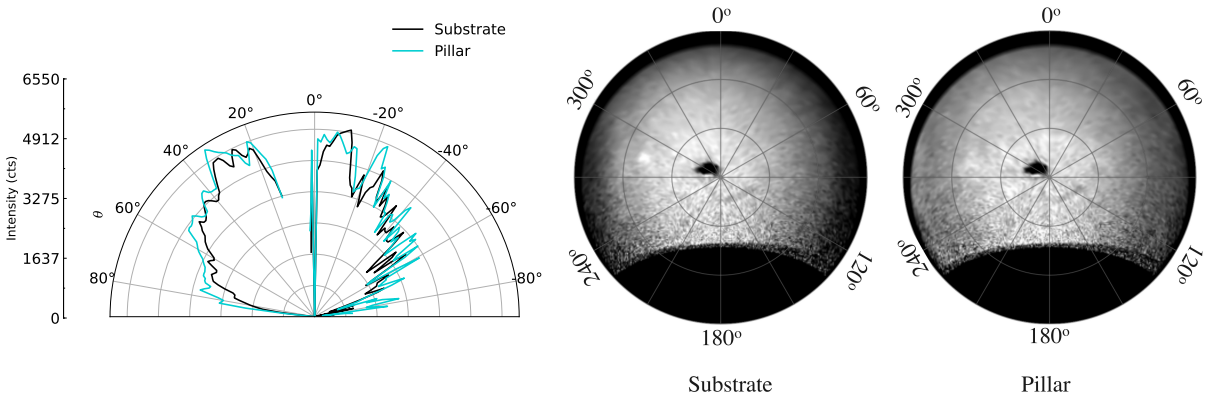

(a) (b)

Figure A.2: Polar emission profiles from ARCL for a pillar with r = 2.9 μm

Appendix B

FDTD simulations

B.1 Random position of dipoles

```
um = 1e-6;
#Geometries of pillar
r_top = 1.8;
r_bottom = 2.4;

select("trunc_cone");
set("z span", 1.4*um);
set("r top", r_top*um);
set("r bottom", r_bottom*um);

randreset(973);
no_dipoles = 50;

#loop that moves the dipole around
for(i=1:no_dipoles){
#save file
    save("dipole_" + num2str(i));
    switchtolayout;

    r = r_top*sqrt(rand);
    theta = rand * 2 * pi;
    X = r * cos(theta); Y = r * sin(theta);

    select("source");
    set("x",X*um); set("y",Y*um);
    set("phi", 0);

    ?"running simulation " + num2str(i) + " of " + num2str(no_dipoles);
    run;
}
```

B.2 Result acquisition

```
function analysis(filename){
#analysis
m = "2Dz"; #monitor name
res = 201; #far-field resolution

#far-field
E2 = farfield3d(m,1,res,res);
ux = farfieldux(m,1,res,res);
uy = farfielduy(m,1,res,res);


write("E2_" + filename + ".txt", num2str(E2), "overwrite");

#Near-field
E_near = getelectric(m);
E_near = pinch(E_near, 4);
E_near = pinch(E_near, 3);

write("E_near_" + filename + ".txt", num2str(E_near), "overwrite");

#radiation profiles
theta1 = linspace(-90,90,400);
E_0 = farfieldspherical(E2, ux, uy, theta1, 0);
write("E_0_" + filename + ".txt", num2str(E_0), "overwrite");

E_AVG = matrix(400);
for(j=0:90){
  E_j = farfieldspherical(E2, ux, uy, theta1, j);
  E_AVG = (E_AVG + E_j);
}
write("E_AVG_" + filename + ".txt", num2str(E_AVG/90), "overwrite");
}
```

B.3 Far-field of different emitter depths in a cone-shaped pillar

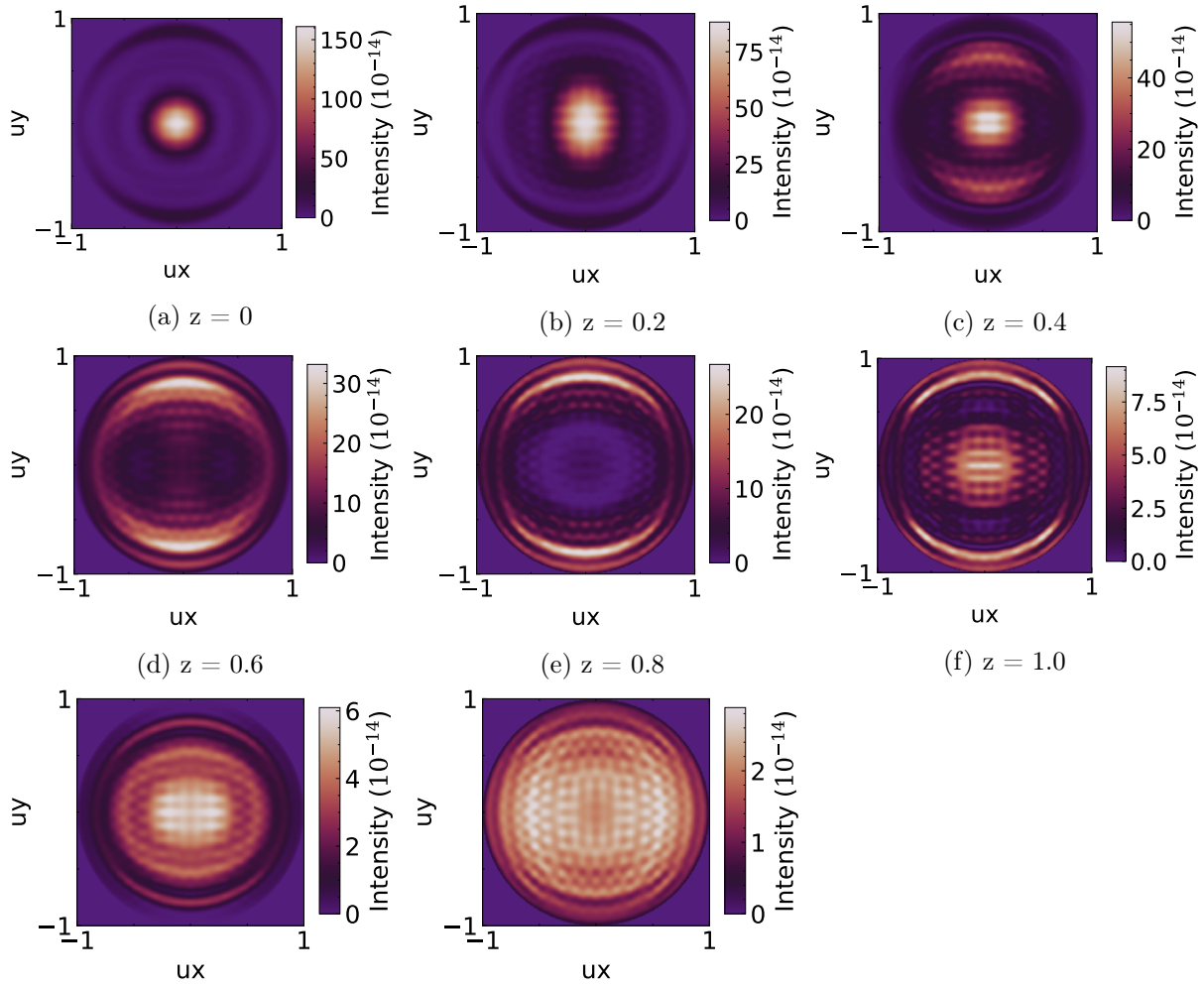

(a) z = 0 (b) z = 0.2 (c) z = 0.4

(d) z = 0.6 (e) z = 0.8 (f) z = 1.0

(g) z = 1.2 (h) z = 1.4

Figure B.1: Cone shaped pillar r = 1.4 μm

B.4 Far-field of different emitter depths in a straight pillar

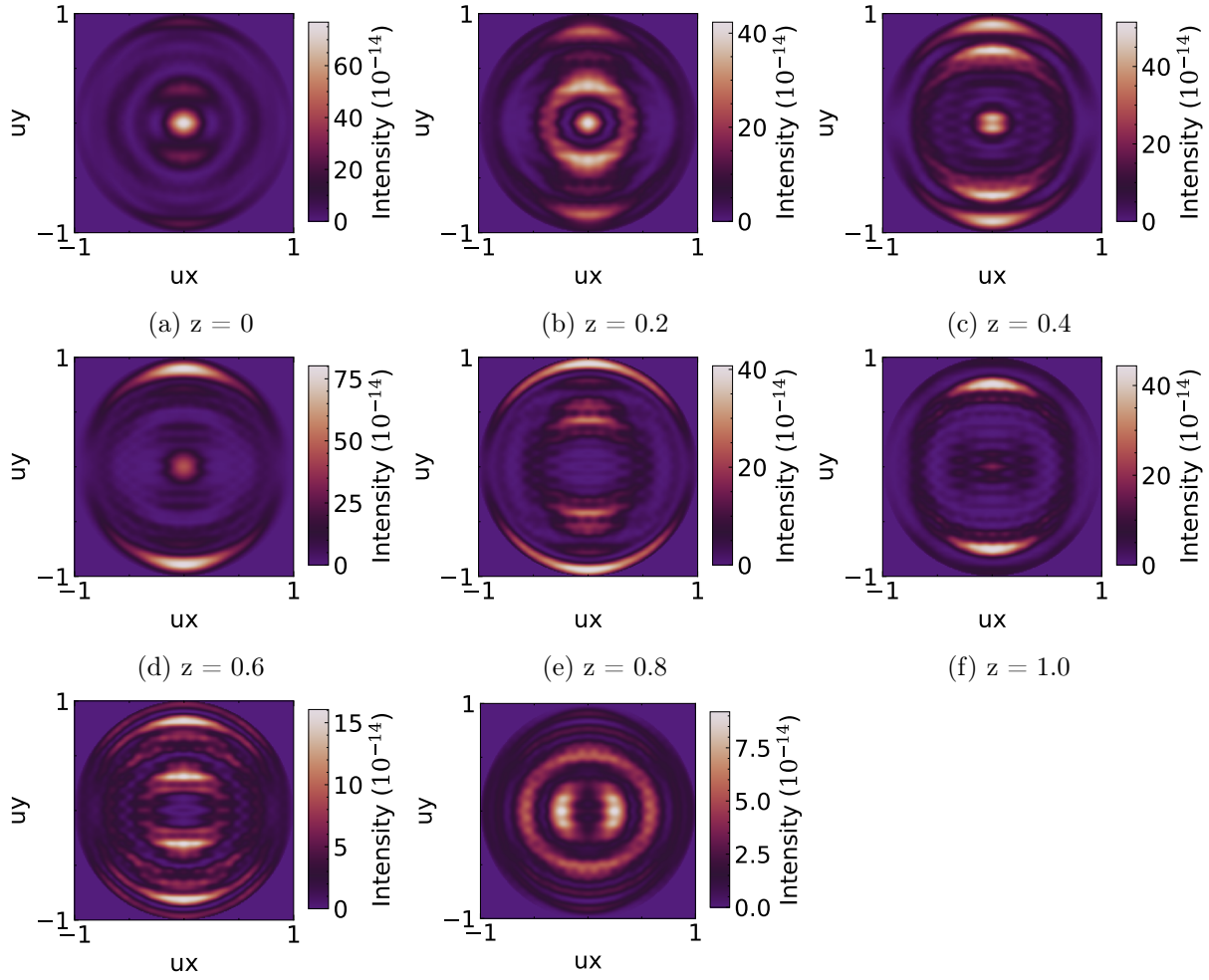

(a) z = 0 (b) z = 0.2 (c) z = 0.4

(d) z = 0.6 (e) z = 0.8 (f) z = 1.0

(g) z = 1.2 (h) z = 1.4

Figure B.2: Pillar with straight sidewalls and r = 1.4 μm

B.5 Other photonic structures

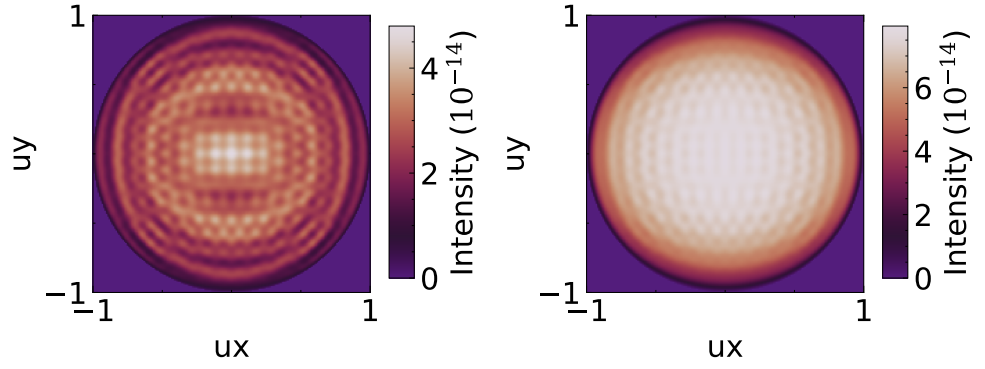

(a) (b)

Figure B.3: Far-field intensity from a hemisphere with (a) r = 1.4 μm and (b) r = 0.2 μm.

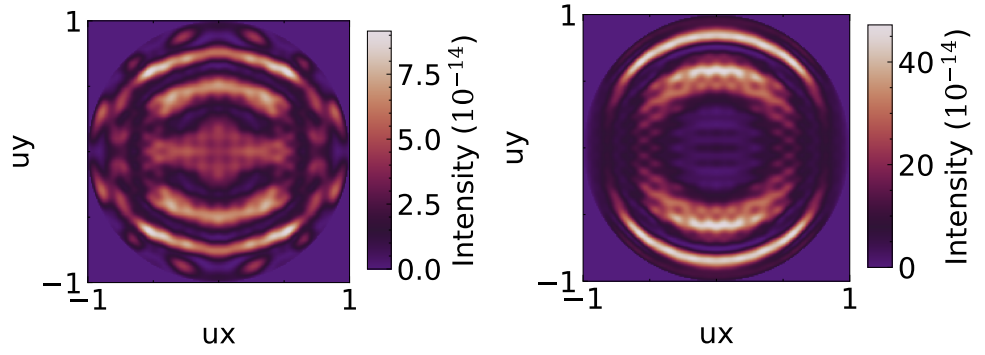

(a) (b)

Figure B.4: Far-field intensity from a rectangular waveguide of (a) 2.8 μm and (b) 0.4 μm.

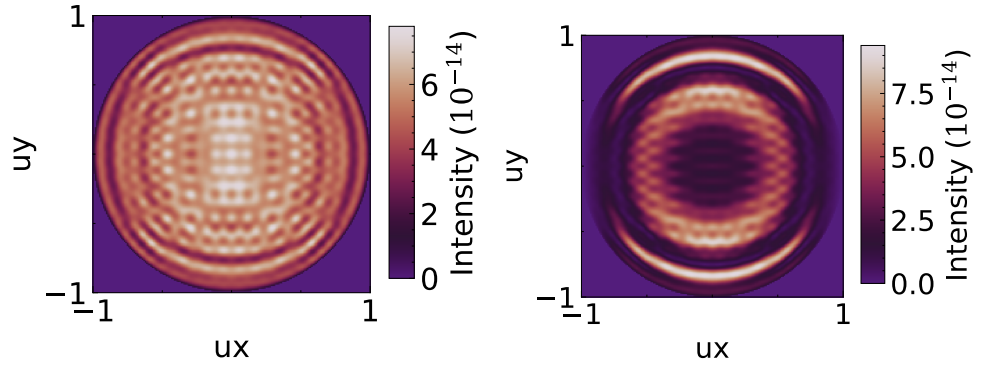

(a) (b)

Figure B.5: Far-field intensity from a pyramid of (a) 2.8 μm and (b) 0.4 μm.